University of Nebraska - Lincoln
DigitalCommons@University of Nebraska - Lincoln

Engineering Mechanics Dissertations & Theses

Mechanical & Materials Engineering, Department of

Summer 7-26-2014

Understanding the Effects of Blast Wave on the Intracranial Pressure and Traumatic Brain Injury in Rodents and Humans Using Experimental Shock Tube and Numerical Simulations

Aravind Sundaramurthy
University of Nebraska-Lincoln, aravind1403@gmail.com

Follow this and additional works at: http://digitalcommons.unl.edu/engmechdiss

 Part of the Applied Mechanics Commons, and the Biomechanical Engineering Commons

Sundaramurthy, Aravind, "Understanding the Effects of Blast Wave on the Intracranial Pressure and Traumatic Brain Injury in Rodents and Humans Using Experimental Shock Tube and Numerical Simulations" (2014). *Engineering Mechanics Dissertations & Theses*. 40.
http://digitalcommons.unl.edu/engmechdiss/40

This Article is brought to you for free and open access by the Mechanical & Materials Engineering, Department of at DigitalCommons@University of Nebraska - Lincoln. It has been accepted for inclusion in Engineering Mechanics Dissertations & Theses by an authorized administrator of DigitalCommons@University of Nebraska - Lincoln.

UNDERSTANDING THE EFFECTS OF BLAST WAVE ON THE INTRACRANIAL PRESSURE AND TRAUMATIC BRAIN INJURY IN RODENTS AND HUMANS USING EXPERIMENTAL SHOCK TUBE AND NUMERICAL SIMULATIONS

By

Aravind Sundaramurthy

A DISSERTATION

Presented to the Faculty of

The Graduate College at the University of Nebraska

In Partial Fulfillment of Requirements

For the Degree of Doctor of Philosophy

Major: Mechanical Engineering and Applied Mechanics

Under the Supervision of Professor Ruqiang Feng

Lincoln, Nebraska

July, 2014

UNDERSTANDING THE EFFECTS OF BLAST WAVE ON THE INTRACRANIAL PRESSURE AND TRAUMATIC BRAIN INJURY IN RODENTS AND HUMANS USING EXPERIMENTAL SHOCK TUBE AND NUMERICAL SIMULATIONS

Aravind Sundaramurthy

University of Nebraska, 2014

Adviser: Ruqiang Feng

Blast induced neurotrauma (BINT) has been designated as the "signature injury" to warfighters in the recent military conflicts. In the past decade, conflicts in Iraq (operation Iraqi freedom) and Afghanistan (operation enduring freedom) as well as the increasing burden of the terrorism around the world resulted in an increased number of cases with blast Traumatic Brain Injury (bTBI). Recently, a lot of research has been done to study the neurological and neurochemical degenerations resulting from BINT using animal models especially rat models. However, it is not clear how and whether the biological outcomes from animal models can be translated to humans; this work is aimed to address this issue.

In this dissertation, the criteria for achieving a standardized methodology to produce shock blast waves are identified. Firstly, shock tube adjustable parameters (SAPs) such as breech length, type of gas and membrane thickness were used for controlling and producing desired blast waves by manipulating shock wave parameters (SWPs). Secondly, using a surrogate head model, the data from the laboratory experiments were compared with experimental data obtained from the field explosions data to show the validity of the laboratory experiments. Finally, effect of test section location on the fidelity of the rat

model in simulating field conditions was studied. Through these steps a standardized and accurate method of replicating the field blast was established.

Using the standardized methodology to model blast waves, the intracranial pressure for various incident pressures on the rat model was studied. Furthermore, to understand the mechanisms of loading and to study the influence of field variables, a finite element model of rat along with the simple ellipsoidal model was developed. With these models, the variables that influence the intracranial pressure such as skull thickness, skull modulus, and skull shape and skull cross section area were studied. Finally, experimental data of intracranial pressure from rat and postmortem human specimen (PMHS) along with their corresponding numerical models were used to develop a model to predict the intracranial pressure. Finally, from this model it was predicted that for the same incident pressure human sustain a higher intracranial pressure than rats, which is contrary to the current scaling law developed to scale injury threshold across species, based on mass.

Dedicated to my,

Parents,

To Dr. Namas Chandra for his guidance throughout my PhD,

To all my teachers and god

Acknowledgements

I would like to take this opportunity to express my deepest gratitude to Dr. Namas Chandra. His guidance not only just remained in research but also extended in many issues of life. I am profoundly indebted to Dr. Chandra for teaching me how to do research and for his patience throughout my PhD. I would also like to thank Dr. Ruqiang Feng for his guidance and supervision and all the help he provided me during my time as a PhD student in UNL. I would like to thank Dr. Linxia Gu for her guidance and encouragement during my research work. I would also like to thank my committee members Dr. Yongfeng Lu and Dr. Joseph Turner for their timely suggestions to improve this research work.

I would also like to thank army research office (ARO) for providing funding for this research. The research work was not possible without constant monetary support.

The atmosphere at the Trauma Mechanics Research Facility (TMRF), UNL has always been friendly and conducive to research. I would like to thank Aaron Alai, Nick Kleinschmit, Aaron Holmberg, Brandon Perry, Kurtis Palu and Dr. Maciej Skotak for conducting the experiments and for their friendship. I also thank my present and past colleagues Dr. Guoxin Cao, Dr. Erwan Plougonven, Dr. Maciej Skotak, Dr. Fang Wang, Mathew Kuriakose, Jonathan Salib and Anthony Misistia for their friendship and guidance. Especially, I would like to thank Fang and Matt for their moral support during the final year of PhD. I also thank my seniors Dr. Shailesh Ganpule, Dr. Ashwani Goel, Dr. Monchai Duangpanya and Dr. Lili Zhang for friendship and guidance during my PhD and especially Shailesh for his constant encouragement during my PhD and guidance during writing manuscripts. I would like to thank Yi Hua for his help during my PhD and his friendship.

I would also like to thank Veera Selvan for discussions during research and lifelong friendship that shaped my life.

I would like to thank Dr. Vettrivel Gnaneswaran and Dr. Nirmal Srinivasan for all the help they provided me during my arrival to UNL and for their friendship. My former roommate Srinivasan Venkatesan for his friendship and motivation. I would also like to thank my lifelong friend Chandrasekar Ramasubramanian for inspiring me to pursue research. I would also like to thank Sundaravel Achudhan and Girish Subramaniyam for their moral support and friendship during my PhD.

I would like to thank graduate specialist of mechanical and material engineering Kathie J. Hiatt and doctoral program coordinator of UNL graduate studies Dr. Eva Bachman for their help throughout my PhD.

Finally, I would like to thank my parents and brother who have always been extremely encouraging and accommodative. I can never thank my family enough for their love and for having more faith in me than I had on myself.

Table of Contents

List of Figures

List of tables

CHAPTER 1: INTRODUCTION

1.1. Motivation

Traumatic Brain Injury (TBI) caused by Improvised Explosive Devices (IED) has been described as the "signature wound of the war on terror" [1]. In the past decade, conflicts in Iraq (operation Iraqi freedom) and Afghanistan (operation enduring freedom) as well as the increasing burden of the terrorism around the world resulted in an increased number of cases with blast Traumatic Brain Injury (bTBI). Figure 1.1 shows the worldwide trend of casualties and injuries due to terrorist explosive events from 1999 to 2006. Within civilian population, injuries related to these acts have increased eight-fold in this period [2]. In a recent report by the guardian it was said that this number rose by 43%, despite al-Qaida splintering [3].

Recent literature classifies these injuries as Blast Induced Neurotrauma (BINT) [4-6]. Although invisible to the naked eye, BINT is reported to cause psychological symptoms such as change in mood, thought, and behavior as well as physiological symptoms such as migraine headaches, insomnia, blurred vision, loss of memory, dizziness, vertigo, tinnitus, nausea, and vomiting with exertion [7].

In theater, the exact number of soldiers who have sustained brain injury during their missions in Iraq and Afghanistan is unknown; however, according to USA today, Pentagon officials estimated that up to 360,000 Iraq and Afghanistan veterans might have suffered

brain injuries. Among them are 45,000 to 90,000 veterans whose symptoms persist and warrant specialized care [8].

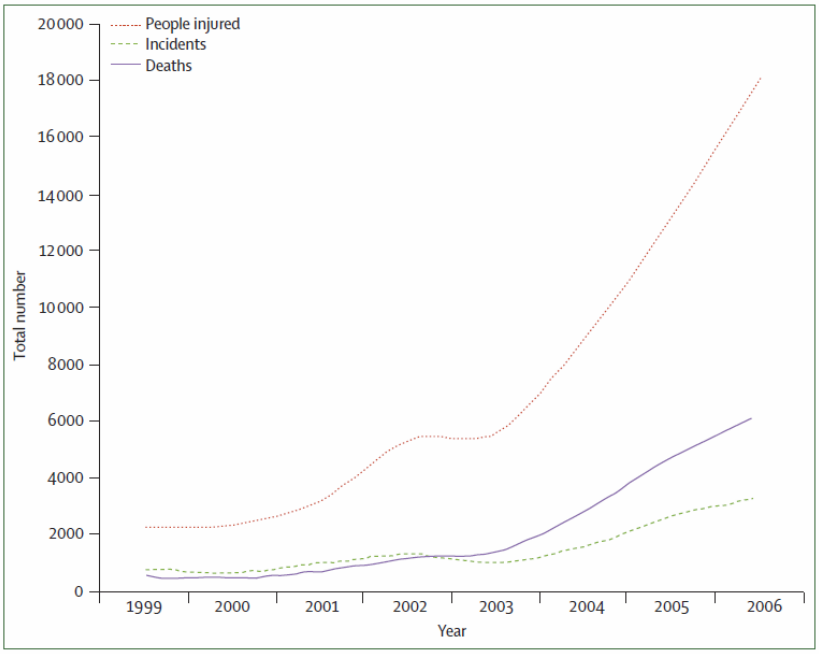

Figure 1.1: Worldwide trends in terrorist explosive events from 1999 to 2006. Source: Wolf 2009 [2]

In a separate study conducted by RAND Corporation, it was estimated that 320,000 service members or 20% of the deployed force (total deployed 1.6 million) potentially suffer from TBI [9]. However, out of this population, approximately 60% have never been assessed by a healthcare provider specifically for TBI. In a stratified telephone interview study conducted among 1965 previously deployed individuals sampled from 24 geographic areas, it was found that a 19% were showing probable symptoms of TBI. Severity of the injury itself or any functional impairment from the injury was not reported [9].

The current literature on BINT suggests conflicting views on its cause, pathophysiology, screening, diagnosis, treatment, and care. BINT's lack of external trauma or invisible internal damage often results in BINT going unrecognized, unacknowledged, and underdiagnosed. Many experts have identified BINT as an emerging subspecialty of traumatic brain injury (TBI) [9]. In addition to the lack of clinical or field data, the scarcity of scientific studies on BINT's prevalence, neuropathophysiology, and symptoms makes it difficult for doctors in terms of diagnosis, therapeutics, and care. Although, BINT is the likely cause for many field related injuries, direct evidence that pure blast causes mechanical insult to the brain and leads to TBI does not exist; except in very rare circumstances where multiple events simultaneously occur. To address this gap, it is vital to study and understand primary blast injury and the subsequent BINT.

1.2. Goals of this research

The two key questions this work will address are: (i) whether shock tube can be used for accurately simulating primary blast injury and, (ii) what are the variables that influence the intracranial pressure sustained and can the intracranial pressure from rat model be translated or scaled to humans. To address these questions, the following goals were set: (a) to reproduce field explosions pertaining to primary blast injury as accurate as possible in a controlled laboratory experiment, (b) to develop an experimental and finite element rat model to study loading incurred during blast, (c) use finite element model of rat head and PMHS model along with the experimental data obtained on intracranial pressure for rat and PMHS to develop a regression model to translate the intracranial pressure from rats to humans using incident pressure as predictor variable.

The first major outcome of this research is an accurate and standardized methodology to study primary blast injury. In general, this would aid the researchers for comparing their results with the results from other laboratories. Furthermore, the accuracy of the blast simulation is vital for the second part of this study where rat and PMHS should be subjected to identical blast conditions to develop a valid primary blast injury model. Secondly, through parametric analysis, blast wave interaction with different head geometries was shown. Through this it was proposed that scaling across species with mass as scaling parameter may be applicable for determining pulmonary injury threshold, however, scaling loads for brain injury threshold using mass will yield erroneous values. Finally, a predictive model for intracranial pressure for both rats and humans will be developed. Assuming that the susceptibility to BINT is determined purely based on tissue level mechanical loading (i.e., intracranial pressure) that exceed acceptable injury threshold values and that the biological response is same at the tissue level across species. We would be able to use the *in vivo* live animal model results, which reported the incident pressure to determine the corresponding intracranial pressures in humans and hence translating the injury threshold to humans.

1.3. Contents of the dissertation

The contents of this dissertation are as follows. In chapter 2, the survey of literature pertaining to various aspects of this dissertation is presented. A review of blast field conditions, available laboratory experiments, computational models, and current scaling law for translating injuries thresholds are reviewed. This chapter starts with an overview of TBI in general and focuses on blast induced traumatic brain injury in particular. This

chapter then outlines the field conditions implicated during primary blast injury. The next part of this chapter reviews various laboratory experiments conducted thus far to understand blast induced mechanical insult to the brain using live and dead animal models. This is followed by the description of the computational animals models developed thus far to study acceleration/blunt and blast induced head injuries. The next part of this chapter describes current scaling methods used for translating mortality and injury threshold to humans from animal model testing.

In the third chapter, we study methods in which field blast can be replicated in a laboratory shock tube. To do this we identify the adjustable parameters in the shock tube and understand their effects individually on the produced blast wave. With this knowledge, we produce the blast wave and compare it with the profiles generated from ConWep simulation software.

Chapter 4 describes the experiments of the blast response of a surrogate head. the pressure-acceleration response of a head-neck human surrogate RED (Realistic Explosion-resistant Dummy) head was evaluated and compared between field explosion tests and in the shock tube with the same set of sensors to verify the validity of the blast pulse produced in a compressed gas driven shock tube.

Chapter 5 describes the experimental studies using instrumented rat model to study the blast induced loading on rat as well as the effect of the test section location on the blast induced loading.

Chapter 6 describes anatomically accurate rat head computational model developed to study the effect of primary blast. This chapter also describes the development of finite element methodology to simulate blast waves. Furthermore, the head model is validated with the experimental results from chapter 5. Validated model was used to study the effects of young's modulus of the skull on intracranial pressure and skull strains. Finally, the model was used for analyzing the loading pathways and subsequent wave propagation in the brain.

Finally, in the first part of chapter 7, a parametric analysis of the influence different head geometric was studied and presented. In the second part of the chapter rat finite element model and the human finite element model along with experimental data of intracranial pressure on PMHS and rat were used to develop a nonlinear regression model to determine the intracranial pressure for various incident pressure. Through this, we hope to deduce the injury threshold for humans based on injury data obtained from animal testing.

Chapter 8 on conclusions includes contributions of this research work and recommendations for future work.

CHAPTER 2: LITERATURE REVIEW

2.1. Introduction:

In this chapter, the literature relevant to the theme of this dissertation; that is to model mechanical loading associated with the primary blast injury and to study the variation of intracranial pressure experienced across the species and develop a model will be reviewed. In section 2.2, the impact of blast induced neurotrauma (BINT) on the society along with its clinical aspects are discussed. In order to study bTBI in the laboratory environment, it is important to replicate relevant field conditions implicated in bTBI, these field conditions are discussed in section 2.3. Next sections of this chapter (i.e. section 2.4 and 2.5) reviews laboratory protocols currently used for replicating field blast conditions along with animals models that are currently used for studying blast induced injury mechanisms. This is followed by a review of finite element model for animal head to study TBI in section 2.6. The next section of this chapter (section 2.7) describes current scaling laws that are used in the study of bTBI.

2.2. Blast injury and blast induced neurotrauma in recent wars

Figure 2.2 shows the classification of blast injury, when an explosive of mass W goes off with a subject at a standoff distance r. The subject may suffer one or more of the following: (a) primary injury due to direct impingement of the shock blast wave, (b) secondary injury from interaction with shrapnel and bomb fragments, (c) tertiary due to impact with

environmental structures or/and (d) quaternary due to inhalation of toxic gases and also all the other injuries that is not included in the first three (Figure 2.1) [10-12].

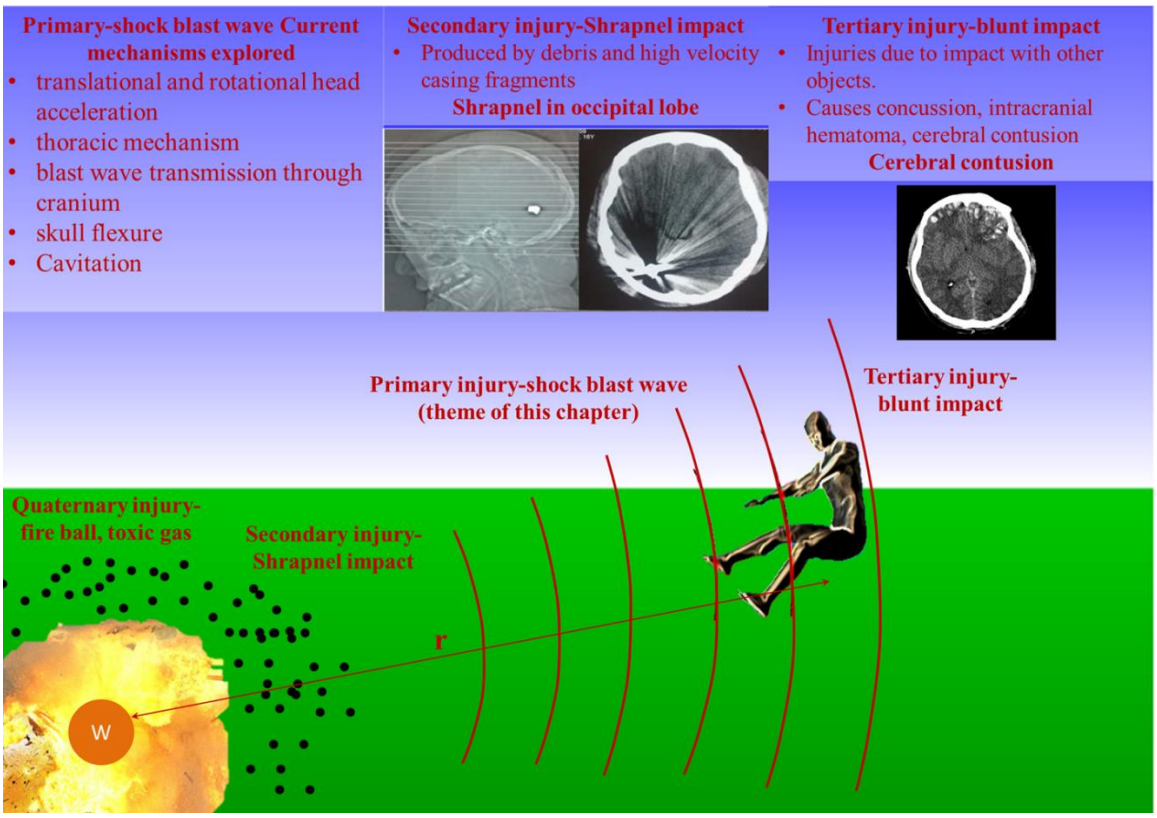

Figure 2.1 bTBI classification, in this figure, *W* is the charge weight and *r* is the standoff distance

Between the American civil war and OIF/OEF, the mortality/morbidity due to gunshot wounds has gradually decreased, whereas the mortality/morbidity due to explosions have increased (Figure 2.2) [13]. In the recent conflicts, this attack is carried out with IEDs. They are usually present in the form of homemade chemical explosives embedded with a variety of shrapnel and typically equipped with a custom detonator. IEDs may be used in

terrorist actions or in unconventional warfare by guerrilla soldiers and insurgent forces in a theater of operations. Due to the simplicity, these devices are often encountered in the urban terrorist attacks [14, 15]. Some common methods of deploying IEDs in theater are in the form of a roadside bomb, as a car or suicide bomb or hidden in animal carcasses [16]. Similarly, in the urban terrorism these devices are placed in a densely populated (train stations) region or in public events (Boston marathon) to inflict maximum civilian casualties [15, 17].

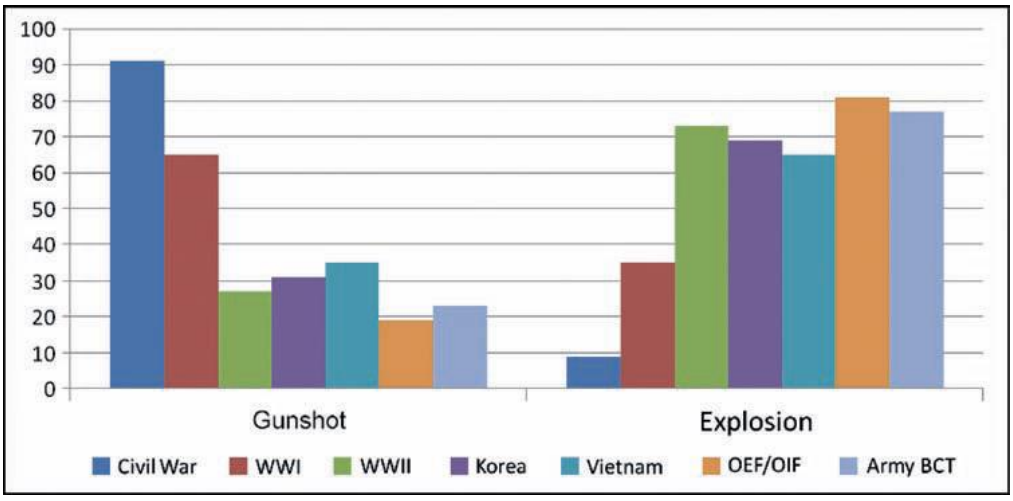

Figure 2.2: Percentage of mechanisms of injury from previous US wars (WIA). Source: [13]

Since Operation Enduring Freedom (OEF) and Operation Iraqi Freedom (OIF), the incidence of TBI among U.S. service members has been significantly higher. Out of this population, approximately 60% have never been assessed by a healthcare provider specifically for TBI. Department of Defense (DoD) based on data from 2004 to 2006 at

selected military installations has estimated that 10-20% of (the total deployed) OEF/OIF service members potentially sustain mTBI [18]. Other studies also report the occurrence of TBI in OEF/OIF veterans. For example, a recent study has found that 22.8% of soldiers in an Army Brigade Combat Team returning from Iraq had clinically confirmed TBI [19]. A survey of OEF/OIF veterans, who had left combat theaters by September 2004, found that about 12% of the 2,235 respondents reported a history consistent with mTBI [20]. Among those who have been medically evacuated from theater, the proportions who have suffered a TBI are predictably higher. For example, Between January 2003 and February 2007, 29 percent of the patients evacuated from the combat theater to Walter Reed Army Medical Center in Washington, DC, had evidence of a traumatic brain injury (TBI) [21]. Of 50 OEF/OIF veterans treated at the Tampa Veterans Affairs Polytrauma Rehabilitation Center, 80% had incurred combat related TBI, with 70% of the injuries caused by improvised explosive devices (IEDs) [22]. For active duty military personnel in war zones, blasts are the primary cause of TBI [9]. Recent statistics from the conflict in Iraq show that several thousand of active duty United States soldiers have sustained TBI; 69% of these as a result of blasts [23]. Analysis of data collected (collection period: March 2004 and September 2004) from 115 patients from the Navy–Marine Corps that were identified with TBI, have found that IEDs were the most common mechanism of injury responsible for 52% TBI cases overall [24]. The analysis also showed that intracranial injuries, particularly concussions, were the most common diagnosis category, especially among patients with non-battle injuries (94%). Although multiple TBI related diagnoses were common, 51% of the patient group had only an intracranial injury with no accompanying head fracture or open wound of the head. It was also found that out of 115 patients analyzed, about 63% of

patients were wearing helmet at the time of injury [24]. In addition to data reported above, Department of defense (DoD), in co-operation with the Armed Forces Health Surveillance Center (AFHSC) and Defense and Veterans Brain Injury Center (DVBIC), has consolidated the data of clinically confirmed TBI cases among service members and categorized them based on the severity of injury as shown in Figure 2.3 [25].

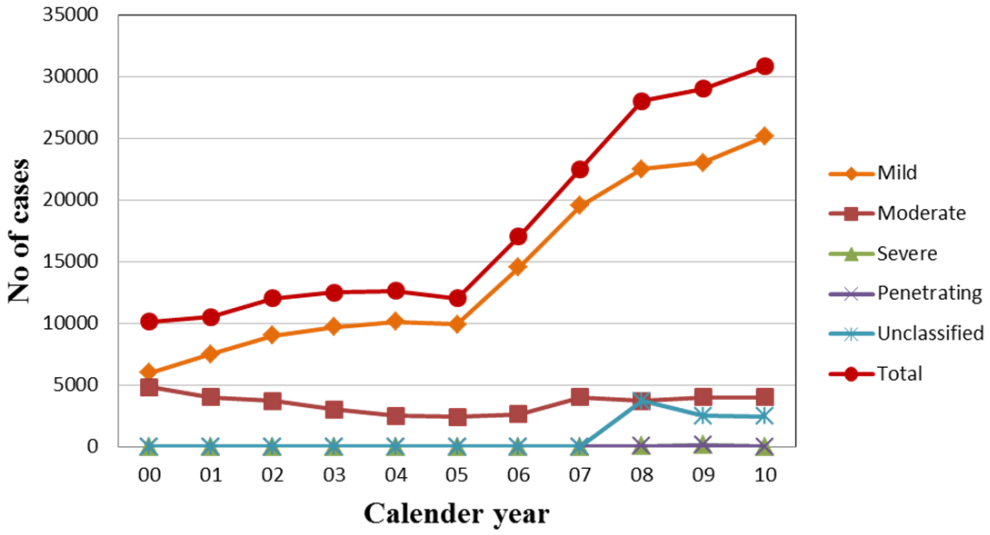

Figure 2.3: Blast Induced TBI in U.S. service members from year 2000 to year 2010 (source: Armed Forces Health Surveillance Center (AFHSC), (Department of defense (DoD). Accessed January 2012.)). These numbers are based on clinically confirmed TBI cases. mTBI contributes to more than 80% of the total reported brain injuries.

Mild TBI contributes to more than 80% of the total reported brain injuries (Fig. 2.3) as exposure to repeated low level blasts is a common feature of the war zone

personnel/civilian populations. Indeed, blast induced mild traumatic brain injury (bmTBI) has been identified as the signature injury of OEF and OIF [9, 23, 26, 27].

2.3. Explosions and shock-blast waves:

An explosion is a process of rapid physical or chemical transformation of a system into mechanical work. The work accomplished during an explosion is due to the rapid expansion of the gases formed at the time of the explosion. The most essential sign of explosion is the rapid jump in pressure (in few microseconds) in the medium surrounding the source of explosion, which is known as the shock blast waves or simply blast waves. Explosion can be due to chemical (plastic explosives, IEDs) or physical method (shock tube, explosion of boiler, and powerful discharges such as lighting). The ability of the chemical explosive transformation is determined by the following three factors: (a) extent of the exothermal reaction, (b) high rate of propagation and (c) presence of the gaseous products. [28].

Exothermicity or the evolution of heat is the first necessary condition without which the occurrence of an explosion process is not possible. The amount of exothermal energy of the reaction results in heating of the gaseous products, which leads to temperatures of several thousand degrees and rapid expansion of the gaseous products. Higher the heat of reaction and the rate of its propagation, greater is the destructive power of the explosion. High rate of the process is the most important criteria that distinguish a normal chemical reaction from an explosion. Although the energy content of chemical explosive is usually equivalent to that of a regular fuel, the time taken for the chemical to convert into gaseous

products is of the order of the microseconds, which distinguishes explosion from the regular combustion. Finally, the high pressure arising during the explosion and the destructive effect caused by them could not be achieved if the chemical reaction were not accompanied by the formation of a sufficiently large quantity of gaseous products. The products that are produced during the conversion of the chemical to gaseous products are the agents, which on expansion cause the extremely rapid change of the potential energy of the explosive into mechanical work [28, 29]. This mechanical work (sudden expansion of gas) is expended in propelling shrapnel/components of the bomb and it compresses the surrounding atmospheric air to initiate shock, which is associated with the primary blast injury.

A simplified hemispherical explosion is shown in Figure 2.4 (a). Depending on the length of the fireball radius (R), the blast is divided into three regimes, near field, far field and mid field [30]. Objects that are exposed to incident pressure of 1000 kPa or higher are typically within the fireball and considered as a near field condition. It is said within the near field condition the following is expected: (a) interaction with detonation products/shrapnel; (b) complex evolution of the waveforms; and (c) high gradients in the flow of temperature and density. In reality, flow conditions in the near field for IEDs are lot more complex due to the irregular charge shape, casing/shrapnel (where some of the kinetic energy of the blast is used for accelerating the shrapnel from the casing) and buried/grounded. It is extremely difficult to device a methodology to simulate the near field condition due to its shear unstable nature. Following the near field is the mid field and far-field, which is usually beyond the fireball expansion.

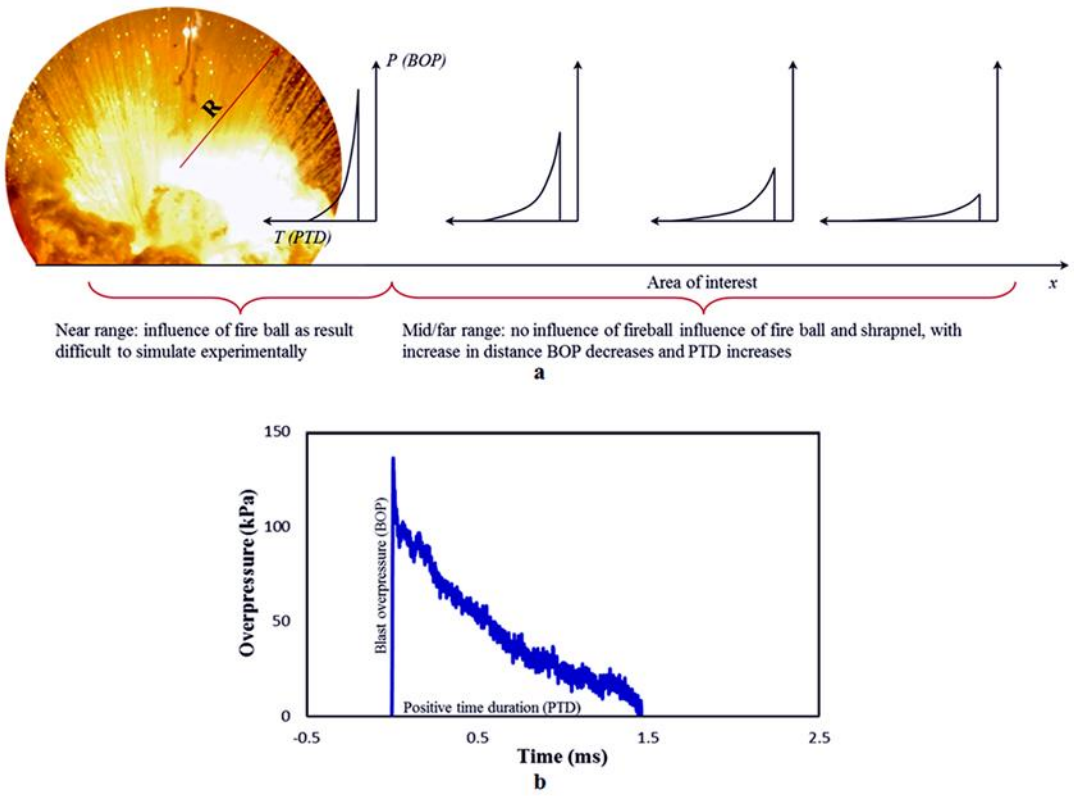

Figure 2.4: (a) shows evolution of shock-blast profile as the distance from the epicenter increases. Radius from epicenter with BOP higher than 1000 kPa is consider far range, which is very close to the fireball (R) and outside this radius it is mid and far field range, (b) Shock-blast wave profile generated from the explosion of 1.814 kg of C4 at a distance of 2.8 m.

Pressure profiles in the mid and far field have a similar form, i.e., decaying monotonically in amplitude and extending in duration with increased distance. Eventually, the wave loses its strength (i.e., Mach number < 1) and decays into a sound wave [29].

Explosive event from any explosive devices (such as IED, plastic explosive or nuclear weapon) for mid to far field can be quantified using a blast wave, which has time as an independent function and pressure as dependent function. Blast wave is a function of the overpressure, positive time duration, negative phase duration, and/or impulse. Figure 2.4 (b) shows the typical blast profile positive phase.

The shape of the positive phase of the mid to far-field blast is usually modelled as a Friedlander waveform which gives pressure values (p) as a function of time (t) (Eqn. 2.1).

$$p(t) = p_o \left(1 - \frac{t}{t_d}\right) e^{\left(\frac{-t}{\alpha}\right)} \qquad (2.1)$$

Where p_o represents the blast overpressure, t_d represents the PTD and α represents the time decay constant [29]. Although, this exponential decay reaches sub-atmospheric pressures generating a negative phase, Friedlander model does not take that into account [31].

2.4. Compressed gas driven shock tube and their use for simulating blast wave

In the last section, a review about basics of chemical explosion including different phases of explosion and basic requirement for generating a shock was discussed. One of the main objectives of this work is to establish a standardized method to replicate field relevant blast conditions (without other artifacts of the field explosion) to study primary blast condition. In this section, we will review groups that currently utilize gas driven shock tube (physical method, i.e., no chemicals involved) for generating blast wave. Currently, there are number of researchers, who investigate blast TBI using compressed gas shock tubes. Table 2.1 from

a review article by Kobeissy and his colleagues shows the recent major studies on primary blast injury [32]. The paper shows that out of 49 studies, only 8 used field testing; further almost 92% of shock tubes (33 out of 36) used compressed-gas driven shock tubes. Furthermore, the table also shows the test section location, strength of the blast wave along with the animal tested.

Table 2.1 Recent major studies on experimental blast injury with loading parameters (overpressure) and location of the test section and specimen used.

Reference	**Model / Device used-BOP Intensity**	**BOP (kPa)**	**Test section location (Inside/outside)**
[33]	Rat / Primary blast/ shock tube	123	Inside the shock tube
[34]	Rat / Compressed air-driven shock tube	138	Outside the shock tube
[35]	Mouse/A compressed air-driven shock tube	145	Outside the shock tube

[36]	Rat/Pneumatically driven shock tube	116.7, 74.5 and 36.6	Outside the shock tube
[37]	Rat/ Composite blast with head acceleration & Primary blast with no acceleration/	230-380	Outside the shock tube
[38]	Rat/ Compressed air-driven shock tube ~2 m distance /	358	Outside the shock tube
[39]	Mouse/ Compressed gas-driven shock tube	145	Inside the shock tube
[40]	Rat/Helium driven shock tube	130, 190, 230, 250, & 290	Inside the shock tube
[41]	Mouse/ blast overpressure/	142	Outside the shock tube

[42]	Rats/Tabletop shock tube	213, 345, 497, and 690	Outside the shock tube
[43]	Rat/Blast chamber (Compression wave attached to a PVC tube)	129.23	Inside the shock tube
[44]	Rat/ Air-driven shock tube	120	End of the driven section
[45]	Rat/Gas-driven shock tube, 90, 103, 117, 193, 159 kPA	90, 103, 117, 159 and 193	Inside the shock tube
[46]	Rat/ Shock tube/	142	Inside the shock tube
[47]	Ferrets/8 inch shock tube/	98-818	Outside the shock tube

[48]	Pigs/Compressed-gas shock tube/variable	107-740	Outside the shock tube
[22]	Rat/compressed gas Shock tube/	100, 150, 200 and 225	Inside the shock tube
[49]	Rat/Air blast shock tube	74.5	Outside the shock tube
[50]	Rat/ Compressed air-driven shock tube	120	not reported
[51]	Compressed air-driven shock tube	94.30, 125, and 145	Inside the shock tube
[52]	Rat/ Air-driven shock tube/	36	End of the shock tube; furthermore, incident pressure were flattop wave

[4]	Mouse/Helium modular, multi-chamber shock tube/mild	183, 213, and 295	Inside the shock tube
[53]	Mouse/ Helium multi chamber shock tube	165.5-310, 182.7	Inside the shock tube
[46]	Rat/Compression-driven shock tube	138	Not reported
[54]	Rat/large-scale BT-I shock tube	338.9 and 440	Not reported
[18]	compressed air/helium driven tube mode, or oxyhydrogen –RDX explosives mode	100, 150, and 200	Inside the shock tube
[55]	Rat/blast tube with pressure wave/	130 & 260	Inside the shock tube

[56]	Female Guinea pig/ shock tubing	23, 41 and 64	Not reported
[57]	Rat/Helium-driven shock tube/	242	Inside the shock tube
[58]	Pig/ compression-driven shock tube	138, 138 – 276, and 276	Not reported
[59]	Rat/Air-driven shock tube	120	End of the tube
[60]	Rat/compression-driven shock tube/	126, and 147	Outside the shock tube
[61]	Rat/ Shock tube	10, 30, and 60	Inside the shock tube

Although there are a number of researchers who investigate blast TBI using animal models, we have noticed significant diversity among them (Table 2.1). There are no standardized methods to simulate field conditions (e.g. chemical explosives, shock tube design), location

of the specimen or the type of animal model employed. All these factors result in the development of general bTBI theories extremely challenging. Considering the complexity of the variations in the test methodologies, comparison of the results between different laboratories is virtually impossible.

2.5. Animal models to study blast induced injury mechanics

In this section, we will review the current methods in which researchers develop animal models and use it to measure intracranial pressure. Brain injury due to BINT is a complex process that comprises an acute injury phase followed by sub-acute and chronic biomechanical and biochemical sequelae. Consequently, a lot of work has been done using animal models (refer to Table 2.1), head surrogates, post-mortem human specimens (PMHS) with shock tubes along with computer models in the past few years to understand the pathophysiology of blast-induced TBI (bTBI), which may differ significantly from the mechanisms associated with blunt and ballistic head injuries. Among these studies, animal models are an ideal choice for studying pathophysiological, complex bio and neurochemical processes along with the long-term cognitive and behavioral ailments.

When simulating field conditions to model primary blast injury, it is important that any experimental model (in vivo or in vitro) satisfy the following criteria: (i) the biomechanical loading conditions (the injury cause) are replicated as accurately as possible, (ii) the mechanical forces used to induce injury are controllable, quantifiable and reproducible, (iii) the inflicted injury is quantifiable, reproducible and mimics the components of human conditions, (iv) the injury outcome is free of any loading artifacts and is related to the

mechanical force causing the injury, and (v) the intensity of the mechanical force used to inflict the injury should predict the outcome severity [62]. In the following section, brief account on the current models using animals to study blast induced loading such as skull strain and intracranial pressure (ICP) will be discussed.

In 2007, Chavko and his colleagues [63], investigated pressure changes induced due to exposure to blast inside the rat brain (i.e., ICP). A FISO sensor was placed in the third ventricle of an anaesthetized rats exposed to 40 kPa blast wave in a gas driven shock tube. The main goal of this research is to establish an experimental animal model to measure the level of transmission through the skull. They found that for an incident pressure of 45 kPa an intracranial pressure of approximately 40 kPa was recorded. In 2011, the same research group did an animal model study in this case with the different orientation of animal with respect to the plane of shock front: (a) head facing, (b) right torso side exposed, and (c) head facing away (abdomen facing blast). The incident pressure used was approximately 35 kPa. They determined that ICP measured depends on the orientation of the animal. For instance, frontal exposure resulted in pressure traces of higher amplitude and longer duration, suggesting direct transmission through the head to brain. In the case of animal facing away from the shock front, ICP measured was equivalent to the incident pressure [52].

In 2011, Leonardi and her colleagues investigated the critical stresses that are inflicted on brain tissue from blast wave encounters with the head by recording ICP of the brain of male Sprague-Dawley rats. The goal was to understand pressure wave dynamics through

the brain. In addition, they optimized *in vivo* methods to ensure accurate measurement of ICP. Their results demonstrate that proper sealing techniques lead to a significant increase in ICP values, compared to the outside overpressure generated by the blast. Further, the values seem to have a direct relation to a rat's size and age: heavier, older rats had the highest ICP readings. They concluded that a global flexure of the skull by the transient shockwave is an important mechanism of pressure transmission inside the brain [64].

In 2011, Bolander continued on the work done by Leonardi on examining the ICP on rats exposed to blast and deduce a relationship between ICP and skull flexure through examining the recorded skull strains. Biomechanical responses of the rat head under shock wave loading were measured using strain gauges on the skull surface and a fiber optic pressure sensor placed within the cortex. MicroCT imaging techniques were applied to quantify skull bone thickness. The strain gauge results indicated that the response of the rat skull is dependent on the intensity of the incident shock wave; greater intensity shock waves cause greater deflections of the skull. ICP sensors indicated that the peak pressure developed within the brain was greater than the peak side-on external pressure and correlated with surface strain. The bone plates between the lambda, bregma, and midline sutures are probable regions for the greatest flexure to occur. They concluded that skull flexure is a likely candidate for the development of ICP gradients within the rat brain [65].

In 2013, Skotak and his team [66] studied the biomechanical loading with pressure gauges mounted on the surface of the nose, in the cranial space, and in the thoracic cavity of cadaver rats. The rats were exposed to 130, 190, 230, 250, and 290 kPa pressure. They

found that, the reflected (nose sensor), and intracranial pressures are higher than the incident pressure; however, there are no clear differences between reflected pressure and ICP. Moreover, the ICP not only is higher than the incident pressure but also shows an oscillatory tendency. While the reflected pressure shows a monotonic increase with side-on pressure for all the pressure groups (130, 190, 230, 250, and 290), the same cannot be said for the ICP: there are no statistically significant differences between groups 190 and 230 kPa. Finally, it was concluded that the outcome is not a function of the total energy transferred to the brain but depends on the specific response of the cranium, which is very similar to the findings of (Leonardi and Bolander 2011). Leonardi and her colleagues designed a complex wave testing system to perform a preliminary investigation of the ICP response of rats exposed to a complex-blast wave environment (blast wave generated by involving shock reflections and/or compound waves from different directions to simulate an enclosure). Finally, the effects of head orientation in the same environment were also explored. Their results demonstrated that, regardless of orientation, peak ICP values were significantly elevated over the peak incident pressures. It was found that exposure to a complex shock wave was more injurious as compared to a free-field scenario at equal pressure magnitudes. Furthermore, results indicated consistent and distinct pressure time profiles in brain depending on the orientation, as well as distinctive values of impulse associated with each orientation. Finally they concluded that the geometry of the skull and the way sutures are distributed on them are responsible for the difference in the stresses observed [67].

2.6. Computational animal models in BINT

Unlike conducting experiments on post-mortem human subjects or human volunteers, conducting experiments on rats to understand TBI is easier. Therefore, unlike human computational models, animal computational model is not often used in the study of BINT. As a result, only a few computational animal models have been reported in the literature. In this section, we will review all the animal models to date (pertaining to TBI), describe their pros (if applicable) and cons along with their findings using the model.

In 1978, Ward and his coworkers generated three-dimensional finite models for the monkey, baboon, and human brains using isoparametric brick elements and membrane elements to represent the soft tissue and partitioning internal folds of dura, respectively. By specifying the finite element mesh on the skull inner surface, the irregular shape of the brain is generated. Each model was subjected to the same skull acceleration to investigate response relationships between species. Important dynamic response differences were revealed by comparing the computed ICP. Experimentally derived head injury data are correlated with model dynamic responses. Using the baboon and monkey models, brain injury tests are simulated and model response measures are compared to produced injury. Using the human model, computed stresses are compared to intracranial pressures measured in cadaver impact tests [68]. In 1980, they extended the model to determine injury threshold for a crash scenario. They determined that brain injury severity correlates with peak ICP, with serious and fatal injuries occurring when the pressures exceeded 34 psi. Using this value as the maximum allowable brain stress, they deduced the tolerance

curves for frontal and occipital impacts, which represent four head acceleration pulse shapes and impact durations between 1 and 10 msec [69].

Lee and his coworkers developed a two-dimensional finite element model of the head of a rhesus monkey to simulate the head acceleration experiments. The purposes of the study were to understand the mechanisms of traumatic subdural hematoma and to estimate its threshold of occurrence. They treated brain as an isotropic homogeneous elastic material with and without structural damping and the skull was treated as a rigid shell. The head model was then subjected to an enforced forward rotation around the neck. The loading had an initial acceleration phase followed by deceleration. During both acceleration and deceleration phases, high shear stress, (and thus strain) occurred at the vertex, where the parasagittal bridging veins are located. Finally, from the model they concluded that the deformation of bridging vein depended on its orientation relative to the direction of impact. Bridging veins that drain forward into the superior sagittal sinus would be stretched during the acceleration phase and would be compressed during deceleration. Therefore, subdural hematoma may have occurred during the acceleration phase in the primate experiments, in contrast to [70] belief that this phase could be neglected in analyzing the subdural hematoma data [71]. In 1992, Mendis developed a baboon model to demonstrate the feasibility of using finite element modeling techniques to extrapolate animal model rotational head injury data to estimate corresponding human injury thresholds. The baboon model was built of rigid skull containing brain, falx and tentorium. He was able to develop a relationship between deformation response of the model and different grades of diffused axonal injury [72].

In 1994, Zhou developed a two dimensional model of three coronal sections porcine brain. All the three models consisted of skull, dura, cerebrospinal fluid (CSF), white matter, gray matter, and ventricles. Model 1, a section at the septal nuclei and anterior commissure level, contained 490 solid elements and 108 membrane elements. Model II, a section at the rostral-thalamic level, contained 644 solid elements and 130 membrane elements. Model III, a section at the caudal hippocampal level, contained 548 solid elements and 104 membrane elements. They assumed plane strain for all the models and material model was adapted from previous publications. A prescribed angular velocity was applied to the outer table and impact responses were computed. The maximum shear stress distribution produced from the models was in good agreement with experimental findings. Furthermore, diffuse axonal injury as indicated by the experiments was found in areas of high shear stress, which persisted for relatively longer periods during the impact. Finally, they concluded that the shear stress or strain could be the cause of diffuse axonal injury [73].

In 2005, Pena and his colleagues developed a two dimensional rat brain model based on high-resolution T-2 weighted MRI images of rat brain, to simulate displacement, mean stress, and shear stress of brain during controlled cortical impact. Furthermore, they did a parametric study by varying the material model depending on the Intensity of the MRI to study the effect of material properties in their results. They found that the tissue displacement did not vary significantly; however, mean stress and shear stress were largely different. They concluded that finite element analysis seems to be a suitable tool for biomechanical modeling and having an accurate material model for tissue is essential to do

post processing analysis [74]. In 2006 Levchakov and her colleagues developed an age specific three dimensional finite element rat model and subjected it to cortical impacts to study the effect of the brain stiffness (it was found out from literature that stiffness of brain tissue is high in the case of younger rats). They determined that for identical cortical displacements, the neonatal brain might be exposed to larger peak stress magnitudes compared with a mature brain due to stiffer tissue properties in the neonate, as well as larger strain magnitudes due to its smaller size. The brain volume subjected to a certain strain level was greater in the neonate brain compared with the adult models for all indentation depths greater than 1 mm. They concluded that the larger peak stresses and larger strain volumetric exposures observed in the neonatal brain support the hypothesis that the smaller size and stiffer tissue of the infant brain makes it more susceptible to TBI [75].

In 2006, Mao developed an anatomically detailed high-resolution finite element model of the rat brain. The model was then validated against *in vivo* measured brain displacement data from dynamic cortical deformation study reported in literature. It was then used to predict biomechanical responses within the brain due to different series of cortical impact experiments by various research groups published in literature. The strain, strain rate, and surface pressure predicted by the computer model were analyzed and compared to contusive brain injury, neuron damage, and axonal dysfunctions observed in animal model. It was found that high strains correlated well with experimentally reported contusions, hippocampal cell injury and cortex axonal dysfunction several days post injury [76]. In 2010, they used the same model to study intracranial responses in a series of cortical impact

experiments in which injury severity ranged from mild to severe. A linear relationship was found between the percentage of the neuronal loss observed in vivo and the FE model-predicted maximum principal strain ($R^2 = 0.602$). Interestingly, the FE model also predicted some risk of injury in the cerebellum, located remote from the point of impact, with a 25% neuronal loss for the ‘‘severe’’ impact condition [77]. In this study, a design of computer experiments was performed with typical external impact parameters commonly found in the literature. An anatomically detailed finite element (FE) rat brain model was used to simulate the CCI experiments to correlate external mechanical parameters (impact depth, impact velocity, impactor shape, impactor size, and craniotomy pattern) with rat brain internal responses, as predicted by the FE model. Systematic analysis of the results revealed that impact depth was the leading factor affecting the predicted brain internal responses. Interestingly, impactor shape ranked as the second most important factor, surpassing impactor diameter and velocity, which were commonly reported in the literature as indicators of injury severity along with impact depth. The differences in whole brain response due to a unilateral or a bilateral craniotomy were small, but those of regional intracranial tissue stretches were large. The interaction effects of any two external parameters were not significant. This study demonstrates the potential of using numerical FE modeling to engineer better experimental TBI models in the future [78].

Zhu in 2011 developed a rat head model based on a previous rat brain model by Mao and his colleagues for simulating a blunt controlled cortical impact [76]. An FE model, which represents gas flow in a 0.305-m diameter shock tube, was formulated to provide input (incident) blast overpressures to the rat model. It used an Eulerian approach and the

predicted pressures were validated with experimental data. These two models were integrated and an arbitrary Lagrangian-Eulerian (ALE) fluid-structure coupling algorithm was then utilized to simulate the interaction of the shock wave with the rat head. The model predicted pressure-time histories at the cortex and in the lateral ventricle were in reasonable agreement with those obtained experimentally. Further examination of the model predictions revealed that pressure amplification, caused by shock wave reflection at the interface of the materials with distinct wave impedances, was found in the skull. The overpressures in the anterior and posterior regions were 50% higher than those at the vertex and central regions, indicating a higher possibility of injuries in the coup and countercoup sites. They concluded that at an incident pressure of 85 kPa, the shear stress and principal strain in the brain remained at a low level, implying that they are not the main mechanism causing injury in the current scenario [20]. In 2013 Zhu developed a pig model to investigate the biomechanical responses of the pig head under a specific shock tube environment. A finite element model of the head of a 50-kg Yorkshire pig was developed with sufficient details, based on the Lagrangian formulation, and a shock tube model was developed arbitrary Lagrangian–Eulerian approach. These two models were integrated and a fluid/solid coupling algorithm was used to simulate the interaction of the shock wave with the pig's head. The finite element model was validated with the experimentally obtained incident and intracranial pressures and there was reasonable agreement with the simulation results. Using the validated numerical model of the shock tube and pig head, further investigations were carried out to study the spatial and temporal distributions of pressure, shear stress, and principal strains within the head. Pressure enhancement was found in the skull, which is believed to be caused by shock wave reflection at the interface

of the materials with distinct wave impedances. Brain tissue has a shock attenuation effect and larger pressures were observed in the frontal and occipital regions, suggesting a greater possibility of coup and countercoup contusion. Shear stresses in the brain and deflection in the skull remained at a low level. Higher principal strains were observed in the brain near the foramen magnum, suggesting that there is a greater chance of cellular or vascular injuries in the brainstem region

2.7. Scaling laws currently developed

Scientific literature on development of scaling relations for blast injury has a long history. However, most of these laws were developed for scaling pulmonary injury and not brain injury. Richmond and his associates were one of the very first to conduct extensive experimental studies of blast overpressures on mouse, guinea pigs, rats and rabbits using shock tubes to study blast lung injury [79] and Bowen and his colleagues were very first to develop scaling relations between blast parameters and body parameters [80]. In an effort to develop lung injury threshold for human from animal testing, Bowen and co-workers derived scaling based on dimensional analysis. Scaling laws developed by Bowen and co-workers are shown below; the most important relating blast parameters to body parameters are marked in bold. These scaling relations of Bowen were widely used to scale overpressures and durations across species (Eqn. 2.2) [81-84] and [85].

$$R = K_1;\ \frac{P}{P_o} = K_2;\ t\frac{P_o^{1/2}}{m^{1/3}} = K_3;\ \frac{P\prime}{P_o} = K_4 \qquad (2.2)$$

Where, *K's*: Constants, *R*: Any non-dimensional index of biological response, e.g., percent mortality or percent increase in lung mass, *P*: Any characteristic pressure of the pulse occurring in the lungs, such as peak pressure, P_o: Ambient pressure, *t*: Any characteristic time of blast waves of similar shape, or of the internal pressure waves; e.g., duration of the blast wave, time to reach maximum intrathoracic overpressure, *m*: Body mass of similar animals, *P'*: Any characteristic pressure of blast waves of similar shape, e.g., peak pressure.

At about the same time Ommaya and his collegues developed scaling relations (based on Holbourn's theory) to scale experimental concussion data on sub-human primates to concussion threshold in man [86]. The primates were subjected to head impact and whiplash in order to produce concussions in them [87]. Authors initially assumed and later confirmed rotational acceleration as a main mechanism responsible for concussion. Similar relations were developed by Margulies [88] and Gibson [89] based on Holbourn's theory. The scaling relations of Ommaya [86] and Margulies [88] are shown below (Eqn. 2.3)

$$\ddot{\theta} = \frac{C}{M^{2/3}};\ \dot{\theta} = \frac{C}{M^{1/3}} \qquad (2.3)$$

Where, $\ddot{\theta}$ – angular/rotational acceleration, $\dot{\theta}$ – angular/rotational velocity, *M* – mass; *C* – constant. Stalnaker and his collegues developed scaling relations by grouping variables to form dimensionless quantities (Eqns. 2.4, 2.5, and 2.6). Three scaling parameters were obtained: species scaling parameter, velocity scaling parameter and acceleration scaling parameter and those parameters are defined as:

$$\textit{Species scaling parameter} = Wa/h \qquad (2.4)$$

$$Velocity\ scaling\ parameter = Vt/h \quad (2.5)$$

$$Acceleration\ scaling\ parameter = Ah/V_2 \quad (2.6)$$

Where, *W*- brain weight, *a*- skull radius, *h*- skull thickness, *V*- velocity of impact, *A*- linear head acceleration, *t*- acceleration pulse duration. Stalnaker and his colleagues [90] used these scaling relations to determine tolerable impact velocity and impact acceleration for human head against side impact based on experiments on primates. Species scaling parameter was plotted against velocity scaling parameter and acceleration scaling parameter for various primates and those results were extrapolated to obtain velocity and acceleration for human. The pulse duration of 20 ms was used for human based on MSC curve.

These scaling relations developed by [91] were further used by [92] to develop human head tolerance curve to sagittal impact. In addition, he also validated scaling relations developed by [91] by comparing human cadaver skull fracture threshold against monkey skull fracture threshold. A reasonably good match was obtained between scaled money skull fracture thresholds with human cadaver skull fracture thresholds.

Zhang et al. reproduced twenty-four head-to-head field collisions that occurred in professional football games using laboratory based accident reconstruction on hybrid III dummy and finite element modeling [93]. In this effort, attempts were also made to relate head kinematics with injury parameters. They found that pressure in the brain relates well with resultant translational acceleration ($R^2 = 0.77$) and shear stress in the brain relates well with the resultant rotational acceleration ($R^2 = 0.78$). Relations between pressure and resultant translational acceleration; and shear stress in the midbrain and resultant rotational acceleration were established. In

addition, it was also found injury probability curves based on pressure, shear stress in the midbrain, resultant translational and rotational accelerations and head injury criterion (HIC) [93].

2.8. Summary

In this chapter, literature relevant to this research work was reviewed. Clinical data clearly indicate that the number of injury due to blasts have significantly increased when compared to injuries due to ballistics since American civil war. It is also postulated, in the literature, that field conditions implicated in the primary blast induced TBI (bTBI) are free from secondary, tertiary and quaternary effects and blast wave profile assumes Friedlander type waveform typically seen in the far field range. A list of researchers who use compressed gas shock tube to simulate the aforementioned conditions is generated from the review. Furthermore, the variations in the test methodology especially the test section location were indicated in the table. A comprehensive review of animal models to study blast induced injury mechanics was done. It was determined that the intracranial pressure measured within the brain is always higher than the incident pressure. It was shown that there is a correlation between skull thickness and intracranial pressure measured. Furthermore, it was determined that the bone plates between the lambda, bregma, and midline sutures have a higher intensity of the skull flexure and hence ICP. Consequently, it was shown that skull flexure along with direct transmission to be an important mechanism for BINT. Finally, a review of the current scaling laws was discussed. In spite of several experimental evidence that showed mechanism of lung injury varies significantly from the mechanism of brain injury. Scaling based on the mass of the species, which was

initially developed for scaling pulmonary injury is used for scaling mortality and injury thresholds of brain injury across species.

CHAPTER 3: LABORATORY MODELING OF SHOCK-BLAST WAVE TO STUDY TRAUMATIC BRAIN INJURY RELEVANT TO THEATER

3.1. Introduction

In the study of Blast Induced Neurotrauma (BINT) and in the development of animal models, many research groups use compressed gas driven shock tubes to simulate primary blast injury conditions [4, 18, 52, 65, 94, 95]. Since the injury to animals critically depends on the nature of the blast wave, it is important to standardize the mechanical insult across the various shock tubes used as the injury device. Further, if these blast profiles can be correlated with pressure measurements carried out under field explosions, then the results from these works will become translational. Though the generation of blast wave by itself is not complicated, controlling the shape and magnitude of the blast profile is not trivial. A compressed gas driven shock tube has been used to generate a blast wave without the artifacts of the high explosives (HE) in the primary blast injury testing. Accurately simulating blast wave in laboratory condition using a compressed gas shock tube requires the ability to control Shock-blast wave parameters (SWPs) independently. In this chapter, an extensive experimental analysis has been carried out to show the methods in which the blast wave profile can be tailored to replicate the field conditions. We study the effects shock tube adjustable parameters (SAPs) such as breech length, type of gas, membrane thickness, and measurement location has on the SWPs. Furthermore, we characterize the

flat top or plateau wave and determine the influence, driver gas and breech length has on this phenomenon. Finally, we compare the blast wave profile from the shock tube with the field explosion profiles generated in ConWep (Conventional Weapons effects).

3.2. Methods

3.2.1. Shock tube

Experiments were carried out in the shock tube designed by our group and tested at the University of Nebraska-Lincoln's blast-wave generation facility (Figure 3.1) [96]. The four main components of any compressed-gas driven shock tube are driver, transition, driven sections and catch tank. The driver section (breech) contains pressurized gas (e.g., Nitrogen, Helium) which is separated from the transition by several frangible Mylar® membranes, while the driven section (including the expansion section) contains air at atmospheric pressure and room temperature.

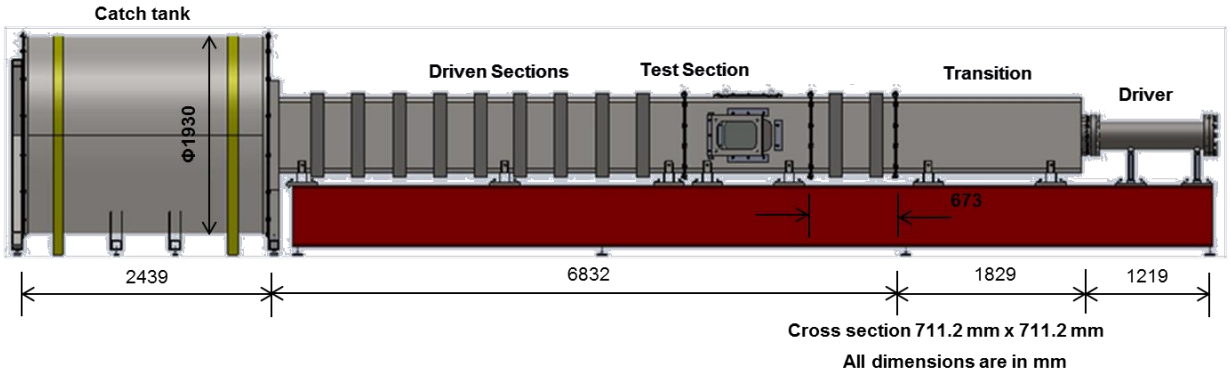

Figure 3.1:711 × 711mm shock tube system

Transition section acts as an adapter, which is used to change the cross-section of the tube from a circular (breech) to a square (expansion section); the square section is a design element to observe events in the test section with high-speed video imaging. The driven section has a 711.2 mm × 711.2 mm (28 in. × 28 in.), cross-section, and the length of 8661 mm. Upon membrane rupture, a blast wave is generated, which expands through the transition and develops into planar blast waveform in the driven section. Driven section also encompasses the test section. Finally, the blast wave exits the shock tube and enters the catch tank, which reduces the noise intensity. The cross-sectional dimension of this shock tube is designed such that subjects within the test section experiences a planar blast wave without significant sidewall reflections. The planarity of the blast wave is verified by pressure measurements across the test section of the shock tube [97].

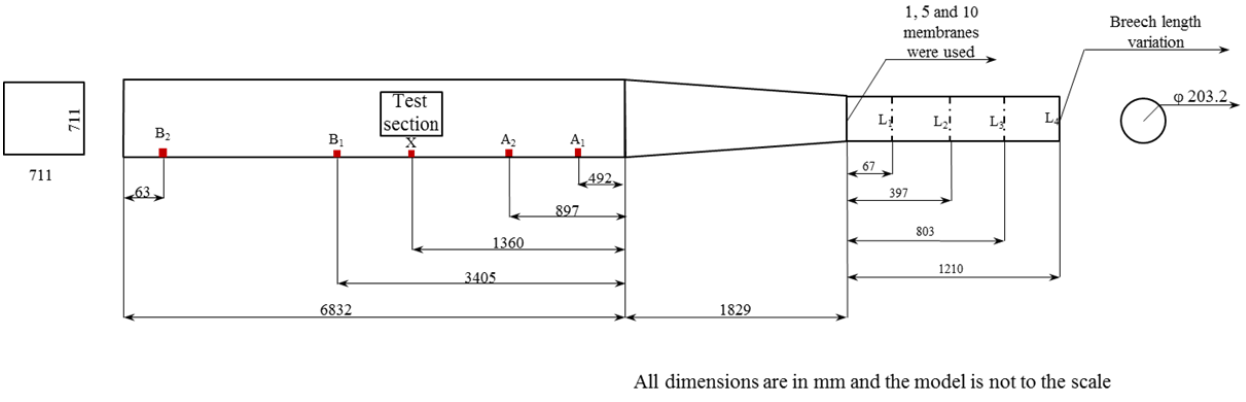

Figure 3.2: Experimental variables and sensor location; here A1, A2, X, B1, and B2 are the side-on pressure sensors.

Figure 3.2 shows the experimental variables and the sensor locations. The length of the breech is varied with discrete increments designated as L_1 (66.68 mm), L_2 (396.88 mm), L_3

(803.28 mm), and L4 (1209.68 mm). The membrane thickness is varied by varying the number of membranes between 1, 5, and 10 (each membrane is 0.254 mm thick). In this work, both nitrogen and helium were used as the driver gas, and the driven gas was air at ambient laboratory conditions (temperature range of 23 ± 2 °C). The evolution of the blast wave along the length of the shock tube was measured using PCB pressure gauges (model 134A24) mounted on the wall of the shock tube at locations A1, A2, X, B1and B2 (Figure 3.2). Burst pressure in driver just before the rupture of the membranes was also recorded.

3.3. Results

3.3.1.Burst pressure

Burst pressure is the pressure in the driver section (breech) at the time of the membrane rupture. This highly compressed gas when allowed to expand rapidly compresses the atmospheric air in the transition and driven sections generating a shock front. Burst pressure for different membrane thicknesses and breech lengths are shown in Figure 3.3. From Figure 3.3, it can be seen that the burst pressure increases with an increase in the membrane thickness. Furthermore, there is no discernible difference in the burst pressure with respect to increase in breech length for any of the three membrane thicknesses studied. It should be noted that any variation in the burst pressure for identical conditions (e.g. number of membranes. Breech volume and type of gas) will be due to the variations in filling rate of gas in the breech; since mylar® membranes are viscoelastic in nature they will deform differently if the rate of the pressurization is different due to different fill rates.

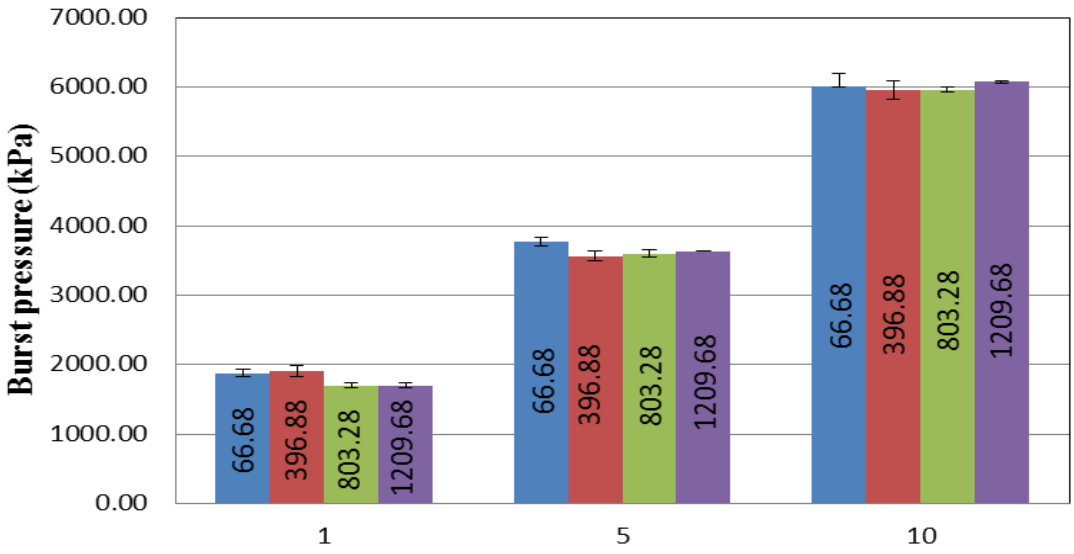

Figure 3.3: (a) Relationship between the number of membrane used and burst pressure produced with respect to different breech lengths.

3.3.2. Shock tube adjustable parameters (SAPs) and their influence on the Shock-blast wave parameters (SWPs) in test section

By changing the SAPs such as membrane thickness (burst pressure) and breech length, we can alter the SWPs such as Mach number, blast overpressure (BOP), and positive time duration (PTD) in the test section. Figure 3.4 (a) shows the relationship between Mach number and burst pressure for different breech lengths used. Here Mach number of the shock front refers to the ratio of the velocity of the shock in the given medium to the velocity of sound in the same medium. Mach number of the shock front depends on the burst pressure and has a positive linear relationship with burst pressure, i.e., shock front velocity increases with an increase in the burst pressure. When breech length is L_1 (small)

Mach number increases at a lower rate (slope of the line) compared to that of the other lengths (L_2, L_3, L_4). How and why the behavior for shorter breech length is different from that of the others will be discussed later.

Blast overpressure is the gauge pressure measured in the air, which is the difference between absolute pressure and atmospheric pressure. Similar to Mach number, there is a linear relationship between BOP and burst pressure (Figure 3.4 (b)). Furthermore, with increase in the burst pressure the BOP for L_2, L_3, L_4 increases with a higher rate (higher slope) compared to that of L_1. These Results are intriguing and are explained in the discussion section.

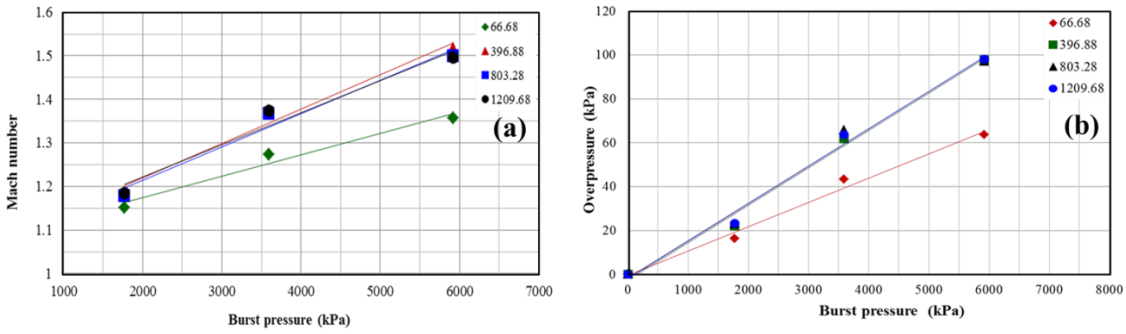

Figure 3.4: (a) Relationship between shock front Mach number and burst pressure, there is linear relationship between Mach number and burst pressure (with strength of linearity R^2 between 0.96 to 0.98), (b) describes the relationship between shock tube parameter burst pressure with overpressure measured in the test section for different breech lengths.

Positive time duration is the period when the BOP reduces to zero, i.e., when it reaches the local atmospheric pressure. Figure 3.5 shows the relationship between PTD and membrane

thickness for different breech lengths. For a given membrane thickness, PTD increases with an increase in the breech length. Furthermore, there is an increase in PTD between membrane thicknesses 1 and 5 for breech lengths L_1, L_2, and L_3; however, such an apparent difference is not observed between membrane thicknesses 5 and 10. Finally, for breech length *L4* there is no apparent difference in PTD for different membrane thicknesses.

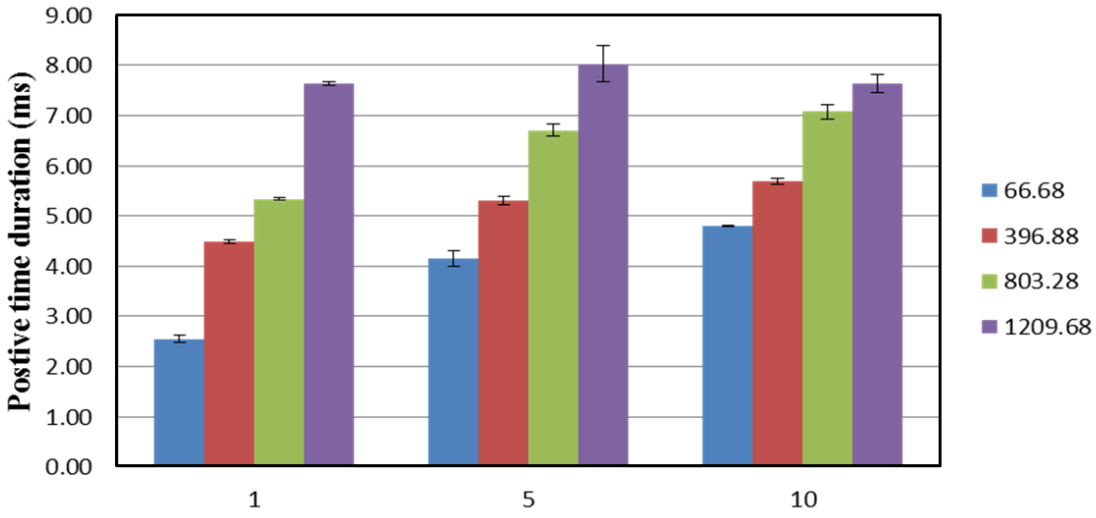

Figure 3.5: Relationship between Positive Time Duration (PTD) and membrane thickness used for different breech lengths. It can be seen that there PTD increases with increase in the breech length for any given membrane configuration; furthermore, for a lower breech. For all cases with breech length L_1, there is a continuous decay in the BOP downstream of the shock tube. For all the other breech lengths, unique points of BOP decays are identified along the expansion section, which is illustrated in the following section.

3.3.3. Evolution of the shock-blast wave along the expansion section

Figures 3.6 (a) (b) and (c) show the evolution of the BOP along the length of the expansion section. From Fig 3.6 (a), it can be seen that, for one membrane there is no discernible change in BOP for breech lengths L_2, L_3, and L_4. For L_1, L_2, L_3 and L_4, we observe the following: (i) for any membrane thicknesses, an obvious difference in BOP is observed between L_1 and other breech lengths (figure 3.6 (a) (b) and (c)), (ii) Beyond 3000 mm from the breech, for 5 and 10 membranes and breech length L_2, BOP starts to decay (Figure 3.6 (b) and (c)), and (iii) Beyond 5000 mm from the breech, for 10 membranes and breech lengths *L3*, the BOP starts to decay (Figure 3.6 (c)). Finally, for L_4 there is no unique decay point, which implies a flat top wave throughout the expansion section.

Figures 3.6 (d) (e) and (f) show the evolution of the PTD along the length of the shock tube expansion section. For any given breech length and membrane thickness, the PTD remains reasonably constant along the length, however, decreases drastically towards the exit of the shock tube. Positive Impulse (PI) is the area under the shock-blast wave profile. Figure 3.6 (g) (h) and (i) show the evolution of the PI along the length of the shock tube expansions section. PI is a function of both overpressure and PTD; hence, it increases with an increase in both membrane thickness and breech length. Due to its relationship with the PTD, the impulse drastically reduces near the exit of the shock tube.

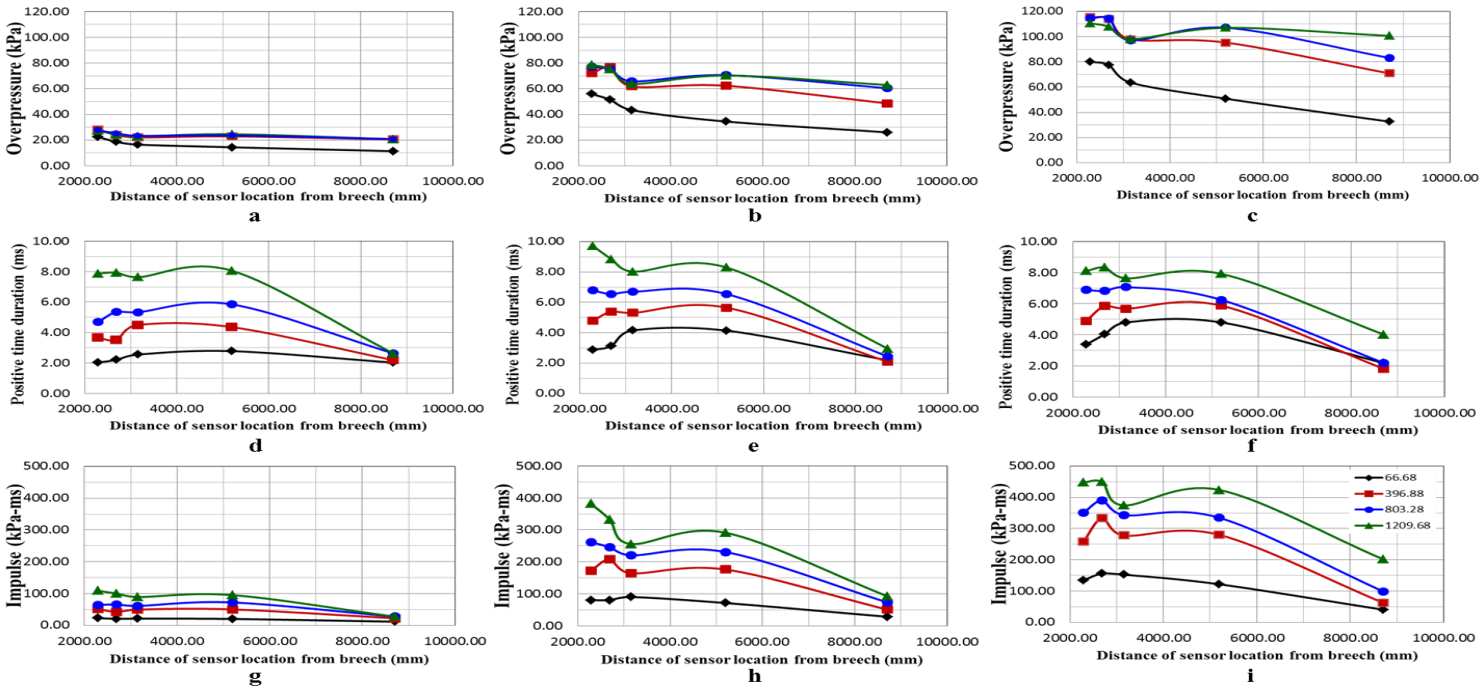

Figure 3.6: Describes the variation of shock-blast profile parameters along the length of the shock tube expansion section; All these experiments were performed for breech lengths 66.68 (black), 396.88 (red), 803.28 (blue) and 1209.68 (green) mm; (a), (b) and (c)show the variation of overpressure along the length of the expansion section for burst pressures corresponding to 1, 5 10 membranes respectively; (d), (e) and (f) show the positive time duration along the expansion section for burst pressures corresponding to 1, 5 10 membranes respectively.

3.3.4. Flattop or plateau wave

A flattop or plateau wave is usually witnessed in a gas driven shock tube [18]. In this case, the shock-blast wave profile once reaching the peak overpressure maintains its peak value for a certain period before decay. Longer breech lengths in combination with the use of nitrogen as a driver gas seems to have a strong influence on this phenomenon. Figure 3.7 shows the comparison between the shock-blast wave profile with nitrogen and helium as driver gas.

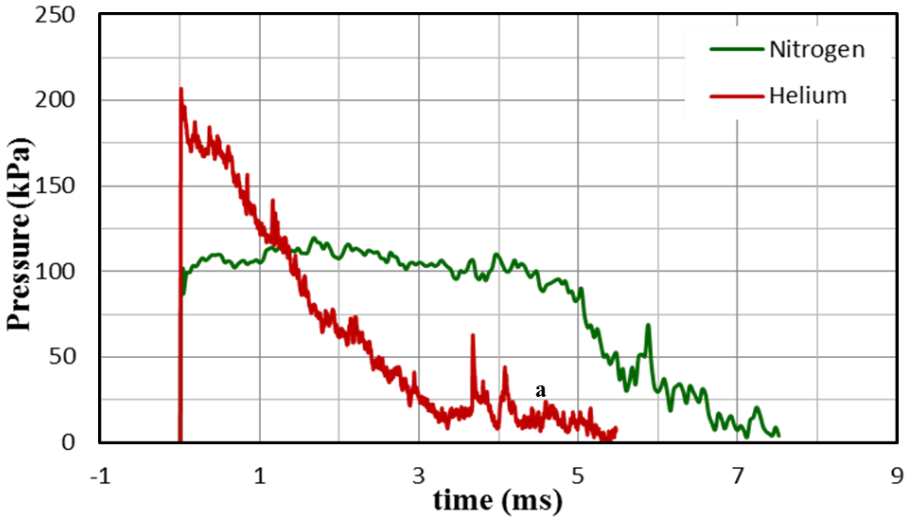

Figure 3.7: comparison of the shock-blast profile for helium and nitrogen with 10 membranes and breech length of 1209.68 mm; clearly, the wave profile corresponding to helium gas is a Friedlander wave and wave profile corresponding to nitrogen is a flat top wave.

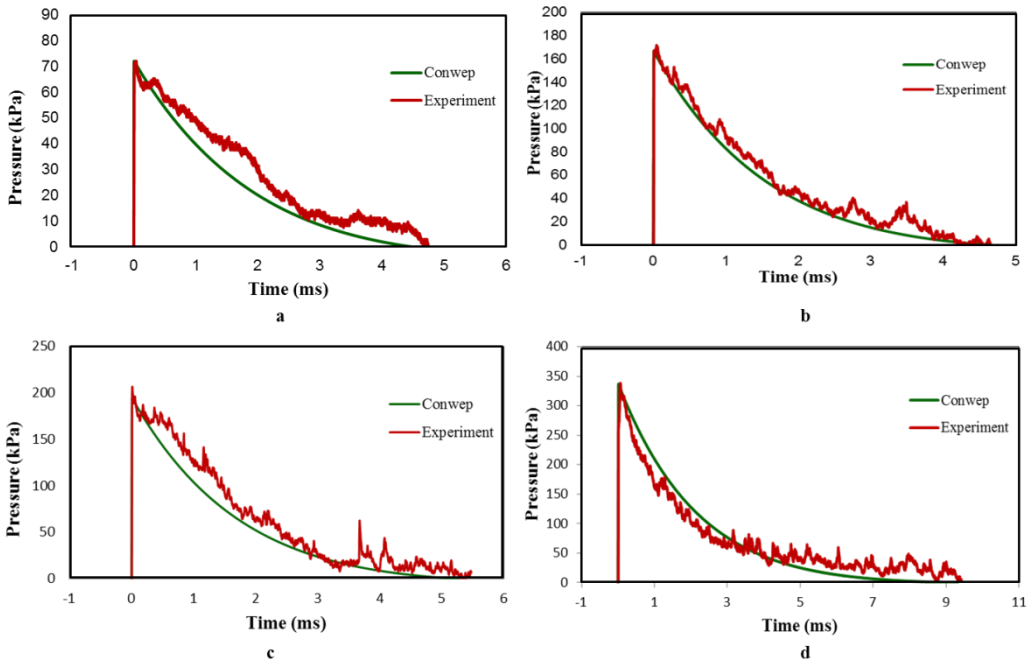

Figure 3.8: Comparison of the shock blast profiles from UNL shock tube device and ConWep simulation software. (a) Comparison between shock blast profile from a 10 membrane, 66.68 mm breech length shot with nitrogen as driver gas and 2.56 kg of TNT at 5.18 m, (b)Comparison between shock blast profile from a 8 membrane, 752.48 mm breech length shot with helium as driver gas and 7.68 kg of TNT at 5 m, (c) Comparison between shock blast profile from a 10 membrane, 1209.68 mm breech length shot with helium as driver gas and 14.08 kg of TNT at 5.7 m, (d) Comparison between shock blast profile from 15 membrane, 1209.68 mm breech length shot with helium as driver gas and 96 kg of TNT at 8.5 m.

In both cases, 10 membranes with a breech length of 1209.68 mm were used. It can be seen that only in the case of nitrogen as driver gas flat top wave is observed, whereas, in the case of helium a pure Friedlander wave is witnessed.

3.3.5. Comparison between field and laboratory profiles

The main object of this work was to establish the shock tube parameters that would be used for generating shock-blast profiles that would mimic field conditions. To validate this hypothesis, we compared the blast profiles of TNT explosive for different strength and range generated from ConWep with those generated from the UNL shock tube device. Figure 3.8 (a) (b) (c) and (d) show the shock-blast pressure profiles, each of these Figures represents a one on one comparison of the incident pressure data from shock tube test section and TNT profiles of different strength and range.

3.4. Discussion

Experiments using animal, cadaver, or test dummies remain the foremost means to investigate the injury biomechanics as well as validate numerical models, and develop personal protective equipment. Currently several researchers use a laboratory compressed gas shock tube to simulate a primary blast insult [18, 22, 98]. However, they do not describe the procedure to control the attributes of a shock blast wave. In this work, we identify the essential parameters of a shock blast wave and describe a methodology to control them by optimizing the parameters of the laboratory gas driven shock tube.

We observed that burst pressure does not vary with respect to increase in the breech length. Furthermore, the membrane rupture is pressure dependent and this critical pressure is not influenced by breech volume, i.e., burst pressure that can be achieved at a minimum breech length L_1 can also be achieved at L_2, L_3 or L_4. Therefore, quantity of membranes used and its thickness is directly proportional to the burst pressure (Figure 3.3). This result corroborates with the findings from the study conducted by Payman and Shepherd, where they used copper as their membrane. They determined that for the same thickness, the burst pressure does not vary more than ± 3%. Similarly, they also determined that membrane thickness has a linear relationship with burst pressure [99].

Controlling BOP and PTD is essential when replicating field blasts. Through the results, it was shown that it is indeed possible in a shock tube to control aforementioned variables by manipulating breech length, burst pressure (membrane thickness), type of gas and test section location (by varying the test section within expansion section). It can be seen that within test section, with an increase in burst pressure both the BOP and the Mach number (strength of shock wave) increases, which implies that both these variables can be increased by increasing the membrane thickness. Similarly, PTD increases with increase in breech length for any given burst pressure. However, at lower breech lengths both BOP and PTD are affected by expansion waves (also known as rarefaction waves) released from the rear end of the breech, which is explained in detail in the next section.

Figure 3.9 shows the x-t wave propagation diagram with shock front, rarefaction head, and tail for two breech lengths. When membranes burst, the driver gas expansion initiates a

family of infinite expansion waves or fan towards the closed end (rear end). Once the expansion head reaches the closed end, they are reflected and travel towards the transition. This reflected wave catches the shock front and since these waves are tensile in nature whereas the shock front is compressive in nature, they start to cancel each other. With each successive expansion wave exiting the breech, the density of the gases reduces and resulting in slowing the successive expansion wave of the fan. This fan of the waves arriving one after the other leads to the nonlinear decay and ultimately shaping the shock blast wave [31]. Once the waveform attains the shape shown in the Figure 2.4 (b) (previous chapter) expansion waves start to erode the BOP and PTD. This was observed in the behavior of waves corresponding to breech length L_1 in the experiment, which is different from the other breech lengths. This is because for L_1, the expansion waves almost instantaneously catch the shock front. For the other lengths, expansion waves catches shock front further down the shock tube (downstream). Therefore, when it arrives at the test section it has already gone through some BOP and PTD reduction. Once the breech length is increased, the time taken by the expansion wave to reach the shock front increases. Consequently, for breech lengths L_2, L_3, and L_4 there is no change in the BOP and PTD at the test section, which implies it is a flattop wave that will become a Friedlander type wave downstream (a pictorial representation is shown in Figure 3.9 by comparing breech lengths C_1 and C_2). Similar to breech length, driver gas also plays a major role in the evolution and interaction of the expansion wave. The expansion wave while traveling towards the closed end of the driver section travels with the ambient sound velocity of that medium. Therefore, for a given breech length and membrane thickness, having helium as a driver gas increases the expansion wave velocity resulting in Friedlander type wave even at an earlier point

than nitrogen gas. Consequently, by varying the length of the breech in conjunction with using the appropriate driver gas we would be able to optimize PTD and BOP.

There is an inherent relationship between SAPs such that optimization of one variable might have a negative effect on the other variables resulting in the formation of a non-optimal shock blast wave. This problem arises depending on: (i) type of driver gas and (ii) test section location. Figure 3.7 shows the comparison of pressure profiles for helium and nitrogen having same membrane thickness (10), breech length (L_4) and measurement location. Although nitrogen due to its low acoustic velocity has a tendency to produce a longer PTD, using a longer breech length results in a flattop wave.

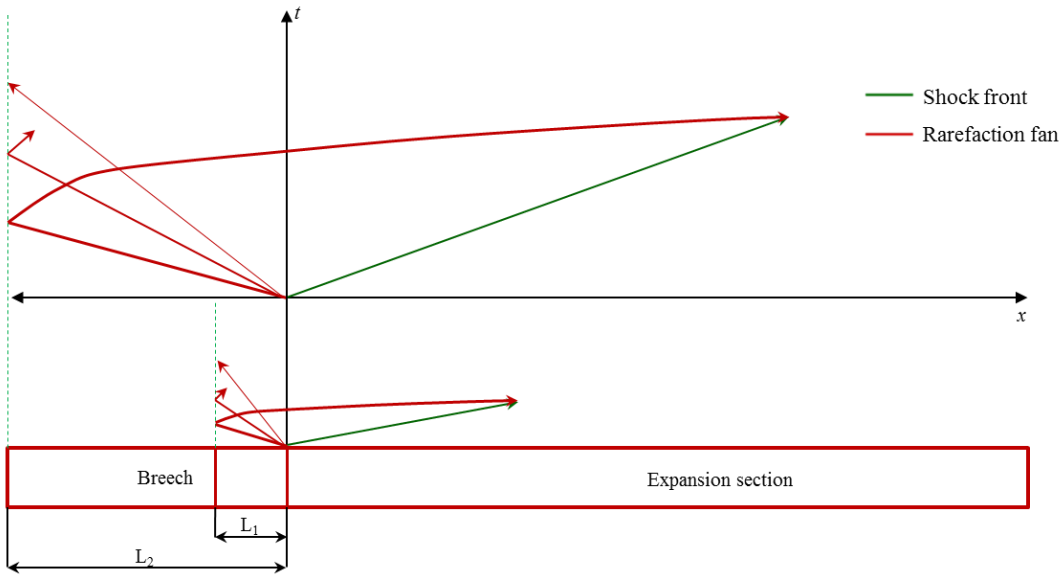

Figure 3.9: Ideal breech length x-t diagram for explosive shock wave replication.

Conversely, helium produces a lower PTD compared to nitrogen but has a sharp decay to the atmospheric pressure. Similar findings are reported in literature, where they compared the wave profiles generated from air (which has acoustic velocity close to nitrogen) and nitrogen with helium. They found that using air and nitrogen as a driver gas produces a flattop wave [18, 100]. One technique used for avoiding a flattop wave when using long breech length is to place the test section downstream of the expansion section, so that the expansion waves would eventually catch up and produces a Friedlander type wave; nevertheless, this method has its own limitation, as explained in the following section.

The evolution of the BOP, PTD, PI at five locations along the length of the expansion section was measured. In a typical free field blast, the BOP decreases rapidly with respect to increase in distance from the blast epicenter [101]. However, BOP in a shock tube does not show a drastic reduction due to its constant cross section. There is a considerable difference between the BOPs for L_1 and all the other breech lengths. As discussed earlier, this difference arises from the interaction of expansion waves that comes from rear end of the breech. This suggests that the expansion waves from the breech for breech length L_1 reaches earlier than all other breech length. With increase in the breech length and burst pressure, distinct points at which the shock blast starts to decay are identified as shown in Figure 3.6 (b) and (c), which implies that downstream to this point shock blast wave has a Friedlander form. Consequently, for longer breech lengths, which tend to produce a flattop wave upstream (e.g. test section), the wave will assume a Friedlander type wave at some point downstream. However, when moving closer to the exit the rarefaction waves from the exit starts to interact with blast wave creating artifacts, which results in inaccurate blast

simulation [31]. As a result, PTD reduces drastically near the exit of the shock tube due to the interaction between shock front and exit expansion waves. This has two consequences: firstly, the PI (energy of blast wave) reduces drastically (Figure 3.6 (g) (h) and (i)). Secondly, since the total energy at the exit is conserved, all the blast energy is converted from supersonic blast wave to subsonic jet wind, which produces erroneous results [37]. The effects of jet wind and specimen placement location along the expansion section for blast simulation using shock tube are illustrated in these references in section 5.4 of chapter 5.

Table 3.1: Explosive capacity of the currently used IEDs and mines in the field. Explosive capacity of these IEDs are given in terms of TNT equivalents in kg.

Threat	Explosive capacity (TNT equivalent in Kg)	Reference
Pipe bomb	2.28	HSD
Suicide bomber	9	
Briefcase bomb	22.70	
AP fragmentation device	0.55	AEP-55
AV blast landmine	6-10	

The discussion above indicated that SAPs can be adjusted to generate a specific shock-blast profile at a specific location (for the placement of animal model). In addition, the

cross-sectional area of the specimen (animal) and specimen holder should be small compared to the entire cross-section of the tube. In all our experiments we have found (through computer simulation and experiments) that if the specimen and holder occupy less than 25% of the tube area, then the reflection from the side walls do not interfere with the profile [22, 96].

Further, it is always beneficial to measure the sidewall pressure just in front of the specimen and possibly one behind to get accurate loading information. A gage too far away upstream or downstream- from the specimen may not yield a reliable loading data, this especially becomes important when developing a nonlinear regression, where incident intracranial pressure is measured as a function of the incident pressure. If possible, one can actually measure the profile using surface pressure gauges glued directly on the animal-and this is the best choice, though surface orientation of the gage and shock direction should be considered.

Table 3.1 shows the IEDs, mine threats currently employed in the field, and their explosive capacity in TNT strength [25, 102]. Using ConWep, we can determine the pressure profiles for TNT explosives within the range of strengths described in Table 3.1. Finally, we compared the shock tube generated wave profile with the incident wave obtained for TNT explosive in ConWep simulation software (Figure 3.8). An important requirement for studying (BINT) is the ability to produce accurate and repeatable blast loading, which can be related to strengths mentioned in table 3.1. Clearly, there is good match in the results,

which indicate that the wave profile generated from our shock tube can be directly related to relevant field conditions.

3.5. Summary

Compressed gas driven shock tubes are used by different research groups to study BINT using animal models. In order to provide field-relevant shock-blast waves and to compare results amongst different groups, it is important to know the actual shock pulse impinging the test objects. Since the pressure time pulse vary significantly for different explosive strength and standoff distance it is important to tailor the shock blast wave parameters for a wide range in controlled and repeatable manner. This study presents how the Shock tube adjustable parameters (SAPs) influence shock-blast wave parameters (SWPs). Further, the need for optimization of SAPs to avoid a flattop wave or expansion waves from the exit, that cause artifacts on the loading profile are explained. Finally, a comparison is made between wave profiles generated from a shock tube and ConWep to show that our shock tube can replicate the exact pressure profiles within a range of practical interest. Some of the key findings of this work are as follows:

- Burst pressure depends only on the membrane thickness and not on the breech length (for practical ranges tested); hence, the blast overpressure (BOP) increases with increase in membrane thickness. At lower breech lengths BOP is affected due to the shock front interaction with expansion waves from the breech.
- Positive time duration (PTD) increases with increase in the breech length; however, higher breech lengths in conjunction with use of nitrogen gas produces a plateau or

a flattop wave. This problem can be solved by either using helium as driver gas or in some cases by shifting the test section downstream of expansion section, (a longer shock tube may be required for avoiding exit end effects).

- When the test section is moved closer to the exit of the shock tube, the rarefaction wave from the exit creates unacceptable artifacts in the wave profile.
- From the comparison of the profiles from ConWep TNT profiles and shock tube profiles it can be concluded that compressed gas shock tube can be used to accurately simulate primary blast injury for blast induced neurotrauma studies.

In this chapter, a comparative study between blast profiles generated from shock tube (without specimen) and conventional explosive (TNT profiles from ConWep software) were made. In the following chapter, comparison of the reflected pressures (pressure actually felt by the subject) between shock tube and field experiments is presented.

CHAPTER 4: VALIDATION OF SHOCK TUBE THROUGH FIELD TESTING

4.1. Introduction

One of the main goals of the current research is to prove that compressed gas shock tube can accurately model the field blast conditions pertaining to primary blast injury. The approach taken to study this problem was to systematically compare the incident pressures recorded in the shock tube to the field incident profiles of TNT, which were obtained from the ConWep simulation software. Secondly, a comparative analysis of the reflected pressures between field blast results with the results from the shock tube using a surrogate head (UNL RED head) was done, which is presented in this chapter. Furthermore, to study the effect of placing test section outside the shock tube, experiments were done outside and compared with the results from the experiment performed inside the shock tube. Section 4.2 of this chapter gives the methods used for this study including the details on the shock tube testing, field-testing, instrumentation used, and the statistical analysis performed for the comparative study. Section 4.3, the results from the study is presented along with the discussion of the results. Finally, section 4.4 shows the summary of the findings from this study.

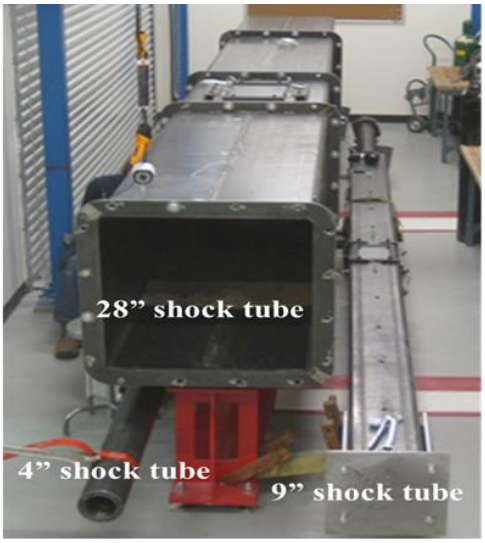

(a)

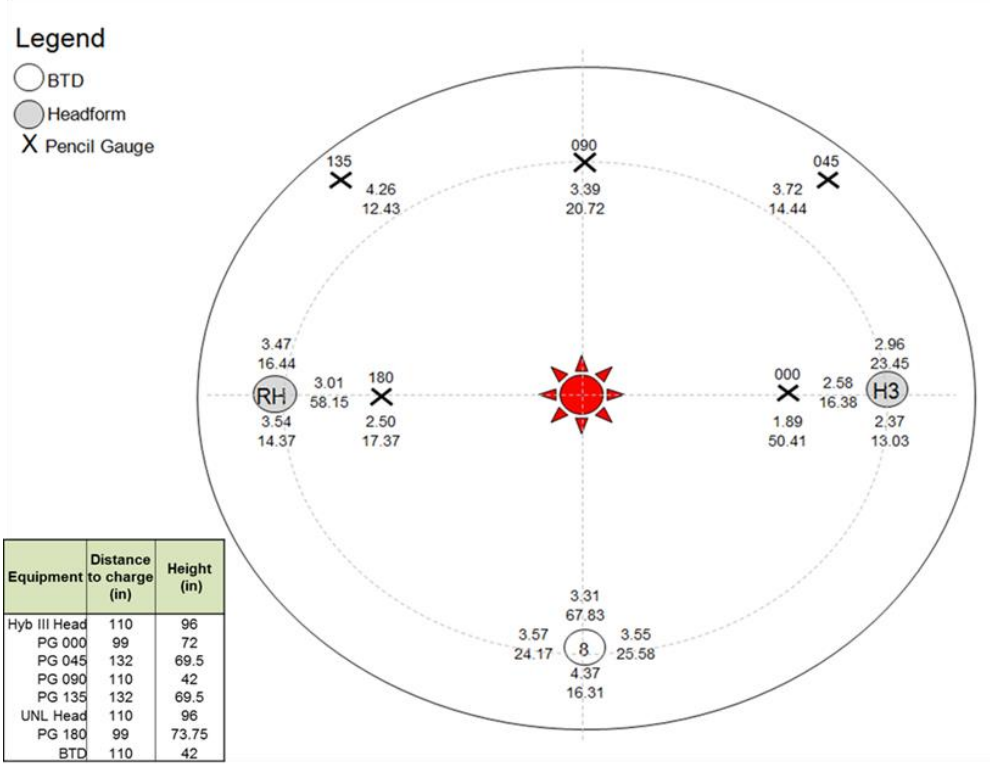

Equipment	Distance to charge (in)	Height (in)
Hyb III Head	110	96
PG 000	99	72
PG 045	132	69.5
PG 090	110	42
PG 135	132	69.5
UNL Head	110	96
PG 180	99	73.75
BTD	110	42

(b)

Figure 4.1: (a) 28 in. and 9 in. shock tube, (b) Schematic layout of the field explosion test.

4.2. Method

4.2.1. Shock tubes

Figure 4.1 (a) shows the 28 in. and 9 in. shock tube. When the breech is pressurized, membranes rupture expanding the high-pressure gas to expand into the expansion section driving a shock wave into the test section.

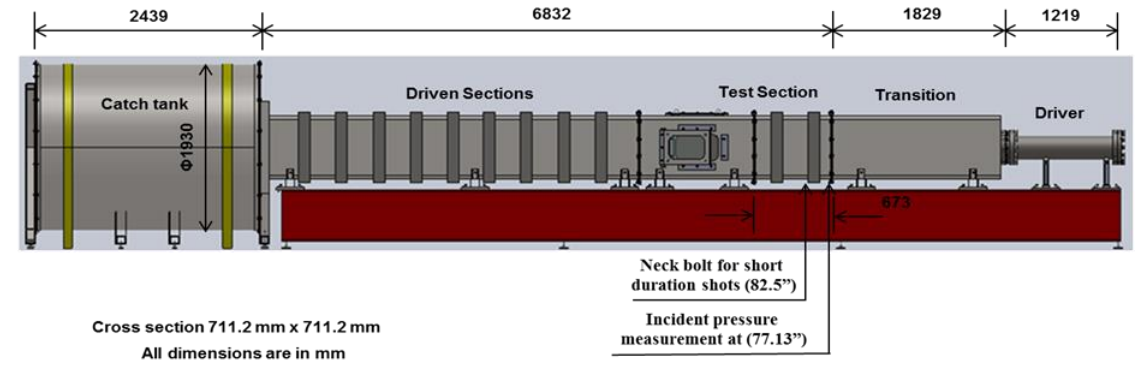

(a)

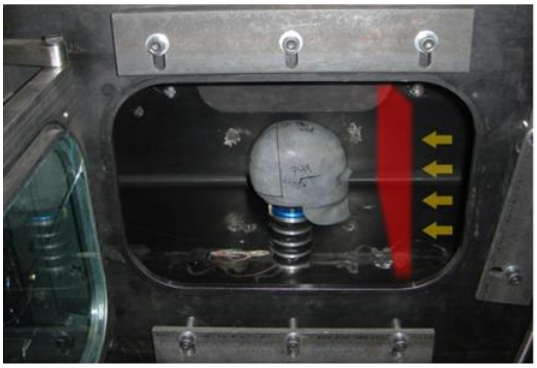

(b)

(c)

Figure 4.2: (a) Experimental setup (a) schematic of the 711 x 711 mm shock tube system, (b) realistic explosive surrogate (RED) head with hybrid III neck inside 28 in. shock tube,

(c) head with hybrid III neck outside 9 in. shock tube, the RED head is located at 11.81 in. (302.51 mm) from the exit.

For details of how shock wave is generated inside the shock tube and what happens near the exit, please refer chapter 4 and section 5.4 respectively. Figure 4.2 (a) and (b) show the experimental setup for the shock tube testing in the 28 in. and 9 in. shock tube respectively. In the 28 in. shock tube the surrogate head was placed 82.5 in. downstream from the breech, which is slightly ahead of the test section. In the case of the 9 in. shock tube the surrogate head was placed 11.81 in. (302.51 mm) from the exit of the shock tube (to test the effect of placing specimen outside). The idea behind this is to study, which location of the shock tube matches well with the results of the surrogate exposed to the field condition.

4.2.2. Free-field (FF) experiments

RED head was subjected to blasts from live-fire explosives. Dummy was placed at 110 in. (2794 mm) from the cylindrical C4 charge and 96 in. (2438 mm) from the ground. Figure 4.1 (b) shows the location of the dummy with the location of the explosive charge and the pencil gauges to measure incident pressure. Dummy was oriented with its anterior part facing the epicenter of the blast.

4.2.3. Surrogate and instrumentation

The surrogate head consists of a polyurethane skull with an opening for the brain and cerebrospinal fluid. It is attached to the neck through the base plate. In this case, intracranial contents were not included.

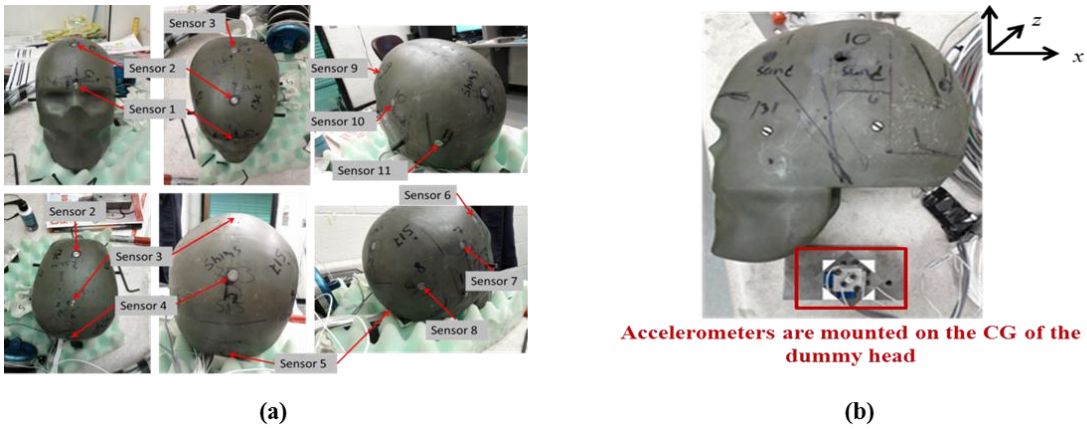

Figure 4.3: (a) Location of the pressure sensors, (b) Location of the acceleration sensor with positive accelerations measured along x and z axis.

The surrogate was instrumented with 11 shock-ready PCB pressure sensors (102B06) and two linear accelerometers (Endevco 7270a) mounted to a tri-axial block located at the center of gravity of the 4.5 kg specimen. Furthermore, helmet was also used in a separate group and comparisons between field and shock tube with and without helmets were made.

Figure 4.3 (a) and (b) show the locations of the pressure sensors on the RED head and the placement of the linear accelerometers respectively. Out of the eleven sensors five are located along the mid-sagittal plane and the other six are located on the side of the head,

three on each side. All pressure sensors utilized in experiments are calibrated under shock loading conditions using a separate 101 mm (4 in.) diameter shock tube (Figure 4.1 (a)) using a flat-topped wave. Accurate calibrations are achieved by generating precisely controlled shock wave velocities and invoking the Rankine–Hugoniot jump conditions to relate shock wave velocities to shock wave overpressures. In the case of accelerometers, factory calibrations were used directly in data interpretation.

4.2.4. Incident pressure

Figure 4.4 shows the incident overpressures recorded in the field as well as in both shock tubes.

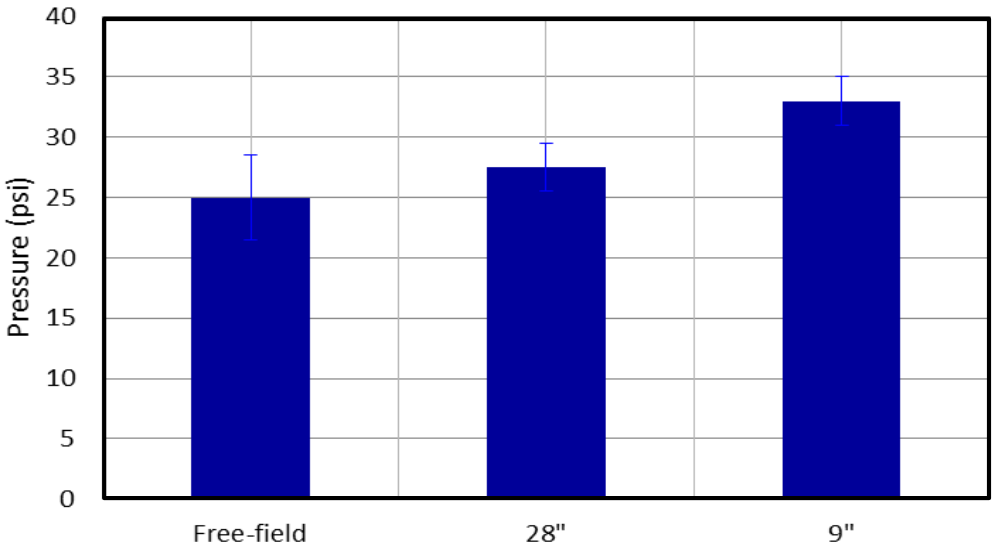

Figure 4.4: Comparison of the average incident overpressure between free field and shock tube shots (1 psi = 6.894 kPa).

Incident pressure varied between 25 to 34 psi (172 to 235 kPa), with the lowest being recorded in the field experiments. The variation of overpressure within the free-field shots is also high (about 9 psi) compared to shock tube (about 3 psi), as demonstrated by the high standard deviation. Furthermore, the peak pressure is low in the case of the field tests, which would manifest in the comparisons of peaks between shock tube and field tests.

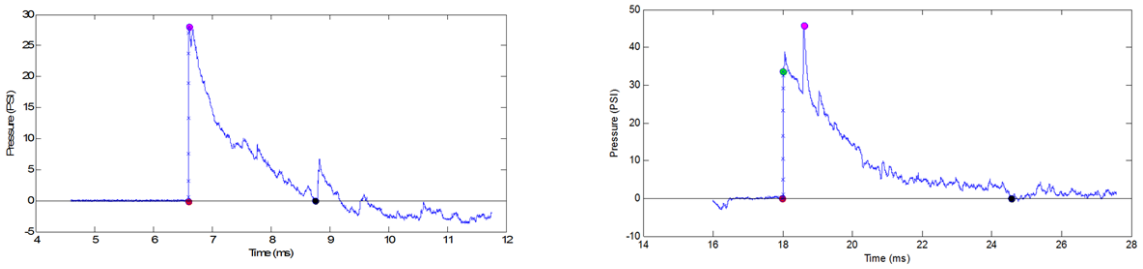

Figure 4.5: (a) Incident pressures for a typical 28 in. shot measured 1960 mm (77.13 in.) from the membranes, (b) Incident pressures for a typical 9 in. shot measured 38 mm (1.5 in.) from the exit of the shock tube, here the second peak marked with pink dot is a sensor artifact arising from sensor vibration (1 psi = 6.894 kPa).

However, this difference should not affect shape of the profile, which is mainly governed by the blast wave interaction with surrogate. The measurement of the incident pressure for the 9 in. shots was taken 1.5 in. from the open end. Figure 4.5 (a) and (b) show the incident pressures for 28 in. shock tube and 9 in. shock tube shot respectively. From the Figure, it can be seen that the overpressure as well as positive time duration are higher in the case of the 9 in. shots as opposed to the 28 in. shots. This relatively long duration is the result of

the amplification of incident wave due its reflection from the anterior region the RED head at the exit of the shock tube.

4.2.5. Statistical analysis

The main objective of the study is to compare the field experiment data and with shock tube data and analysis the similarities and differences. For this purpose, an ANOVA test was performed between groups. Differences were considered significant at $p < 0.05$ (if $p > 0.05$, there is no significant difference between the groups). Furthermore, a power analysis was also performed for results with $p < 0.05$ to determine whether there are any power problems. Here the probability of the power type II error was calculated, which represents the false negative.

4.3. Results and discussion

4.3.1. Comparison between free-field blast and 28 in. short duration results

4.3.1.1. Front bare head facing

Figure 4.6 (a) and (b) show the comparison between peak overpressure and linear acceleration between the free-field tests and the tests performed in the 28 in. shock tube. In terms of magnitude, there is no significant difference between sensor 1, 4 and 11; however, while performing a power analysis on these comparisons it was determined that there is a 62%, 68% and 82% chance of type II error respectively. There is a significant difference in the magnitude for all the other cases. Among them sensor 2 has the maximum

average difference (17.29 psi) and sensor 7 has the minimum difference (4.87 psi). Except for the sensor location 1 and 11, the overpressure recorded in all the other sensors are higher in the case of shock tube than in the free field (statistical analysis for all sensor locations is given in appendix A (I)).

Figure 4.7 shows pressure profiles for the bare head in free field and shock tube. Looking at traces from these sensors there are not many differences in their overall shape; positive time regions look as though they are also in good agreement. Traces with the most apparent differences are from sensor 10 and even these have similar positive time regions.

Figure 4.6 (b) shows the peak minimum and maximum acceleration comparisons between shock tube and free field data. From the statistical analysis, it can be seen that there no significant difference in the maximum positive acceleration recorded in sensors 5 and 6 between free field and shock tube. However, power analysis for sensor 5 and 6 proved that the probability of type II error, i.e., miss of an effect is 57% and 92 % respectively.

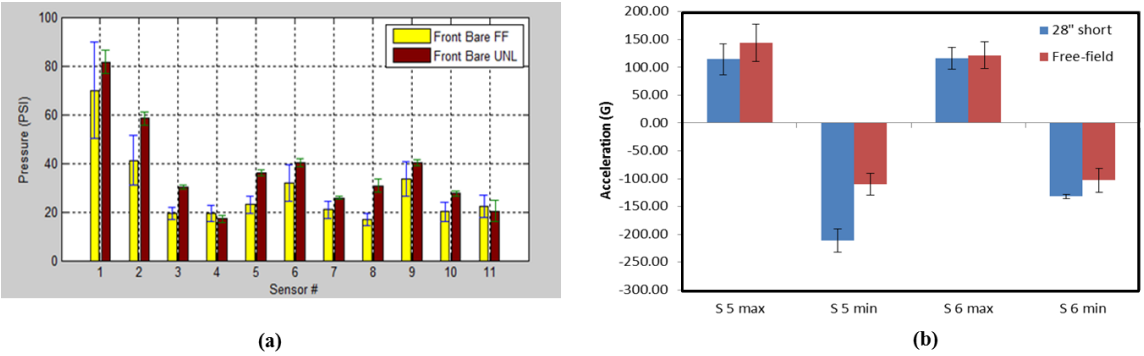

(a) (b)

Figure 4.6: comparisons of (a) overpressure, (b) Minimum and maximum linear acceleration for a front facing bare head in free field and shock tube, (1 psi = 6.894 kPa).

There is a significant difference in the negative acceleration in sensor 5 and 6. Figure 4.8 (a) and (b) show the acceleration profile. In this case, the maximum and minimum in the middle of the trace are not artifacts of the sensor; it is possibly due to the existence of a force being built upon the geometry of the head.

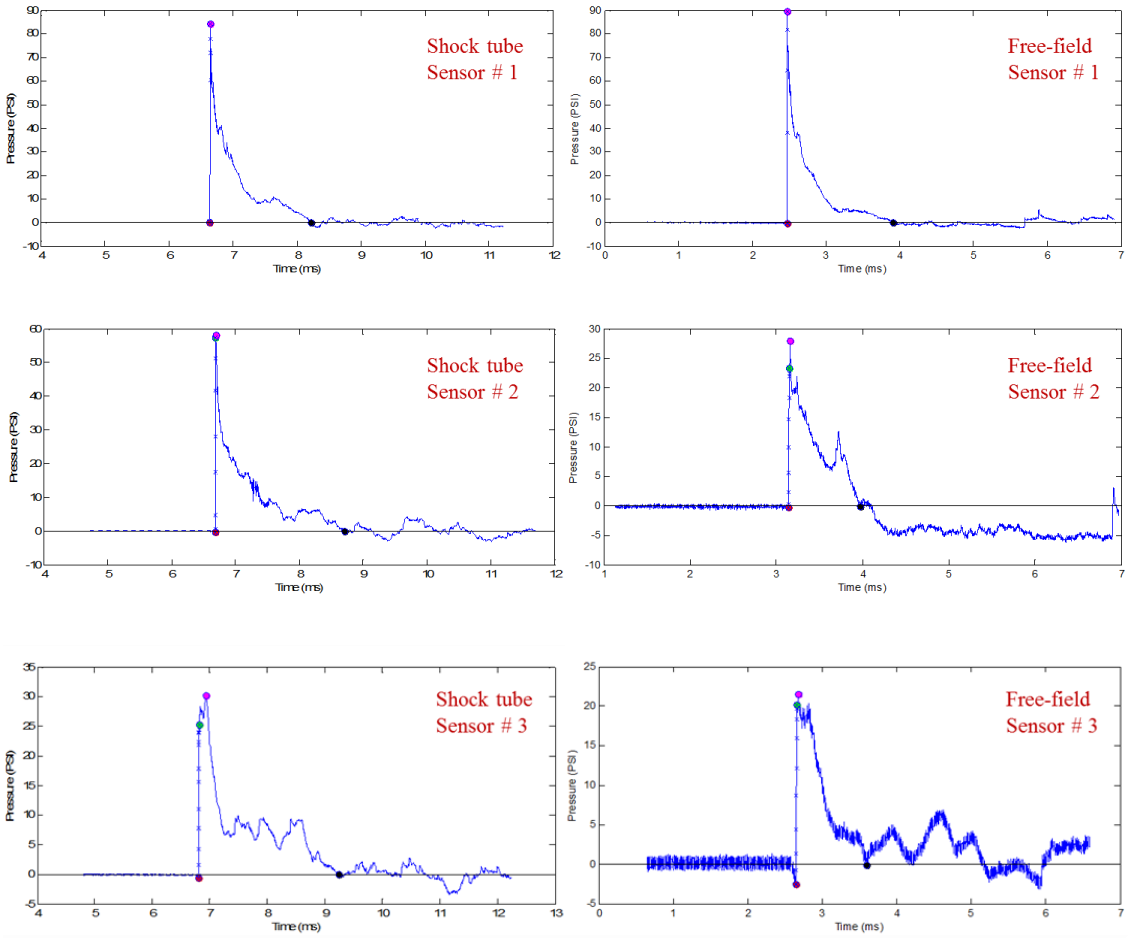

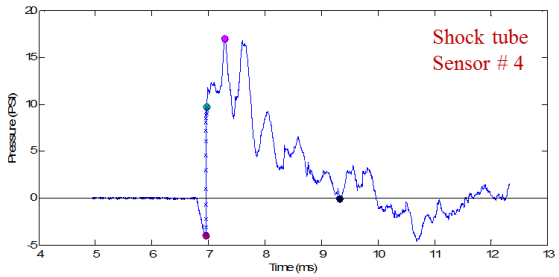
Shock tube
Sensor # 4
Pressure (PSI)
Time (ms)

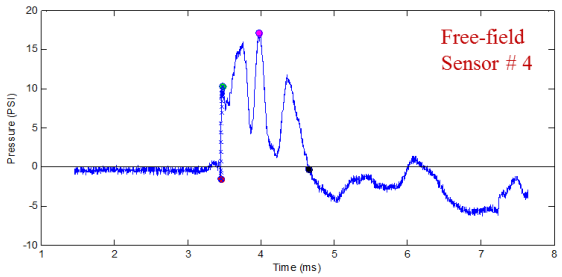
Free-field
Sensor # 4
Pressure (PSI)
Time (ms)

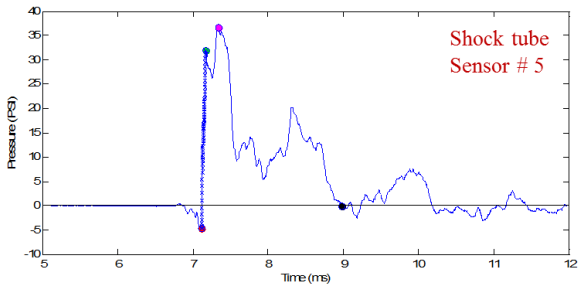
Shock tube
Sensor # 5
Pressure (PSI)
Time (ms)

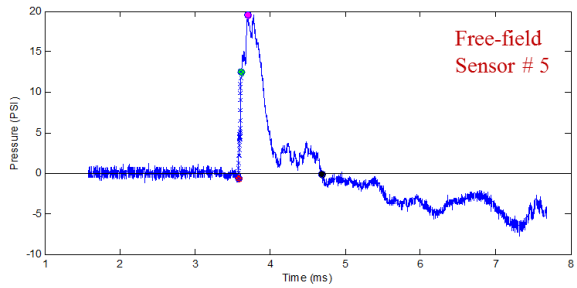
Free-field
Sensor # 5
Pressure (PSI)
Time (ms)

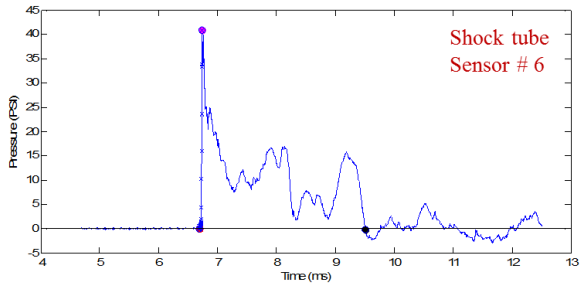
Shock tube
Sensor # 6
Pressure (PSI)
Time (ms)

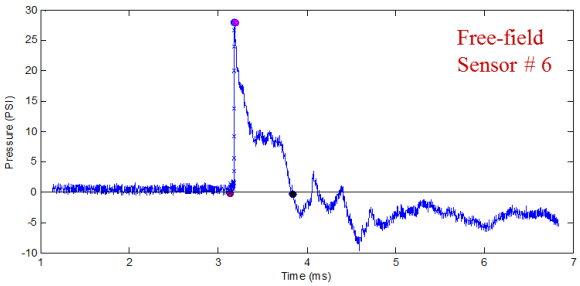
Free-field
Sensor # 6
Pressure (PSI)
Time (ms)

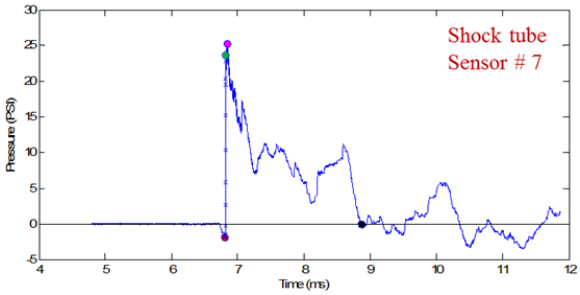
Shock tube
Sensor # 7
Pressure (PSI)
Time (ms)

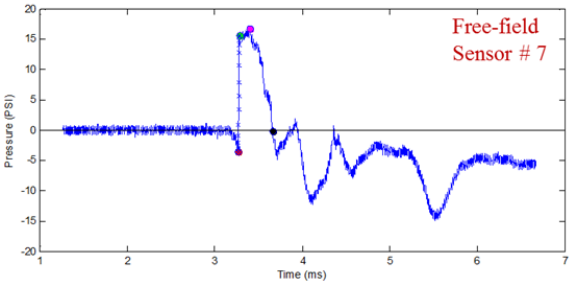
Free-field
Sensor # 7
Pressure (PSI)
Time (ms)

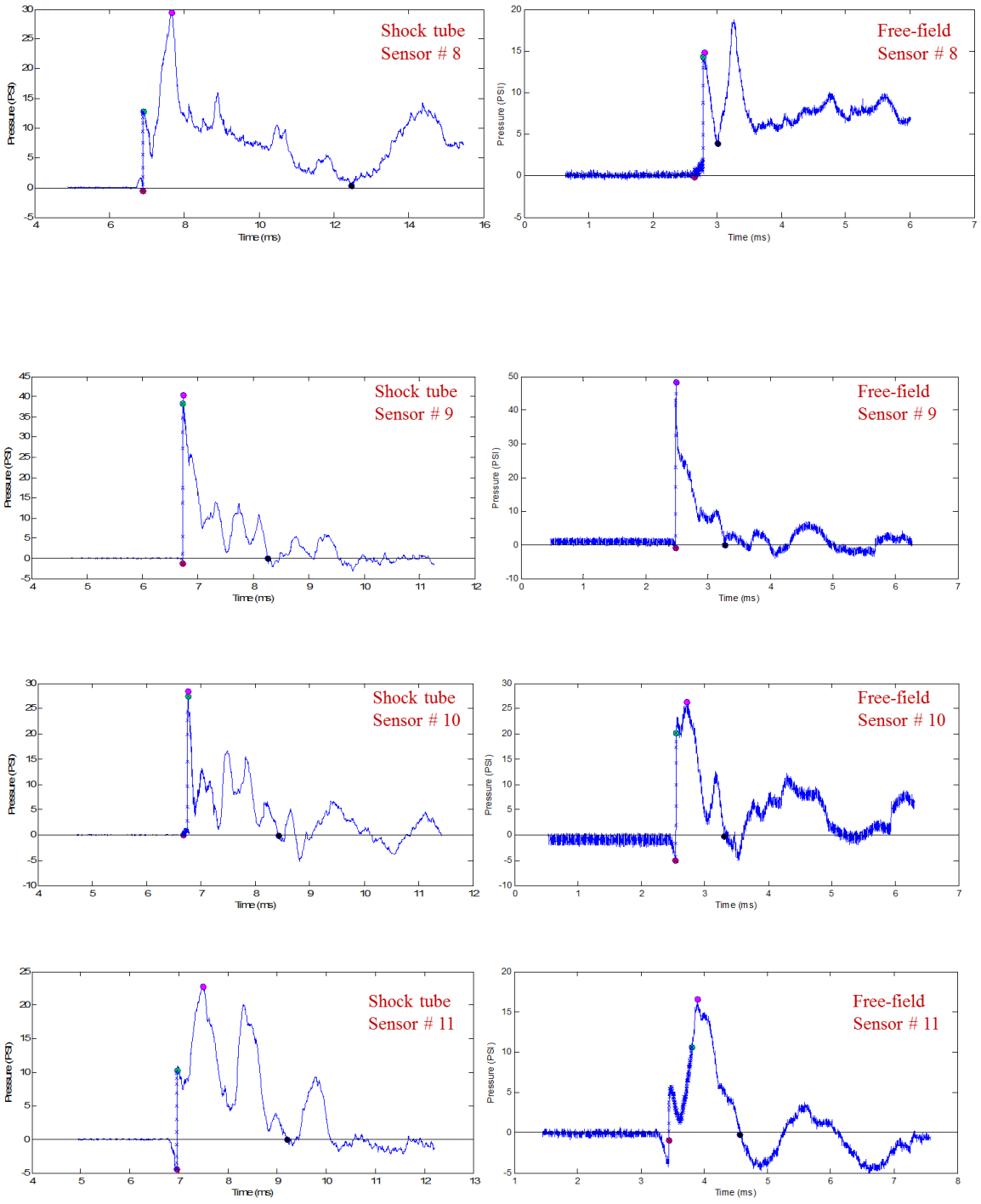

Figure 4.7: Comparisons between pressure profiles for bare head in free field and 28 in. short duration shot, (1 psi = 6.894 kPa).

In both the free field and in the 28 in. shock tube for sensor 5, profiles exhibit a sharp rise soon after the time of arrival. Also, if one ignores the first rise in the profiles, the time difference between the min and max peaks looks like it is in good agreement with the min value happening ~1.5 ms before the max value (Figure 4.8).

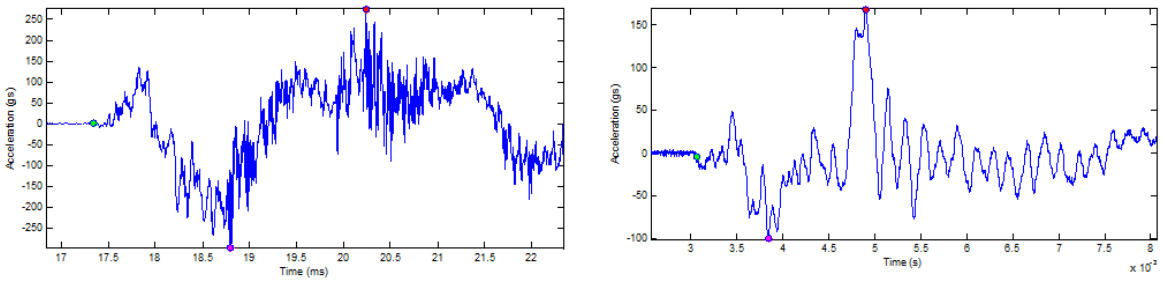

(a) **(b)**

Figure 4.8: Comparison of acceleration profile for sensor # 5 of bare head, (a) shock tube, (b) field experiment, in this case we can clearly see the existence of maximum value well past the peak acceleration corresponding to the traverse of the shock front (1).

4.3.1.2. Front helmeted head

Figure 4.9 (a) shows the comparison of peak pressure between 28 in. short and free field when the head is helmeted. It appears that some profiles from the free field seem to be attenuated with respect to the 28 in. shock tube tests. An exception is the response of sensor 1 and 11, in which the free field data looks larger than the UNL shock tube data. From the statistical analysis, it was determined that there is no significant difference in sensors 3, 8 and 10. However, further power analysis showed that there is 88%, 89% and 68% chance

of type II error in those results respectively. Among the other sensors, sensor 5 has the maximum difference of 15.88 psi and minimum difference of 4.21 in sensor 4 (statistical analysis for all sensor locations is given in appendix A (II)).

An analysis of the free field shock front planarity may be necessary to ensure the planarity of the shock front. In the shock tube, planarity has been measured and validated. Some of the pressure values seem high in the free field helmeted tests when compared to the UNL shock tube tests. This may be due to the potential curvature of the free field shock wave pushing up and underneath the helmet brim, as indicated in the Figure 4.10.

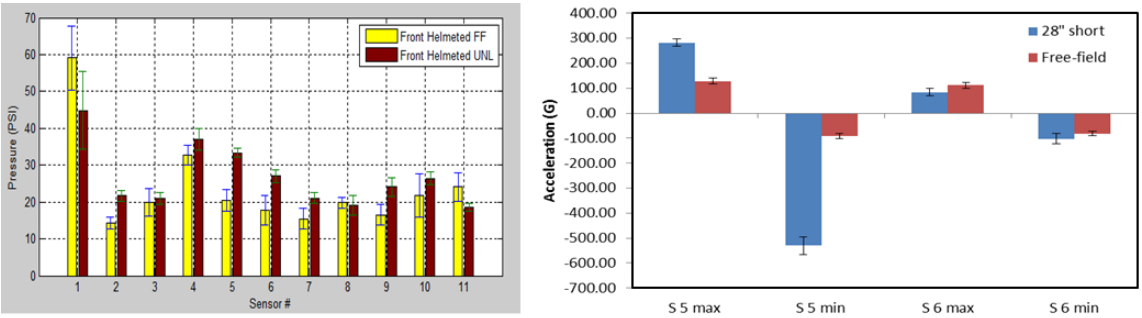

(a) **(b)**

Figure 4.9: Comparisons of (a) maximum overpressure, (b) linear acceleration for a front facing helmeted head in free field and shock tube. All the maximum values of the acceleration were obtained in the first 50 ms, there is a huge difference in the negative acceleration of sensor 5 when compared with the field, (1 psi = 6.894 kPa).

This hypothesis may be further substantiated when looking at the traces from sensor 1 in the free field and in the 28 in. shock tube. In the free field traces of sensor 1, there is a clean

rise often followed by a brief secondary peak, whereas in the 28 in. tube the data at the peak of the trace from sensor 1 are highly oscillatory indicating that turbulence may be occurring at this localized area. Turbulence would be expected if the planarity of the shock front had been broken before it interacted with sensor 1 and a smooth rise would be expected if the planarity of the shock front had not been broken before it interacted with sensor 1 (Figure 4.11). There are slight variations in the profiles; however, this variation may be due to several experimental factors like: (a) position of the helmet during the test, (b) variance in the shock front helmet interaction and (c) variance in the free field-testing.

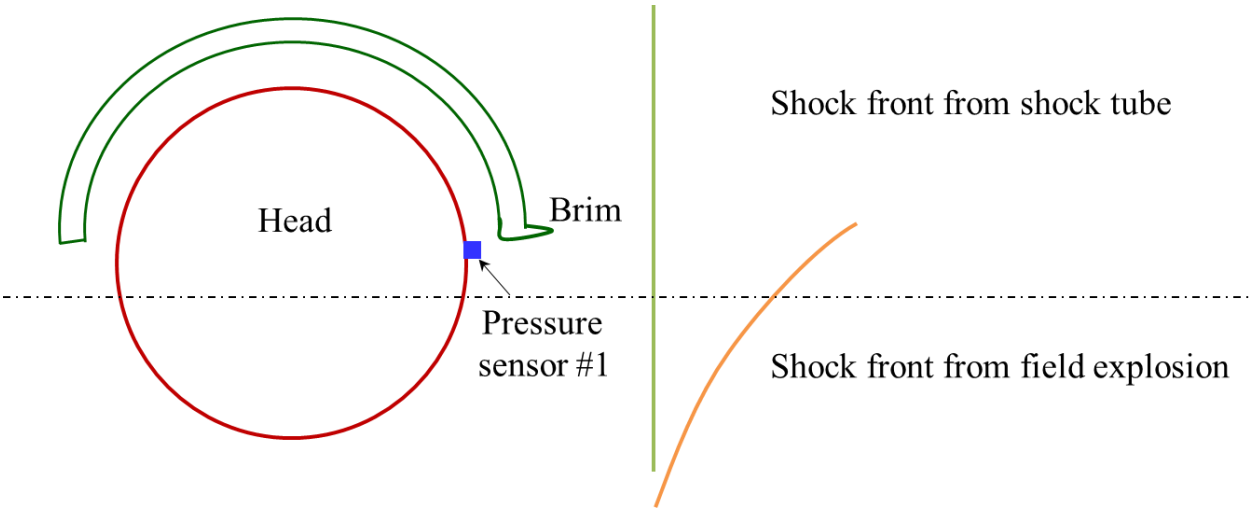

Figure 4.10: Diagram of head form and potential shockwave interactions. Blue square indicates location of sensor 1 with respect to the brim of the helmet. The shock fronts drawn here are exaggerated for the sake of explanation and they are not drawn to the scale.

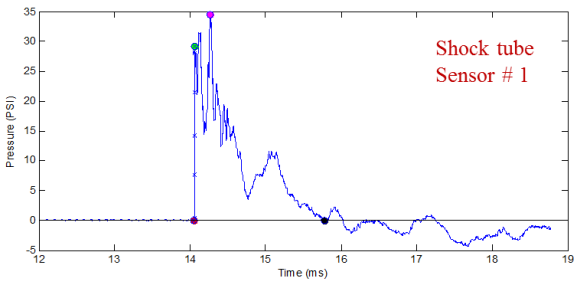
Shock tube
Sensor # 1
Pressure (PSI)
Time (ms)

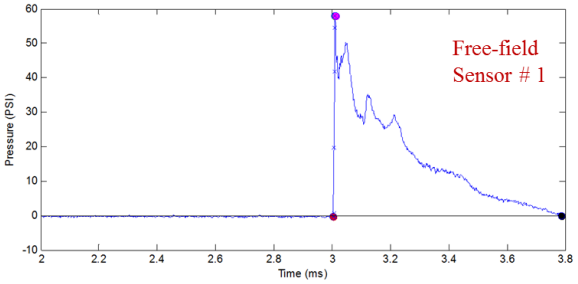
Free-field
Sensor # 1
Pressure (PSI)
Time (ms)

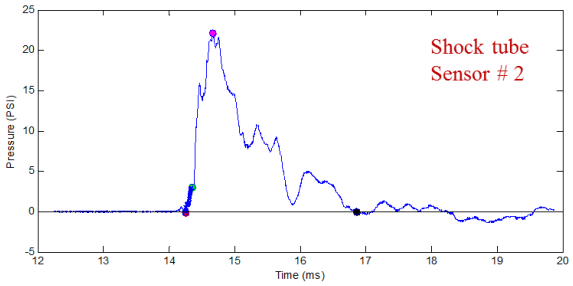
Shock tube
Sensor # 2
Pressure (PSI)
Time (ms)

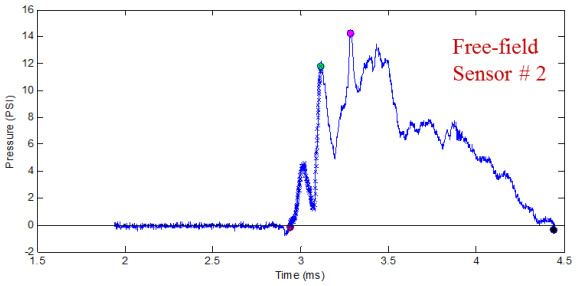
Free-field
Sensor # 2
Pressure (PSI)
Time (ms)

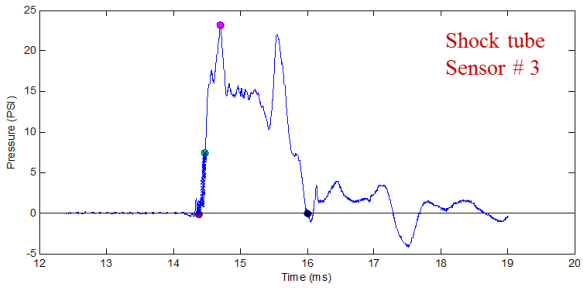
Shock tube
Sensor # 3
Pressure (PSI)
Time (ms)

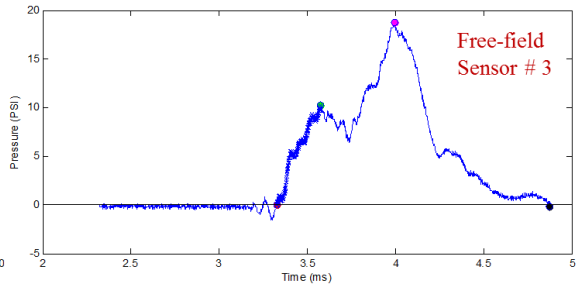
Free-field
Sensor # 3
Pressure (PSI)
Time (ms)

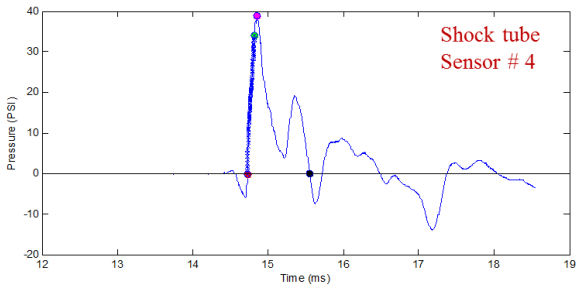
Shock tube
Sensor # 4
Pressure (PSI)
Time (ms)

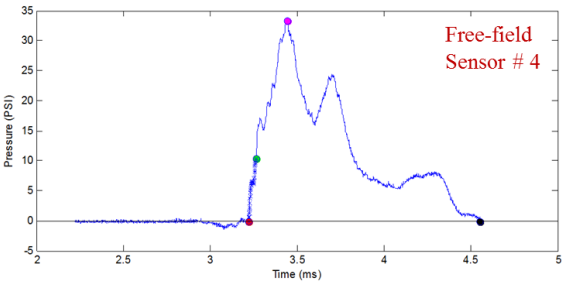
Free-field
Sensor # 4
Pressure (PSI)
Time (ms)

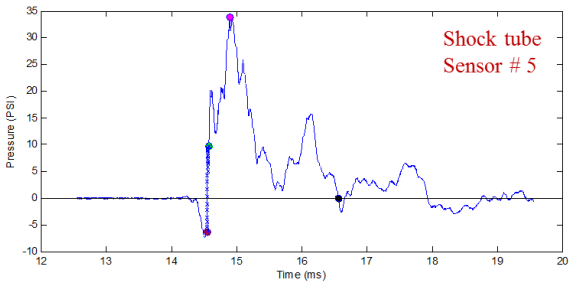
Shock tube
Sensor # 5
Pressure (PSI)
Time (ms)

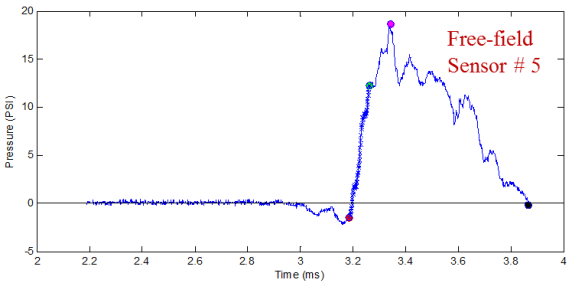
Free-field
Sensor # 5
Pressure (PSI)
Time (ms)

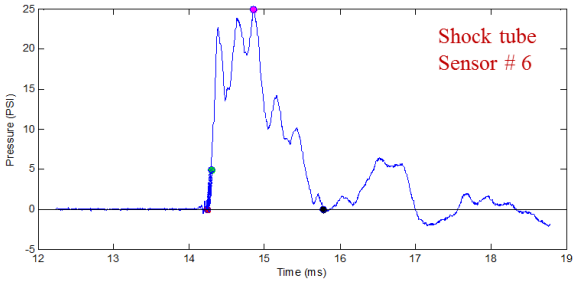
Shock tube
Sensor # 6
Pressure (PSI)
Time (ms)

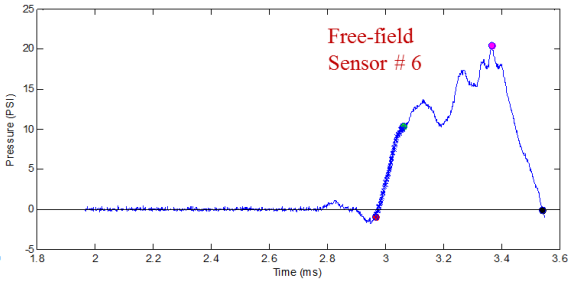
Free-field
Sensor # 6
Pressure (PSI)
Time (ms)

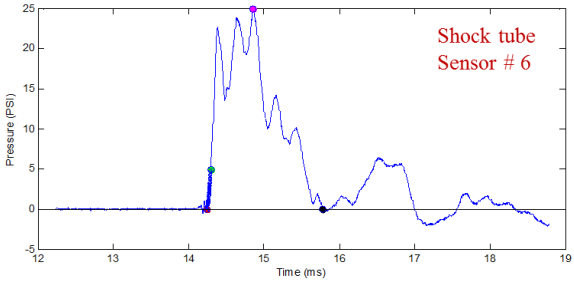
Shock tube
Sensor # 6
Pressure (PSI)
Time (ms)

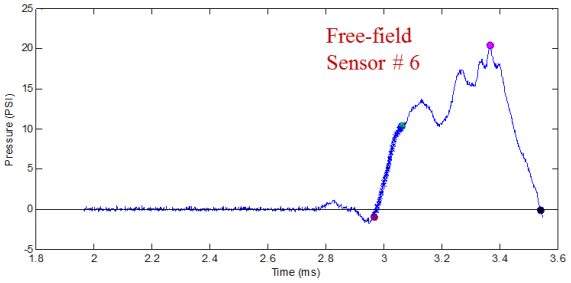
Free-field
Sensor # 6
Pressure (PSI)
Time (ms)

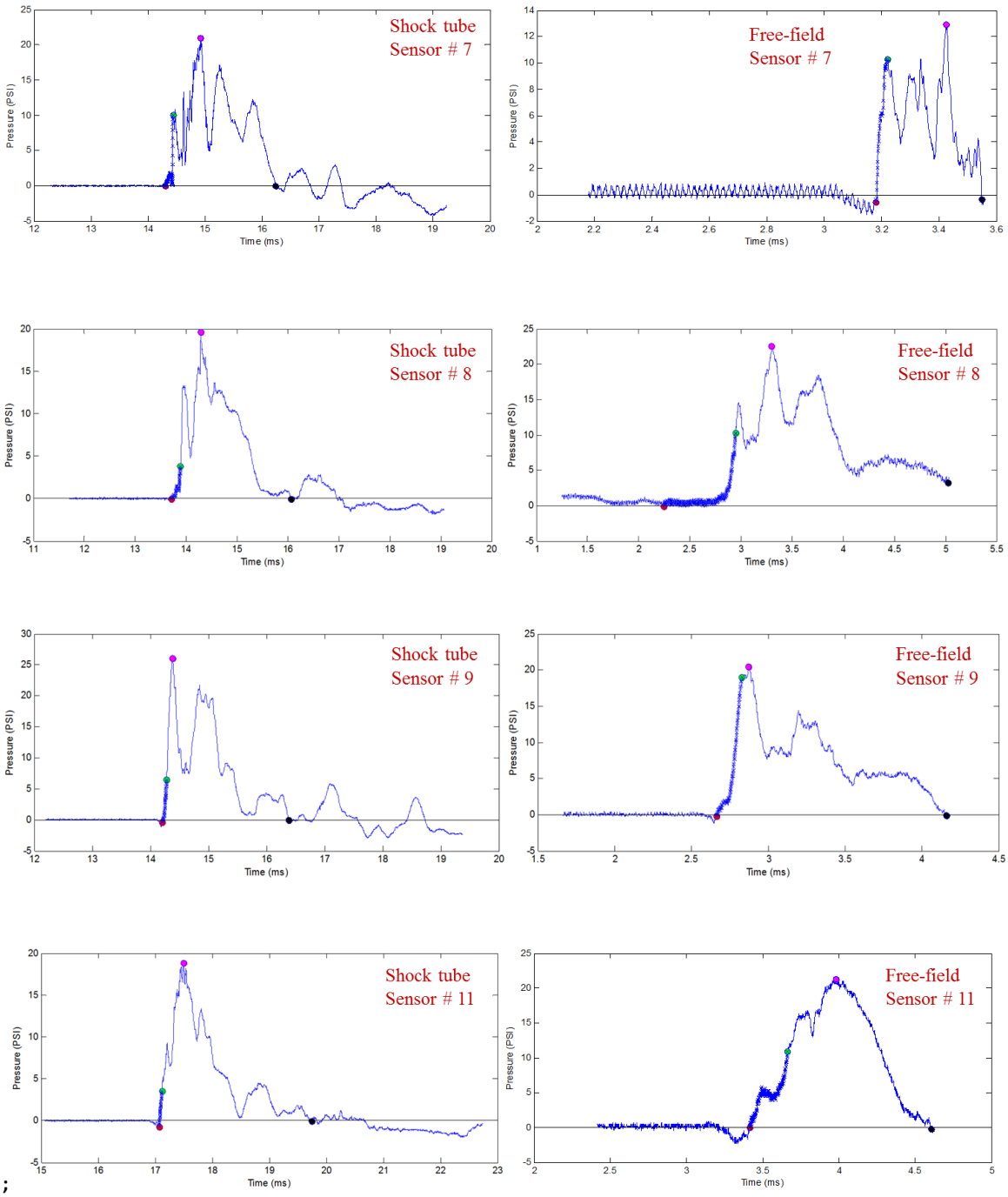

;

Figure 4.11: Comparison of pressure profiles between free field and shock tube tests for a helmeted head for selected sensors. From the profile for sensor 1 it can be seen that the beginning of the trace in the free field conditions is non-oscillatory indicating that the

planarity of the shock front did not break from interactions with the brim of the helmet, while the trace from the shock tube is oscillatory as a result of the planarity of the shock front being broken up from interactions with the brim of the helmet before interacting with sensor 1, (1 psi = 6.894 kPa).

Figure 4.9 (b) shows the linear acceleration of the helmeted head. There is a significant difference in the acceleration in both sensors 5 and 6 with highest being the shock tube in the negative direction of sensor 5. This is because of the buildup of the pressure in the head helmet subspace, which pushes the head backward through the chinstrap. The high negative acceleration is due to the spring back caused by the HIII neck used in the experimental setup. Furthermore, higher acceleration when shock front traverses in the shock is also due to the higher Mach number generated in the shock tube tests as opposed to the field tests. Figure 4.12 shows a statistical comparison of free field and shock tube data based on maximum and minimum values garnered from the first 5ms (not just due to the traverse of the shock front). Linear accelerometer comparisons for the free field Vs. 28 in. short duration bare acceleration data, the maximum and minimum values were usually seen past the first peak, i.e., the acceleration values corresponding to the traverse of the shock front is not be the maximum acceleration.

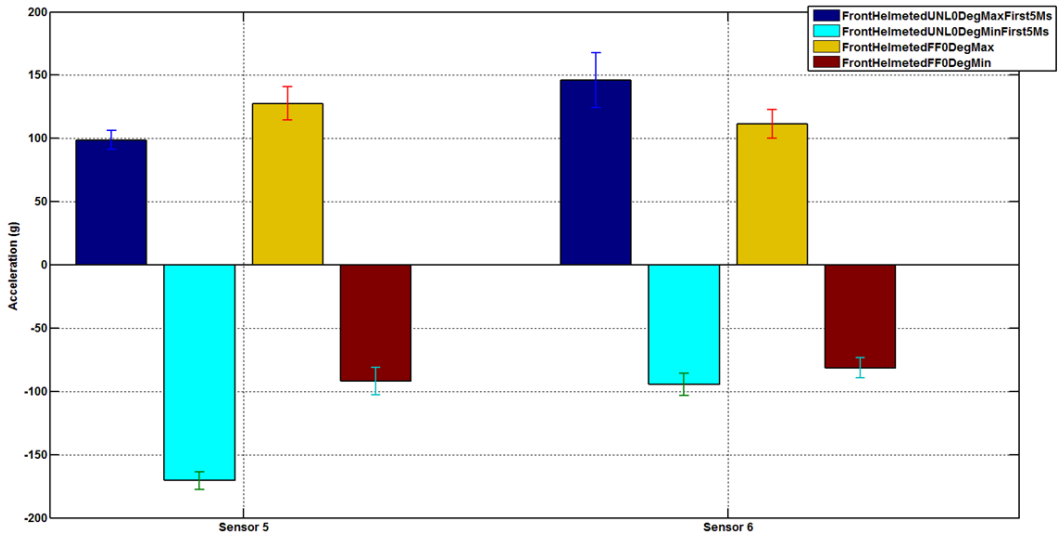

Figure 4.12: Comparisons between accelerometers 5 and 6 for helmeted front facing orientation in both the free field and UNL 28 in. shock tube short duration tests; derived from the beginning of the trace (5ms from the time of arrival). 5ms was chosen to see how comparable the accelerations are during the traverse of the shock front before buildup of energy in the anterior of the head. Gathering the peak minimum and maximum values from the first 5ms, the shock tube data better approximates the free field data; still, discrepancies may exist between different data sets.

4.3.2. Comparison between inside (short duration) and outside (D1) the shock tubes

The purpose of this study is to compare the varying flow condition while doing experiment at test section and the exit of the shock tube.

4.3.2.1. Front bare head

Here we compare the overpressures and linear acceleration for: (1) 28 in. short duration (2-3 ms) and (2) 9 in. shock tube at a distance D1 (11.8 in. from the exit). From Figure 4.13 (a), it can be seen that sensors 1, 2, 6 and 9 record a higher pressure in 9 in. D1 than in 28 in. short duration shot.

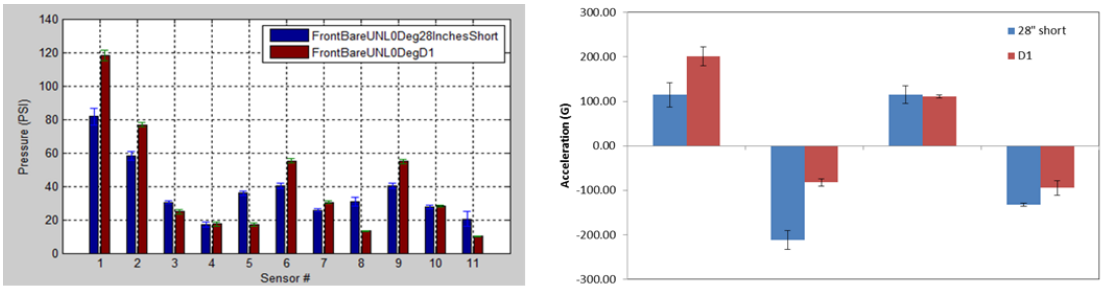

(a) **(b)**

Figure 4.13: comparisons of (a) overpressure, (b) linear acceleration for a front facing bare head inside a 28 in. shock tube and outside at distance D1 in 9 in. shock tube, (1 psi = 6.894 kPa).

Further statistical analysis proved that there is a significant difference in all the sensors but 4 and 10; however, power analysis showed that there is a chance of 93% and 81% respectively for those sensor comparisons to be a type II error. In sensors 3, 4, 5, 7, 8, 10, 11 the overpressure is either equal or the overpressure is higher for the 28 in. short duration shot. This is due to varying flow dynamics near the exit of the tube, around the RED head when placed outside, which is illustrated in the following Figure 4.14.

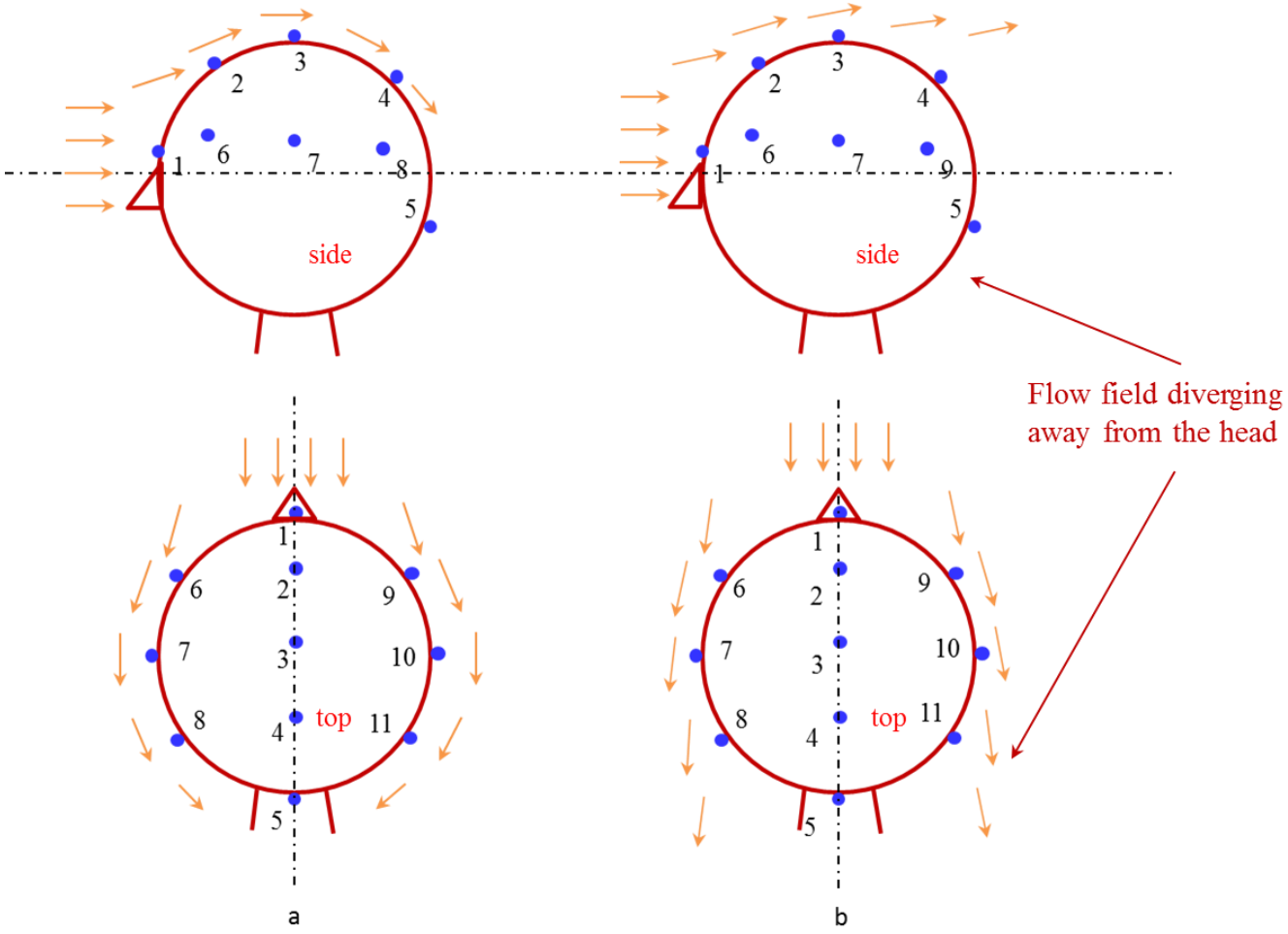

Figure 4.14: Flow dynamics around the head form (a) inside the shock tube, (b) outside outside the shock tube.

As described above, when inside (Figure 4.14 (a)), the shock front after interacting with the anterior of the head diffracts and converges around the head form. However, when outside, following the interaction with the head, the flow field expands outwards due to the pressure gradient (Figure 4.14 (b)). This phenomenon is responsible for the reduction in the overpressure in sensors 3, 4, 5, 7, 8, 10, 11. When looking at the profiles it is evident

that there is a significant reduction in the positive time duration when the head form is placed outside as opposed to inside (Figure 4.15).

This behavior of the shock front losing its planarity and diverge from the exit of the shock tube is also seen through Figure 5.7 of chapter 5, where the complex nature of the shock front exiting the tube is described. Figure 4.13 (b) shows the comparison of linear acceleration for short duration 28 in. and 9 in. D1 shots with the RED head (bare) facing the shock front at 0^{o}. From the statistical analysis done on sensor 5 and 6, it can be seen that there is a significant difference in both positive and negative accelerations of sensor 5 and maximum negative of sensor 6. It is interesting to notice that positive is more in 9 in. D1 shot whereas negative is more in the 28 in. shot. This might be due to the exiting jet wind in the 9 in. D1 shot slowing down the reaction (spring back) of the RED head. In sensor 6 maximum positive does not have a significant difference; but, power analysis shows that there is 93% chance of type II error in that comparison.

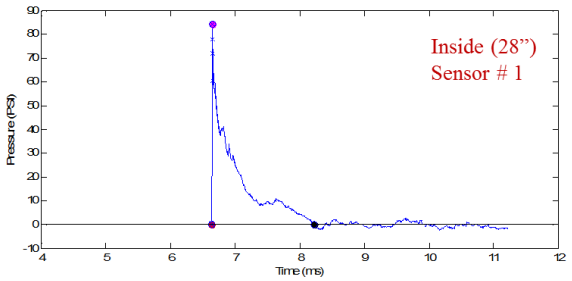
Inside (28")
Sensor # 1
Pressure (PSI)
Time (ms)

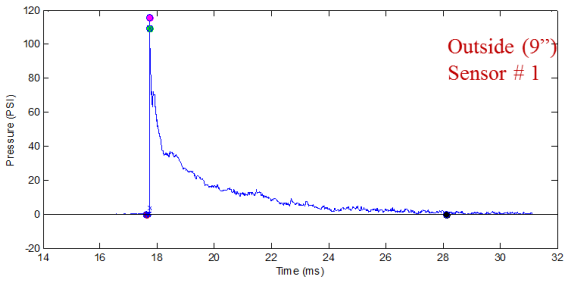
Outside (9")
Sensor # 1
Pressure (PSI)
Time (ms)

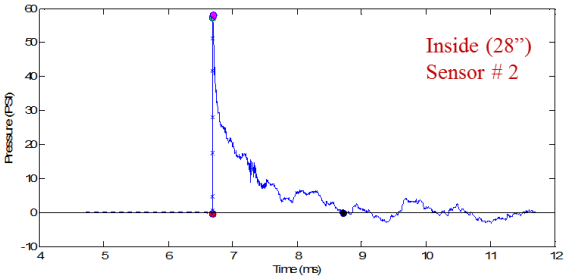
Inside (28")
Sensor # 2
Pressure (PSI)
Time (ms)

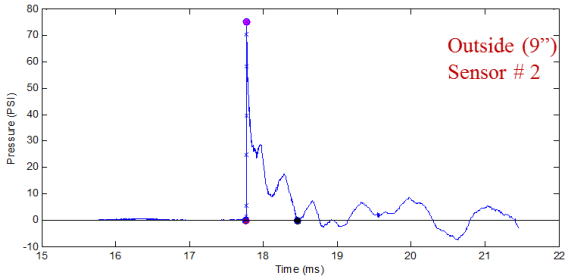
Outside (9")
Sensor # 2
Pressure (PSI)
Time (ms)

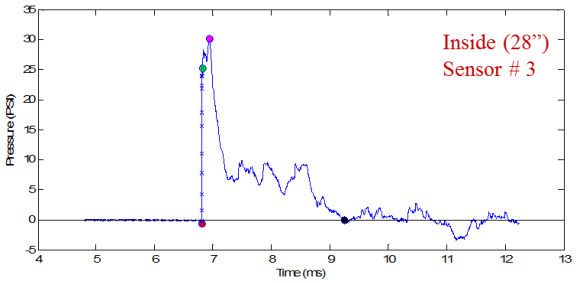
Inside (28")
Sensor # 3
Pressure (PSI)
Time (ms)

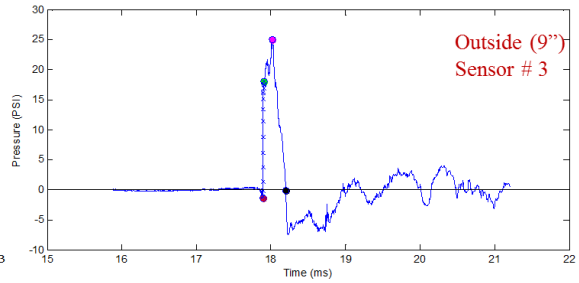
Outside (9")
Sensor # 3
Pressure (PSI)
Time (ms)

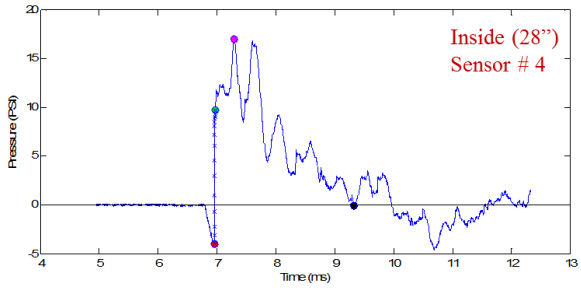
Inside (28")
Sensor # 4
Pressure (PSI)
Time (ms)

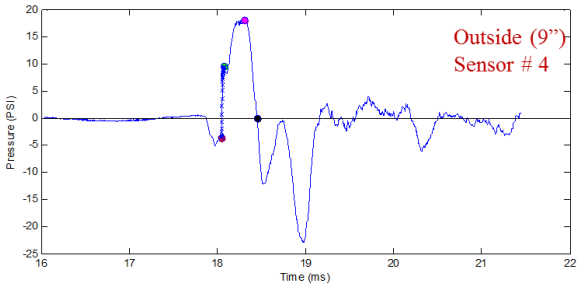
Outside (9")
Sensor # 4
Pressure (PSI)
Time (ms)

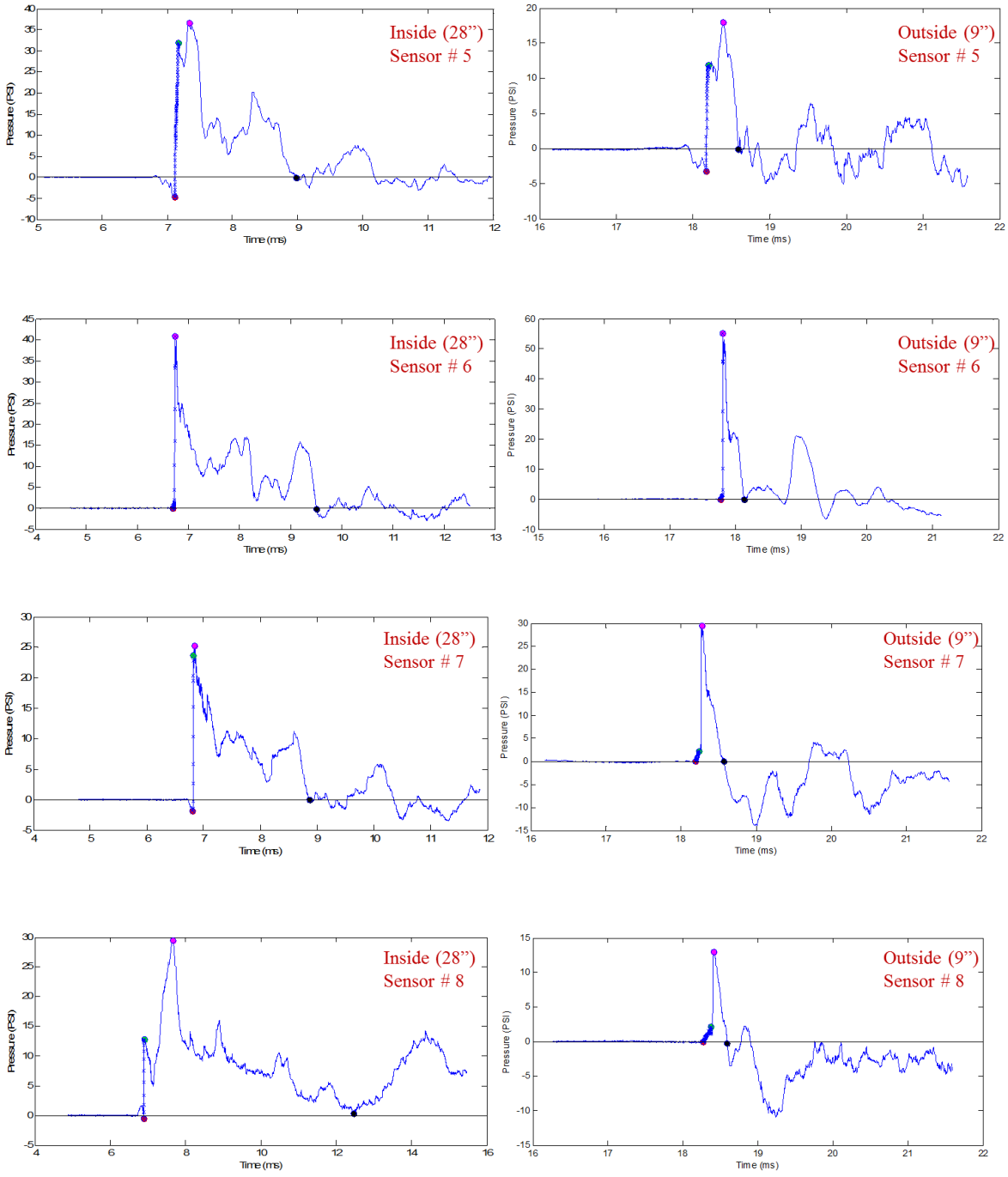
Inside (28")
Sensor # 5
Outside (9")
Sensor # 5
Inside (28")
Sensor # 6
Outside (9")
Sensor # 6
Inside (28")
Sensor # 7
Outside (9")
Sensor # 7
Inside (28")
Sensor # 8
Outside (9")
Sensor # 8
Pressure (PSI)
Time (ms)

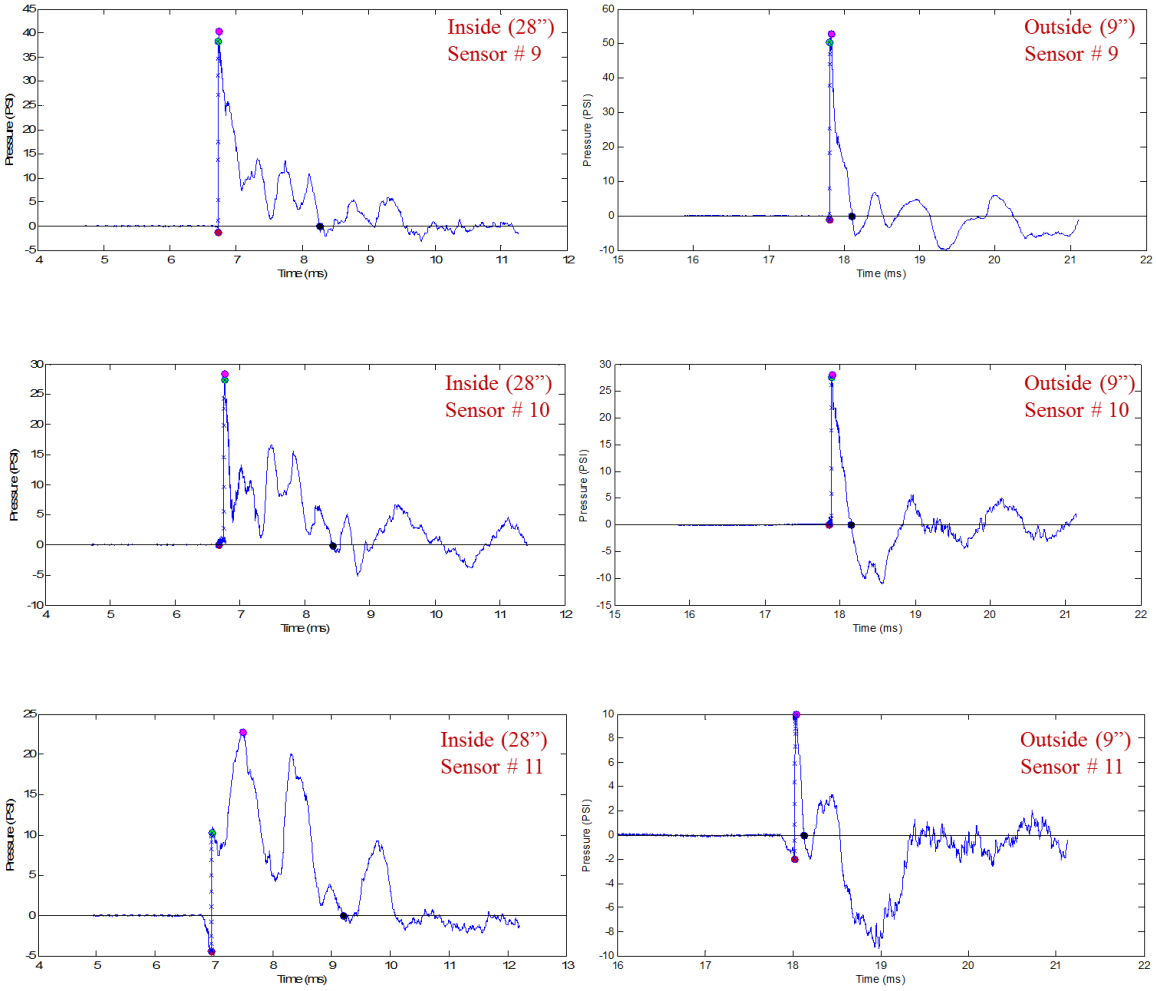

Figure 4.15: Shows the comparison of pressure profile between 28 in. short duration shot and 9 in. D1 shot.

4.4. Summary

Study was conducted to compare the surface pressure and linear acceleration of the RED head for various loading parameters in shock tube and free field explosive loading. Furthermore, a comparison between performing tests inside and outside of a shock tube was also done. In cases where a power problem is indicated, additional experiments with

the same input shock profiles may have to be carried out to increase the power or reduce the chance of type II error. Summary of the chapter is as follows.

- It was determined there is some difference in the peak overpressure between 28 in. short duration shots and free field shots with the maximum difference being 17.29 psi in sensor 2. These differences may be attributed to: (a) variation in the incident pressure between free field (25 psi) and 28 in. short (28 psi), (b) once the shock front impinges the surface of the subject, it diffracts and tends to engulf the whole head. This diffraction and pattern of fluid flow depends on the point of impingement but also on the local geometry. Consequently, this causes the variation in the maximum overpressure. There is a good qualitative match between the pressure profiles, which indicates the capture of essential physics of the phenomenon.
- Generally, the maximum positive acceleration has less difference (29.37 g, for 28 in. short duration shot) when compared to the field data; however, for almost all cases when the head was placed inside the maximum negative acceleration is higher in the shock tube than in the free field-testing. The exact cause of this is phenomenon is still unknown.
- In the case where helmet was used, the overpressure for sensors 1, 2, 3, and 5 has the maximum variation when compared with the field data. However, this difference is not more than 14.19 psi (28 in. short duration inside). The acceleration of the helmeted head is higher when compared to the bare head in the shock tube. This might be due to the buildup of force in the concave helmet inner surface.

- When placed outside the shock tube, there is a reduction in the overpressure and positive time duration when compared with shots inside the shock tube, which can be seen in the pressure profiles comparison shown in Figure 4.15. Especially, overpressure seems to be reduced or remain equal to that measured in the experiments conducted inside the shock tube in all but sensors 1, 2, 6, and 9, even though the 9 in. D1 shot had a higher incident pressure.

Now that the validity of the shock tube is established, the proposed experimental technique was used for developing an animal model to study the effects of test section location as well as the biomechanical loading on rats (relationship between incident, reflected and intracranial pressures), which is explained in the following chapter

CHAPTER 5: EFFECT OF PLACEMENT LOCATION ON BIOMECHANICAL LOADING EXPERIENCED BY THE SUBJECT

5.1. Introduction

The goal of this chapter is twofold: 1) to understand the relationship between the animal placement location (APL), i.e., test section along the length of the shock tube and related biomechanical loading on rat, 2) to evaluate the effect of the incident peak overpressure on the biomechanical loading (surface and intracranial overpressures) experienced by the animal

5.2. Materials and Methods

5.2.1. Shock tube

Experiments were carried out in the 229 mm x 229 mm (9 in.x9 in.), cross-section shock tube designed and tested at the University of Nebraska-Lincoln's blast wave generation facility [96]. The three main components of the shock tube are the driver, transition, and straight/extension sections (includes test section) (Figure 5.1). The driver section is filled up with pressurized gas (e.g. Helium) separated from the transition by several Mylar membranes. The remaining sections contain air at atmospheric pressure and at room temperature. The transition section is an “adapter” for seamless circular-to-square cross-

section conversion. The square cross-section is designed to facilitate observation and recording of the specimen-blast wave interactions using high speed video imaging techniques (typically frame rates of 5,000-10,000 frames per second are used). Upon membrane rupture, a blast wave is generated, which expands through the transition and develops into a planar shock-blast waveform in the extension section.

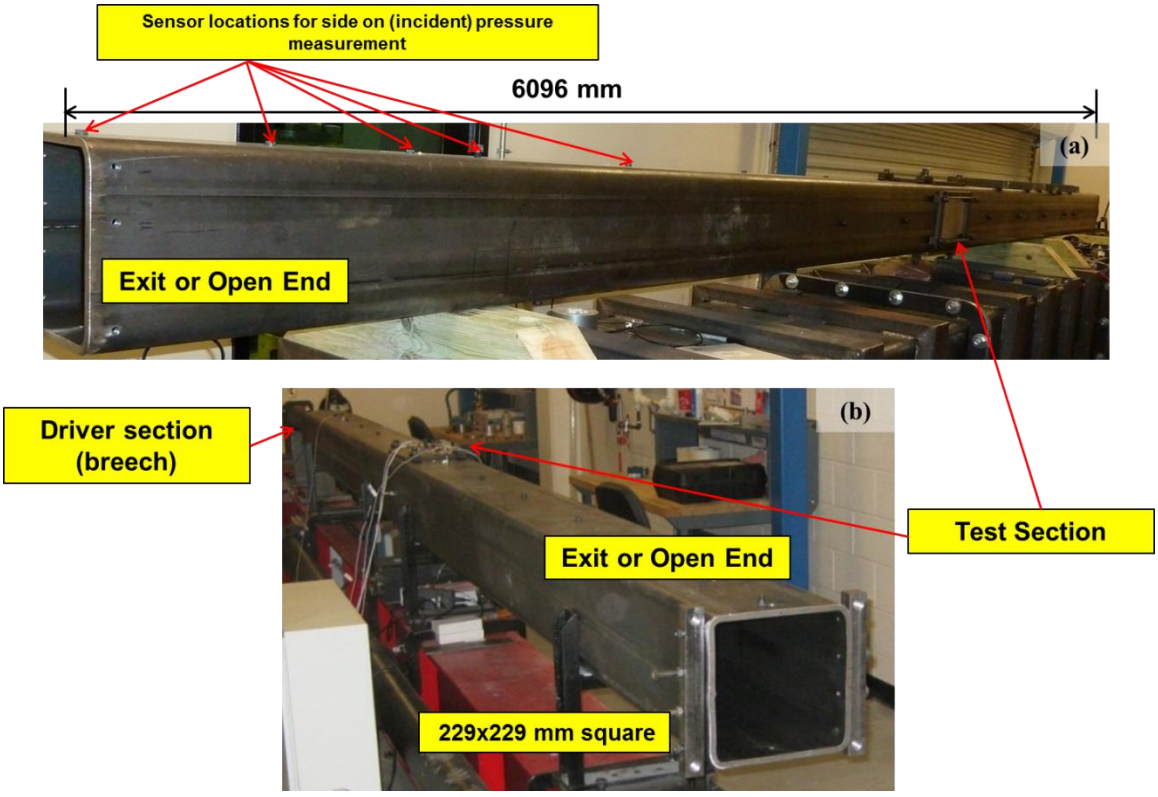

Figure 5.1: Shock-blast wave generator at the University of Nebraska Lincoln. (a) Locations where incident (side-on) pressures are measured are shown. (b) Test section represents animal placement location (APL) corresponding to (a) in the text. Transparent windows.

The test section is strategically located to expose specimens to the blast wave profile of interest (Friedlander in this case). The shock tube is designed and built to obtain a fully developed planar shock-blast wave in the test section, located approximately 2800 mm from the driver (the total length of the shock tube is 6000 mm) [96]. The cross-sectional dimensions of the shock tube is designed such that test specimen experiences a planar blast wave without significant side-wall reflections.

The planarity of the blast wave is verified through blast wave arrival time measurements made along the cross-section of the test section of the shock tube [97]. By varying the length of the breech (i.e., driver section) and by varying the number of Mylar membranes, blast parameters (overpressure, duration and impulse) can be varied. This ability to vary blast parameters is important to replicate various field scenarios and to study the effects of a blast spectrum on animal response.

5.2.2. Sample preparation and mounting

Approval from the University of Nebraska Lincoln's Institutional Animal Care and Use Committee (IACUC) was obtained prior to testing. All the animals were obtained from Charles Rivers® Laboratory and were housed in the same conditions. Five, male Sprague Dawley rats of 320-360g weight were sacrificed by placing them in a carbon dioxide (CO2) chamber for approximately 5 minutes until all movements had ceased. The death of the animal was confirmed before the experiment by ensuring no reaction to a noxious stimulus. Immediately following the sacrifice, a pressure sensor was placed on the nose, and two additional sensors were implanted in the thoracic cavity and in the brain respectively.

Figure 5.2 shows the schematic of the approximate positions of these sensors. Surface mount Kulite sensor (model # LE-080-250A) was used on the nose, and probe Kulite sensors (model # XCL-072-500A) were used for the thoracic cavity and brain. Kulite probe sensors have a diameter of 1.9 mm and a length of 9.5 mm. The sensor implantation was performed as follows: the brain sensor was inserted through the foramen magnum 4-5 mm into the brain tissue.

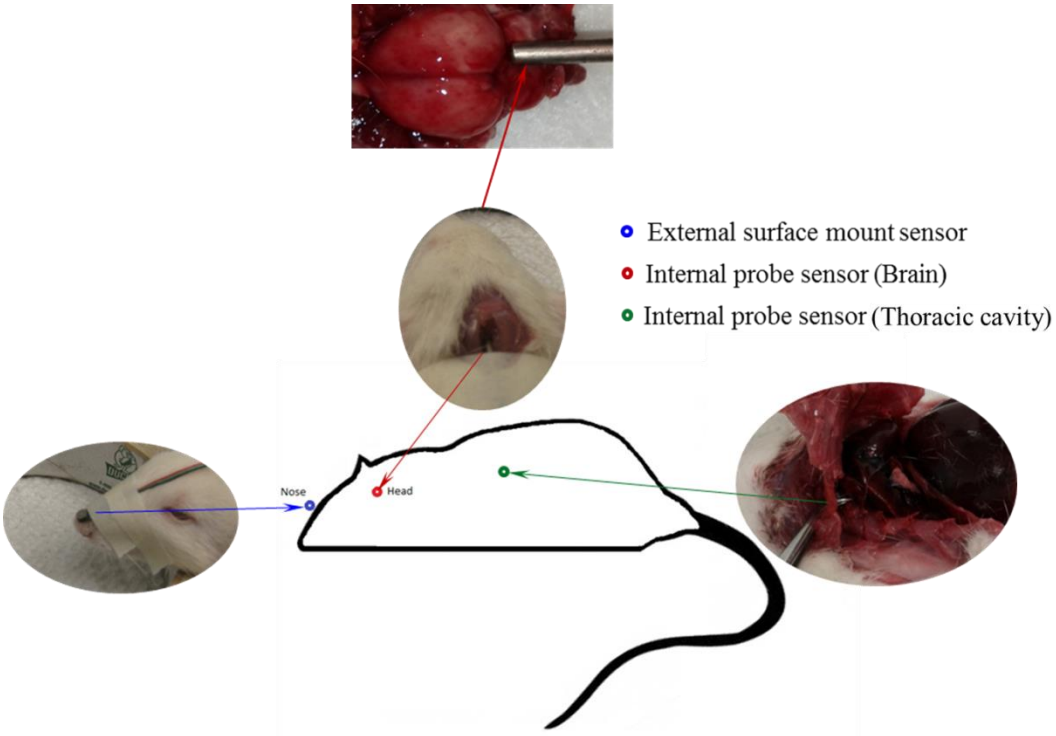

Figure 5.2: Location of surface/internal pressure sensors on the rat model. External surface pressure gauge (model # LE-080-250A) on the nose measures reflected pressure (actual pressure that loads the animal). Internal pressure probe (model # XCL-072-500A) in the head and the lungs measure intracranial and thoracic pressures respectively.

Before inserting the sensor, the tip of the sensor was backfilled with water to ensure good contact with tissue. If the sensor tip contacts the air, the impedance mismatch between the brain tissue, air, and sensing membrane would create inaccurate pressure measurements.

An aluminum bed was designed and fabricated for holding the rat during the application of blast waves. The aerodynamic riser is attached to the bed to hold the sample away from the surface of the shock tube.

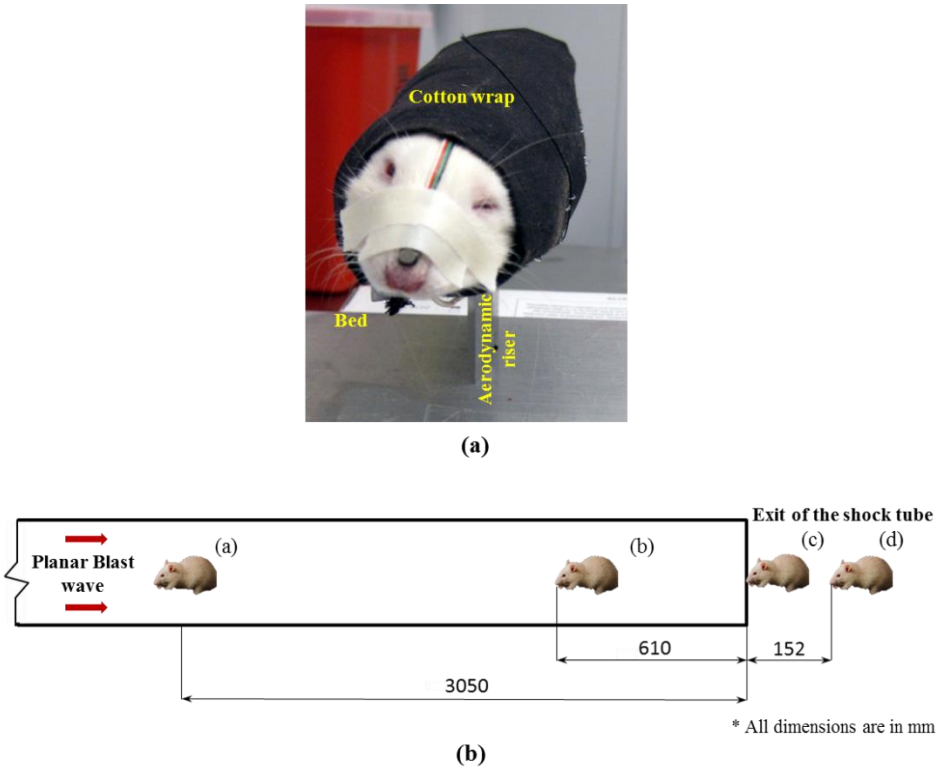

Figure 5.3: (a) Geometric details of the aerodynamic aluminum riser on which rat bed is mounted; the design minimizes blast wave reflection effect. Cotton wrap in conjunction with rat bed secures the rat firmly during the tests. (b) Shows different animal placement (APLs) along the length of the shock tube.

Figure 5.3 (a) shows the placement of rat on the aluminum bed. All the rats were in prone positions and strapped securely against the bed with a thin cotton cloth wrapped around the body.

5.2.3. Blast wave exposure

All rats were exposed to the blast wave at four different animal placement locations (APLs) along the length of the shock tube. These APLs are: a) the test section located at 3050 mm inside from the exit (open end), b) 610 mm inside from the exit, (c) at the open end of the shock tube and (d) 152 mm outside the exit (Figure 5.3 (b)). Control over burst and incident pressure is achieved simply by adjusting the number of Mylar membranes. At animal placement location (a) rats were tested at different average incident overpressures of 100, 150, 200 and 225 kPa with Mylar membranes thicknesses of 0.02, 0.03, 0.04 and 0.05 inches, respectively. At APL (b), (c) and (d) the peak incident pressure was set at 125 kPa. This pressure was achieved with 0.03 membrane thickness in the case of (b), and with membrane thickness of 0.034 for the cases of (c) and (d). For each pressure, the experiment was repeated three times (n=3). High-speed video was recorded at APLs (a) and (c) to identify the motion of the rat, which was not constrained to the rat bed.

5.3. Results

5.3.1. Role of the APL on biomechanical loading

Figure 5.4 shows incident pressure, pressure in the brain and thoracic cavity corresponding to various locations along the length of the shock tube. At APLs (a) and (b) incident pressure profiles follow the Friedlander waveform (Fig. 2.4 (b)) fairly well. Pressure profiles in the brain and thoracic cavity also have similar profiles (the shape is almost identical) to that of the incident pressure profiles. At these locations, peak pressures recorded in the brain is higher than the incident peak pressure and the peak pressure recorded in the thoracic cavity is equivalent to the incident peak pressure.

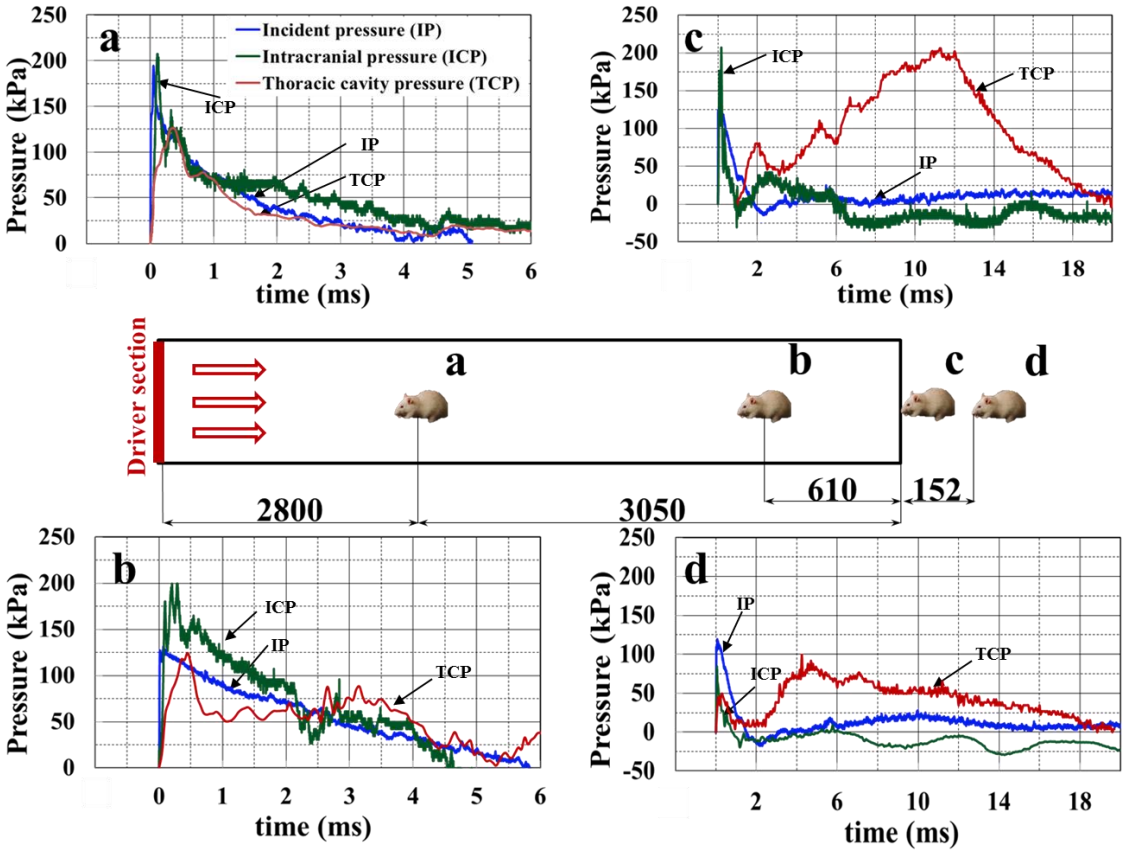

Figure 5.4: Measured pressure-time profile in the brain, thoracic cavity with their corresponding incident pressures at all APLs. At APL (a) and (b) both intracranial and thoracic pressures follow the same behavior as incident pressure; however, in APL (c) and (d) (outside the shock tube) the positive time duration in the brain is reduced drastically and the lung experiences a secondary loading. In this Figure all the dimensions shown are in mm.

It is clear from the Figures that at APL (c) the incident pressure profile differs significantly from the ideal Friedlander waveform; the overpressure decay is rapid and the positive phase duration is reduced from 5 ms at APL (a) to 2 ms at APL (c) (Fig. 5.4 (a) and (c),

respectively). Pressure profile in the brain shows a similar trend. Pressure profile in the thoracic cavity shows a secondary loading with higher pressure and longer duration. Pressure profile in APL (d) position is similar to the pressure profile recorded in the APL (c), except the value of the peak pressure reported in the brain is lower than the incident peak pressure.

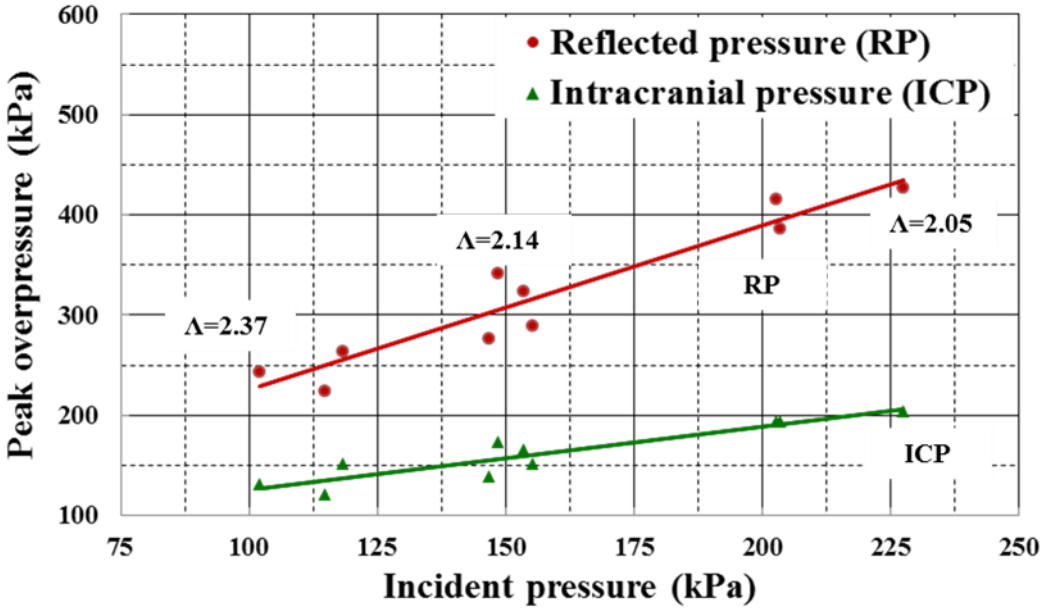

Figure 5.5: Variations of reflected pressure (RP) and intracranial pressure (ICP) with respect to four incident pressures (IP) 100, 150, 150 and 225 kPa at APL (a). Λ represents the ratio of reflected pressures to incident pressures.

5.3.2. Role of incident blast intensity on biomechanical loading

Figure 5.5 shows the plot of peak incident pressure vs. peak pressure on the surface of the rat (nose) and peak incident pressure vs. peak pressure in the brain (intracranial pressure).

The data points are based on the testing at APL (a). Both surface and intracranial pressures are linear functions of the incident pressure.

5.4. Discussion

Distinguishing and reproducing field condition resulting from a realistic military explosion in battlefield is an important TBI research challenge. It is believed that blast wave interaction with the body causing mild and moderate bTBI occur in the far field range where the blast wave is planar and characterized by Friedlander wave. In this scenario, an injury is governed by three key parameters: 1) peak overpressure, 2) the overpressure (positive phase) duration, and 3) positive phase impulse (the integral of overpressure in the time domain). A fourth parameter under-pressure is sometimes considered important and is believed to cause cavitation in the brain, though this is yet to be verified.

It has been reported that input biomechanical loading experienced by the animal determines both the injury and mortality [60, 95]. Thus, it is significant in the study of mild and moderate TBI to reproduce these far field conditions as accurately as possible without any other artifacts. In this work the response of animal at various APLs along the length of the shock tube is studied in order to understand the role of this key parameter on the injury type, severity and lethality. Once the optimal APL is determined parametric studies are conducted to understand the effect of incident blast overpressures on surface and intracranial pressures.

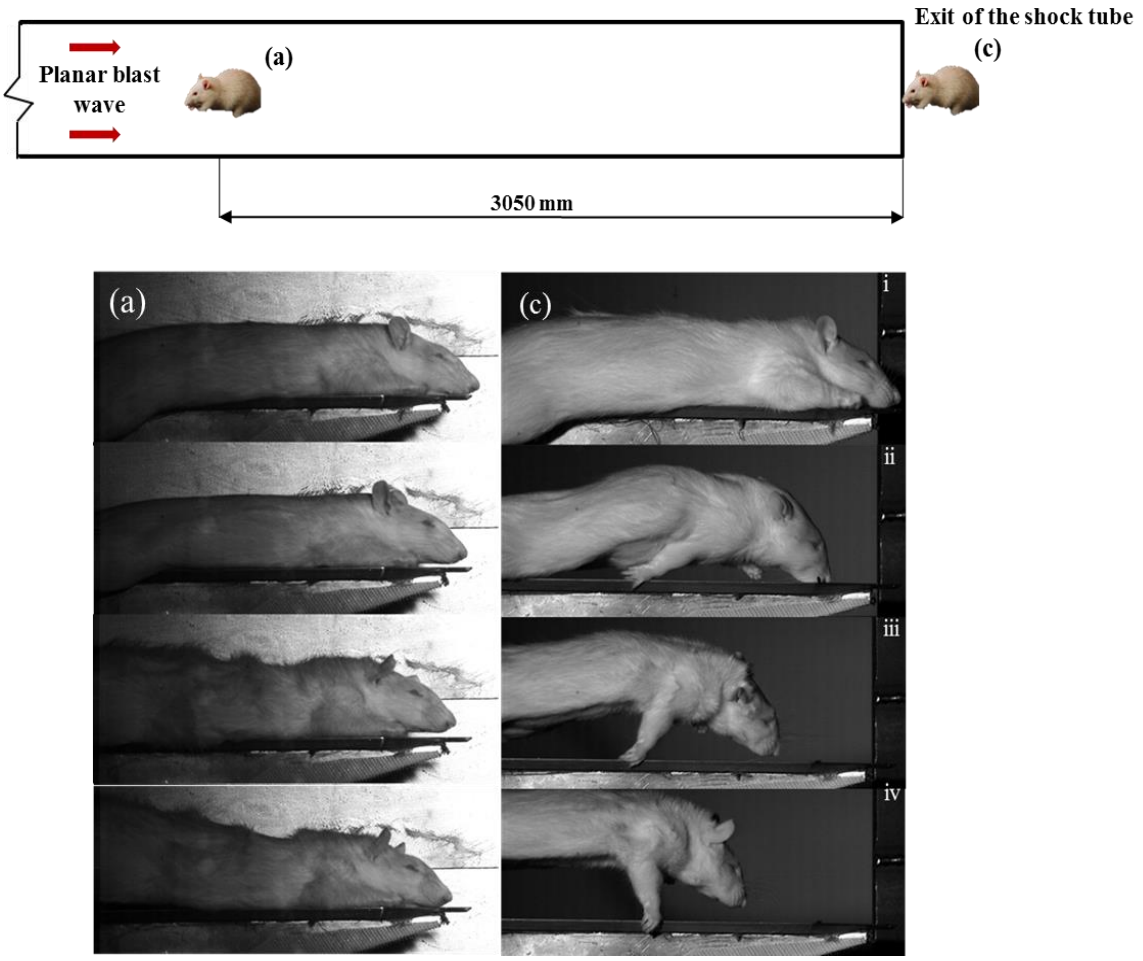

Figure 5.6: Motion of unconstrained rat under blast wave loading (a) inside; (c) outside. (i) to (iv) represents time points t = 0, 20, 40 and 60 ms respectively; the rat is thrown out of the bed when placed outside.

The biomechanical response of the animal significantly varies with the placement location. For APLs inside the shock tube (i.e., (a) and (b), in Figure 5.4) the load is due to the pure blast wave, which is evident from the p-t profiles (Friedlander type) recorded in thoracic cavity and brain. For APLs at the exit (c) and (d), *p-t* profiles show sharp decay in pressure after the initial shock front. This decay is due to the interaction between the expansion

wave from the exit of the shock tube, eliminating the exponentially decaying blast wave, which occurs in APL (a) and (b).

This has two consequences: firstly, the positive blast impulse (area under the curve) reduces drastically. Secondly, since the total energy at the exit is conserved, most of the blast energy is converted from supersonic blast wave to subsonic jet wind [103]. This expansion of blast wave at the exit (subsonic jet) produces entirely different biomechanical loading effect compared to blast wave. Consequently, the thoracic cavity experiences secondary loading, i.e., higher pressure and longer positive phase duration. When the animal is constrained on the bed, this high velocity subsonic jet wind exerts severe compression on the tissues in the frontal area (head and neck) which in turn causes pressure increase in thoracic cavity (lungs, heart). To further illustrate the effect of subsonic jet wind on the rat, experiment at APL (a) and (c) without any constraint was performed. Figure 5.6 shows the displacement (motion) of the rat at various time points starting from the moment the blast wave interacts with the animal. At APL (a), the displacement is minimal; however, at APL (c) the rat is tossed away from the bed (motion) due to jet wind. This clearly illustrates the effect of high velocity subsonic jet wind on the rat when placed outside the shock tube. Consequently, the animal is subjected to extreme compression loading when constrained and subjected to high velocity (subsonic) wind when free, both of which are not typical of an IED blast. This in turn changes not only the injury type (e.g. brain vs. lung injury) but also the injury severity, outcome (e.g. live vs. dead) and mechanism (e.g. stress wave vs. acceleration). Svetlov et al. exposed the rats to the blast loading by placing the rats 50 mm outside the shock tube [95]. They found that the subsonic jet wind represented

the bulk of blast impulse. They concluded that rat was injured due to the combination of blast wave and subsonic jet wind as opposed to a pure blast wave. Similar subsonic jet wind effects are reported by Desmoulin et al. during their experiments on dummy heads placed at the exit of the shock tube [104]. Long et al. studied the effect of Kevlar protective vest on acute mortality in rats. In their experiments all rats (with or without vests) were placed in a transverse prone position in a holder secured near the exit of the shock tube and exposed to 126 and 147 kPa overpressures. The Kevlar vest was completely wrapped around the rat's thorax, leaving the head fully exposed. They found significant increase in survival (i.e., decrease in mortality) of the rat with a protected body. However, without armor only 62.5 % and 36.36 % rats survived at 126 and 147 kPa respectively [60]. This indicates that the lung/thorax experiences significant pressure loads and mortality is higher near the exit of the shock tube. In a separate study performed by Skotak and his team to determine mortality as a function of incident pressures, it was reported that when experiments were performed inside the shock tube APL (a), the rats survive much higher peak overpressures than that reported by Long et al. in their experiments performed outside[40]. Further, the cause of death in our case appears not to arise from lung injuries. In order to better explain the flow dynamics effects at the exit of the shock tube numerical simulations are carried out.

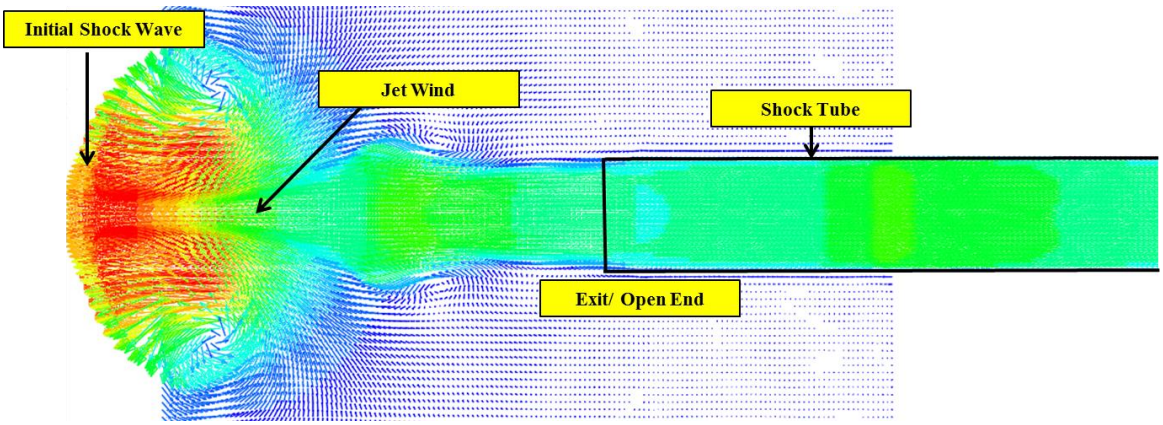

Figure 5.7: Velocity vector field near the exit of the shock tube. Jet wind is clearly visible in velocity vector field along with the initial shock front.

Figure 5.7 shows velocity fields at the exit of the shock tube. No sample (no rat model) is considered in the numerical simulations to demonstrate the 3D nature of flow field once the blast wave exits (the open end of) the shock tube. As the constrained planar blast wave exits the open end of the shock tube, it is fully unconstrained producing a series of fast travelling rarefaction waves (expansion waves) from the edges and vorticities (low pressure regions). These rarefaction waves travel faster than the shock front. The blast wave is nullified; the remaining flow is ejected as subsonic jet winds. Similar effects at the exit of the shock tube are reported by the various researchers through experiments and numerical simulations [103, 105-108]. Due to the spatiotemporal evolution of the blast wave from planar to three dimensional spherical, the blast wave pressure and impulse are reduced drastically as it moves away from the exit of the shock tube.

Another aspect of this work is to understand the relation between the incident, surface, and intracranial pressure at various incident blast intensities at APL (a), an optimal location for the testing. The term “optimal” is used in a very limited sense, in this work. As the shock wave propagates from the driver, the peak overpressure continues to decrease and loses total energy due to the expansion or rarefaction that arrives from the driver. There is a point along the length of the tube, where the peak pressure is maximum and downstream of this point it starts to decay; for this reason, the location where the peak overpressure is maximum is termed as the optimal location (more on this is explained in chapter 3).

We found that both surface pressure and intracranial pressure increases linearly with the incident pressure and both these pressures have higher magnitude than the incident pressure. Pressure amplification is attributed to aerodynamic effects. When the blast wave encounters a solid surface, the incident pressure is amplified, as the high velocity particles of the shock front are brought to rest abruptly, leading to a reflected pressure on the surface of the body. The amplification factor (the ratio of reflected pressure to incident pressure) depends on the incident blast intensity, angle of incidence, mass and geometry of the object and boundary conditions, and can vary by a factor of 2 to 8 for air shocks (Figure 5.5) [109, 110]. This surface pressure is transmitted to the brain through the meninges and the cranium. A few studies compare the pressures in the brain to that of the incident pressures [52, 63-65]. They find that intracranial pressure (ICP) is higher than the incident pressure. This is true even in our experiments. However, this increase in ICP compared to the incident pressures should not lead one to the false conclusion that the pressure increases as it traverses from outside to the brain. It should be noted that due to the mechanics of blast

wave-structure interaction, the surface (reflected pressure) is always higher than the incident pressure by a large factor (typically 2 to 3 though it can reach upto 8); this pressure actually reduces from this higher value to a value possibly more than that of the incident pressure.

$$(p_R = \Lambda * p_I) \qquad (5.1)$$

Thus, ICP should be compared to the surface (reflected) pressure and not just to the incident pressure (Eqn. 5.1). Unfortunately, it is very difficult to measure the surface pressure on the specimen (e.g. animal model) and only the incident side-on pressures are usually reported and compared to ICP. Wave transmission pathway analysis indicates that the main loading pathways for the rat head are the eye socket and the skull; the snout does not play a major role in loading the brain.

Some limitations of the current study are: (i) in this work only prone position with head and body oriented along the direction of the shock wave propagation (perpendicular to the shock front) is considered, which is the commonly used orientation in the current animal model studies with shock tubes [20, 61, 64, 65]. Very recently, Ahlers et al. studied the effect of orientation (side and frontal) on the behavioral outcomes in rat. From their study it was concluded that low intensity blast exposure produced an impairment of spatial memory which was specific to the orientation of the animal [111]. In order to extend our results to this study, the effect of animal orientations at different APL need to be studied separately. It is hypothesized that the loading pathways are likely to be different when orientations (e.g. supine vs. prone) are varied. (ii) Euthanized animals were used in the

experiments. From the tests performed at different post-euthanization time points, it was found that there is no significant variation in the recorded pressures in the brain and in the lungs. Furthermore, euthanized rats were also used by Bolander et al. to record strains on the skull during blast wave interaction [65]. Through acute mechanical loads may not be affected for dead vs. live animals, surely the chronic biochemical sequelae are expected to be different. (iii) Negative pressure (under pressure) in the P-t profile was not included in the study; however, we believe negative pressures may play a key role in possible cavitation behavior, one of a few possible mechanisms currently being explored [112]. (iv) Although, recording acceleration of the rat to study the dynamic effect might give some more useful insight into the problem, it was not done as a part of this study; however, author propose to do it in a separate study in his future work.

5.5. Summary

The effect of animal placement location on the biomechanical loading experienced by the animal is a critical issue that it is not well understood. From current literature it can be seen that different locations, inside and outside the shock tube are both used to induce injury on the animal. However, depending on the location, the biomechanical loading experienced by the animal varies and hence its injury type, severity and lethality may vary as well. It is critical to characterize and understand the biomechanical loading experienced by the animal at different placement locations along the tube in order to recreate field loading conditions on the animal models. In this work rat was placed at four different locations along the length of the shock tube to mimic various options used by other investigators. It

was found that the biomechanical response of the rat varied significantly at these placement locations. Out of these locations, optimal placement location is identified for blast induced neurotrauma studies, well inside the tube where a fully-developed Friedlander wave is first encountered. The optimal location was chosen to study the relationship between incident peak overpressure, surface and intracranial pressures.

- Animal Placement Location plays an important role in the biomechanical loading experienced by the animal.
- For inside the shock tube, Friedlander waves implicated in TBI are best replicated. Thus for animal placement locations deep inside the shock tube, the load experienced by the animal is purely due to the blast wave and not influenced by the three dimensional nature of the events occurring at the exit of the shock tube.
- Near and outside the exit of the shock tube, an expansion wave significantly degrades the blast wave profile and the remaining flow is ejected as a subsonic jet winds. Thus loading experienced by the animal is mainly non-blast jet type loading.
- Due to subsonic jet wind effects at the exit of the shock tube, animals are tossed when free and lung is heavily loaded when the animal motion is constrained. This in turn can change injury type, severity and medical outcome.
- Surface and intracranial pressures vary linearly with incident pressures; intracranial pressures are governed by both surface and incident pressures.

Following the development of the experimental rat model, a three dimensional finite element rat head model was developed study the loading pathways, determine the region

of maximum intracranial pressure and study the effects of varying skull modulus on the intracranial pressure, which is described in next chapter.

CHAPTER 6: DEVELOPMENT AND VALIDATION OF THREE DIMENSIONAL RAT HEAD MODELS

6.1. Introduction

In this chapter, we describe the development of MRI based finite element model of rat head. In addition, computational framework for blast simulations is also described. Finite element (FE) discretization, material models are described in sections 6.2.1 and 6.2.2 respectively. Computational framework for blast simulations based on Euler-Lagrangian coupling is described in section 6.2.3. Boundary conditions are described in section 6.2.4 and the method of solution (including method of Euler-Lagrangian coupling) is described in section 6.2.5. In the next section, validations of the model at different animal placement locations (APL) are presented (section 6.2.6). Finally, the validated model is used for studying the loading pathways and their consequence in the experimental modelling of rat along with effect of skull modulus on intracranial pressure is presented in sections 6.3 and 6.4 respectively.

6.2. Development of rat head model

6.2.1. Finite Element (FE) discretization

A three-dimensional rat head model was generated from the combined use of high resolution MRI and CT datasets of a male Sprague Dawley rat.

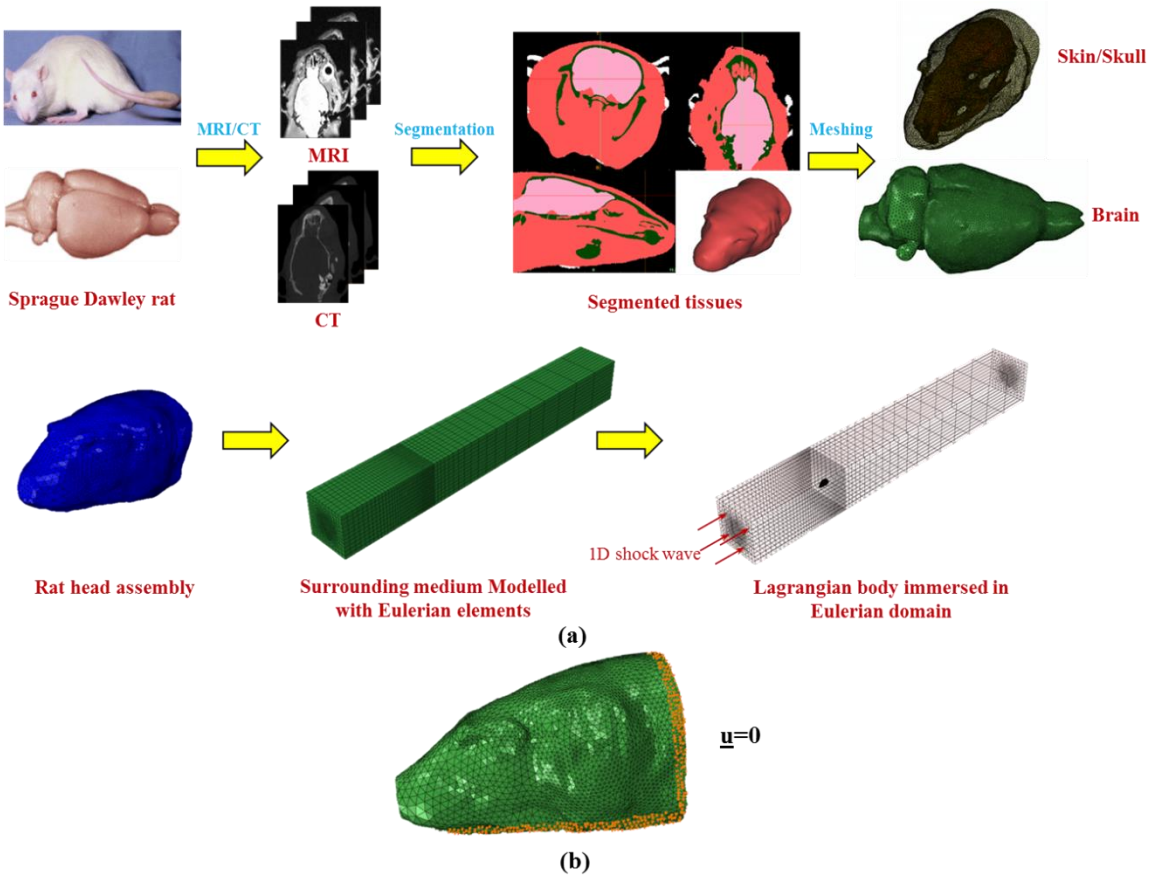

Figure 6.1: (a) The sequence of finite element modeling methodology is shown here. MRI/CT scans of euthanized rats are overlapped, registered, segmented and triangulated using software Avizo 6.2®. the triangulated surface mesh is imported into hypermesh® to generate a 3D mesh consisting of 10 noded tetrahedron Lagrangian elements; this model is imported into finite element software Abaqus® 6.10 and assembled with the Eulerian shock tube. (b) Numerical boundary condition on the rat, displacement in all three linear directions (x, y and z) is constrained from motion.

This technique has already been used to develop realistic human head model from a series of MRI/CT images [109], and to develop two-dimensional model of rat brain [74]. Two different T2-weighted MRI scans (one for the muscle skin and other for the brain), and one CT scan (for the skull and the bones) were used. These three different scans were necessary to achieve proper contrast and segmentation of various tissues (i.e., muscle, skin, brain, skull, and bones). The brain MRI has an isotropic resolution of 256x256x256 pixels, for a field of view of 30 mm in all three directions.The MRI for muscle and skin has an anisotropic resolution, with a pixel size of 512x512x256, for a field of view of 30, 30, and 50 mm respectively. The three datasets were overlapped, registered, segmented, and triangulated using software Avizo 6.2®. The triangulated mesh (i.e., surface mesh) is imported into meshing software HyperMesh® and a volume mesh with 10 noded tetrahedrons element is generated from this surface mesh. The skull, skin and brain share the node across the interface. These elements are treated as Lagrangian elements. The model was then imported into the finite element software Abaqus® 6.10 and the rat model was inserted in the shock tube model.

The generation and propagation of blast waves are modeled in the shock tube environment. The air inside the shock tube, in which the blast wave propagates, is modeled with Eulerian elements (Fig. 6.1). The size of the Eulerian domain corresponds to physical dimensions of the shock tube used in the experiments (cross-section: 229 x 229 mm). A biased meshing approach was adopted with fine mesh near the region of the rat head and coarse mesh elsewhere to reduce total number of elements in the model without sacrificing accuracy. To further understand flow field at the exit of the shock tube and its effect on the head

biomechanical loading, an additional FE model with shock tube and an outside environment was used. The main purpose of this model is to validate rat head model with a different flow conditions; consequently, showing the robustness of model.

6.2.2. Material models

The skin and skull are modeled as linear, elastic, isotropic materials with properties adopted from the literature [113]. Elastic properties in general, are sufficient to capture the wave propagation characteristics for these tissue types and this approach is consistent with other published works [20, 76]. For elastic material stress is related to strain as:

$$\sigma_{ij} = \lambda E_{kk}\delta_{ij} + 2\mu E_{ij} \tag{6.1}$$

Where,

σ is a Cauchy stress, E is a Green strain (also known as Green-Lagrange strain), λ and μ are Lame constants and δ is a Kronecker delta.

Brain is modeled with an elastic volumetric response and viscoelastic shear response. Viscoelastic response is modeled using standard linear solid model. The associated Cauchy stress is computed through:

$$\sigma_{ij} = J^{-1}F_{ik}.S_{km}.F^{T}_{mj} \tag{6.2}$$

where σ is a Cauchy stress, F is a deformation gradient, J is a Jacobian, and S is the second Piola-Kirchhoff stress, which is estimated using following integral:

$$S_{ij} = \int_0^t G_{ijkl}(t-\tau)\frac{\partial E_{kl}}{\partial \tau} d\tau \qquad (6.3)$$

Where E is the Green strain, and G_{ijkl} is the tensorial stress relaxation function. The relaxation modulus for an isotropic material can be represented using Prony series:

Table 6.1: Material properties used in this study (a) elastic material properties, (b) viscoelastic material properties and (c) properties used for modeling air.

(a)

Material	**Young's modulus (MPa)**	**Poisson's Ratio**
Skin	**8**	**0.42**
Skull	**100**	**0.3**
Brain	**0.123**	**0.49**

(b)

Material	**Instantaneous shear modulus (kPa)**	**Long-term shear modulus (kPa)**	**Decay constant** s^{-1}

Brain	**41**	**7.8**	**700**

(c)

Material	**Density (kg/m^3)**	**Gas Constant (KJ/kg-K)**	**Temperature (K)**
Atmospheric	**11.607**	**287.05**	**300**

$$G(t) = G_1 + G_2 e^{\frac{-t}{\tau_r}} \quad (6.4)$$

Where G_1 is the steady state elastic modulus, G_2 is the rubbery modulus, $1/\tau_r = E_2/\eta$ is the decay constant, η is the viscosity and t is the time. From this instantaneous and long term modulus can be deduced as $G_{inst}=G_1+G_2$ and $G_{lt}=G_1$ respectively. For material parameters of the brain tissue, widely accepted bulk modulus value of 2.19 GPa is used in this work. This value is motivated from the works of Stalnaker [114] and McElhaney [115]. Brain tissue is modeled as elastic volumetric response and viscoelastic shear response with properties adopted from the work of Zhang, L.Y., et al. [116]. The material properties of the rat head model is summarized in Table 6.1.

Air is modeled as an ideal gas equation of state (EOS). The Mach number of the shock front calculated from our experiments is approximately 1.4 and hence the ideal gas EOS assumption is acceptable; the ratio of specific heats does not change drastically at this Mach number value. The material property of air is summarized in Table 6.1.

6.2.3. Loading, interface and boundary conditions

As described in the experimental work on rat in chapter 5, model was subjected to blast in the frontal direction. As described by Ganpule in his work, there are two possible techniques to impose the shock conditions: technique (a) Modeling of the entire shock tube, in which driver, transition and extension sections are included in the model so that events of burst, expansion and development of a planar of the blast wave are reproduced; technique (b) Partial model with experimentally measured (*p*-*t*) history is used as the pressure boundary condition, where the numerical model comprises the downstream flow field containing the test specimen. Technique (a) is computationally very expensive and takes about 147 CPU hours on a dedicated 48 processors. These simulations reach the limits of computing power in terms of memory and simulation time. On the other hand, technique (b) requires about 1.26 million elements with 10 CPU hours. The pressure, velocity and temperature profiles obtained using technique (b) match well with the profiles that are obtained using full scale model (technique (a)) at the boundary and downstream locations [117]. Hence, in this study, technique (b) was used to save time without scarifying accuracy. Approach similar to technique (b) has been widely used in shock dynamics studies using shock tubes [106, 118, 119].

The experimental pressure boundary condition (i.e., experimentally measured pressure-time (p-t) profile) was used as an input for the FE simulation. The velocity perpendicular to all other remaining faces of the shock tube is kept at zero to avoid escaping (leaking) of the air through these faces. This will maintain a planar shock front traveling in the longitudinal direction with no lateral flow. The displacement of the nodes on the bottom and rear faces of the rat head is constrained in all degrees of freedom (Figure 6.1 (b)). The interface between all components (skin, skull and brain) was modeled as tied (i.e. no tangential sliding and no separation) contact. An enhanced immersed boundary method is used to provide the coupling between the Eulerian and the Lagrangian domains. Here, the Lagrangian region resides fully or partially within the Eulerian region and provides *no-flow* boundary conditions to the fluid in the direction normal to the local surface. Further, the Eulerian region provides the pressure boundary conditions to the Lagrangian region. Thus, a combination of fixed Eulerian mesh and solid-fluid interface modeling through the enhanced immersed boundary method allows for the concurrent simulations of the formation and propagation of a primary blast wave in a fluid medium and accounts for the effects of both fluid-structure interaction and structural deformations once the blast wave encounters a solid. The interactions (contact conditions) between Eulerian (containing air and a propagating blast wave) and Lagrangian regions are defined using 'general contact' feature (card) in Abaqus®. In general, contact, contact constraints are enforced through the penalty method with finite sliding contact formulation. Various contact property models are available in general contact. In the present work, frictionless tangential sliding with hard contact is used as contact property model.

6.2.4. Solution scheme

The FE model is solved using the nonlinear transient dynamic procedure with the Euler-Lagrangian coupling method (Abaqus® 6.10). In this procedure, the governing partial differential equations for the conservation of mass, momentum, and energy along with the material constitutive equations and corresponding equations defining the initial and boundary conditions are solved simultaneously. Eulerian framework allows the modeling of highly dynamic events (e.g. shock) which would otherwise induce heavy mesh distortion. An enhanced immersed boundary method was used to provide the coupling between the Eulerian and the Lagrangian domains.

The finite element model is solved using the nonlinear transient dynamic procedure with the Euler-Lagrangian coupling method (Abaqus®). In this procedure, the governing partial differential equations for the conservation of momentum, mass and energy (see equations 6-8) along with the material constitutive equations (described earlier) and the equations defining the initial and boundary conditions are solved simultaneously.

Conservation of mass (continuity equation):

$$\rho \frac{\partial v_i}{\partial x_i} + \frac{\partial \rho}{\partial t} + v \cdot \nabla \rho = 0 \qquad (6.6)$$

Conservation of momentum (equation of motion):

$$\frac{\partial \sigma_{ij}}{\partial x_j} + \rho b_i = \rho a_i \qquad (6.7)$$

Conservation of energy (energy equation):

$$\rho \frac{\partial e}{\partial t} + v \cdot \nabla e = \sigma_{ij} \frac{\partial v_i}{\partial x_j} - \frac{\partial q_i}{\partial x_i} + \rho q_S \qquad (6.8)$$

where, ρ is a density, *x, v* and a are displacement, velocity and acceleration of a particle respectively, σ is a Cauchy stress, *b* is a body force, *e* is internal energy per unit mass, *q* is heat flow per unit area and q_S is a rate of heat input per unit mass by external sources.

In Eulerian-Lagrangian method, the whole model is solved (i.e. both Eulerian and Lagrangian domains) with the same Lagrangian equations. The notion of a material (solid or fluid) is introduced when specific constitutive assumptions are made. The choice of a constitutive law for a solid or a fluid reduces the equation of motion appropriately (e.g., compressible Navier-Stokes equation, Euler equations etc.). For the Eulerian domain in the model the results are simply mapped back to the original mesh with extensions to allow multiple materials and to support the Eulerian transport phase for Eulerian elements. Eulerian framework allows for the modeling of highly dynamic events (e.g. shock) which would otherwise induce heavy mesh distortion. In Abaqus® the Eulerian time incrementation algorithm is based on an operator split of the governing equations, resulting in a traditional Lagrangian phase followed by an Eulerian, or transport phase. This formulation is known as "Lagrange-plus-remap." During the Lagrangian phase of the time increment nodes are assumed to be temporarily fixed within the material, and elements deform with the material.

6.2.5. Validation of finite element model

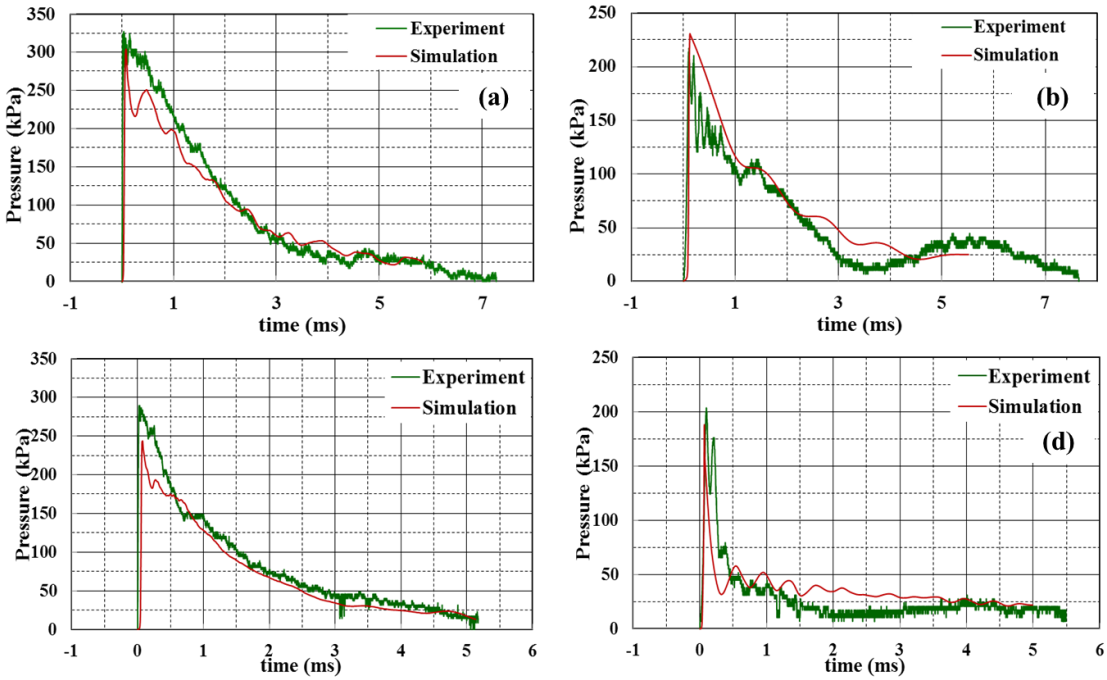

Figure 6.2: Comparison between experiments and numerical models both inside and outside the shock tube, (a) Surface pressure measured on the nose, (b) intracranial pressure inside the brain; (a) and (b) are measured at Animal Placement Location (APL) (a) i.e., inside the shock tube, (c) Surface pressure measured on the nose, (d) intracranial pressure inside the brain; (c) and (d) are measured at APL (c) i.e., outside the shock tube.

During the Eulerian phase of the time increment deformation is suspended, elements with significant deformation are automatically remeshed, and the corresponding material flow between neighboring elements is computed. As material flows through an Eulerian mesh, state variables are transferred between elements by advection. Second-order advection is used in the current analysis. The Lagrangian (solid) body can be a deformable body and

can deform based on the forces acting on it and the deformation of the Lagrangian solid influences the Eulerian domain. In current analysis 8 noded brick elements are used for Eulerian elements and 10 noded tetrahedron for Lagrangian elements. We found that at Animal Placement Location (APL (a)) (refer Figure 5.3 (b)), optimized loading conditions in the shock tube exist. Consequently, in the finite element model the APL (a) was preferred to perform the extended sets of finite element simulations. Before we use this finite element model to make predictions it is necessary to validate the model against experimental data. Figure 6.2 (a), (b), (c) and (d) show comparison of p-t profiles for the nose and the brain sensors at APL (a) and (c) respectively. These two locations were chosen to show the validity of the model for two different loading conditions. Furthermore, we wanted to verify whether the model could capture these changes in loading condition. There is a good agreement between the experiment and finite element simulation in the APL. Hence, the model can be used as a predictive tool towards understanding blast induced loading on rat.

6.3. Application of the numerical model

The validated model was used to study the blast induced loading on the rat. In this study, effect of increasing incident pressure is analyzed through the studying intracranial pressure and skull strains for carious skull modulus. Finally, the loading pathways induced due to blast interaction with head and the subsequent wave propagation on the brain was studied.

6.3.1. Relationship between incident pressure and intracranial

Figure 6.3 shows the relationship between the incident pressure and intracranial pressure. From the Figure, it can be seen that IP and ICP has a positive linear relationship; i.e., with increase in the IP, the ICP increases linearly while the material property of the skull is kept same. This result is also experimentally corroborated with results from section 5.3.2. Where the Sprague Dawley rat was subjected to different incident pressure while the intracranial pressure was recorded. It was shown that there was a positive linear relationship between intracranial pressure and incident pressure.

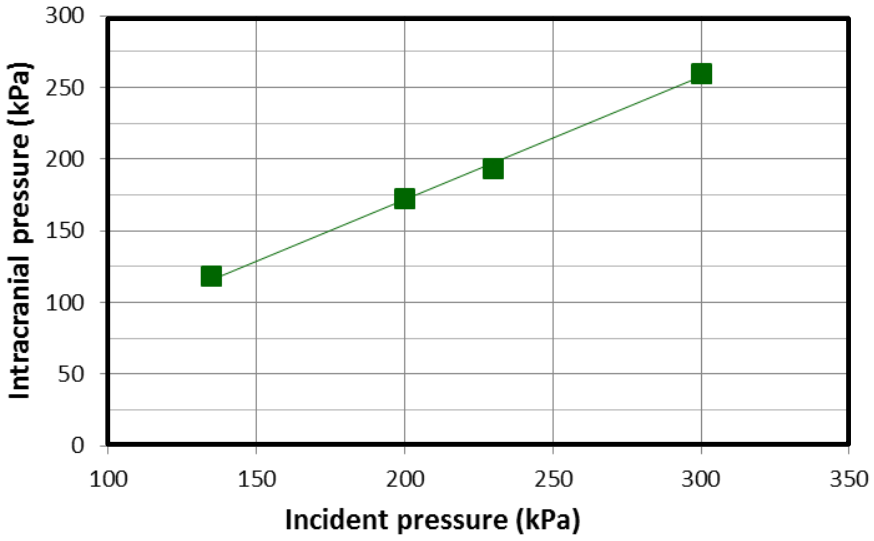

Figure 6.3: Relationship between incident pressure and intracranial Pressure.

6.3.2. Effect of skull modulus

Figure 6.4 shows the relationship between the intracranial pressure and the rigidity of the skull.

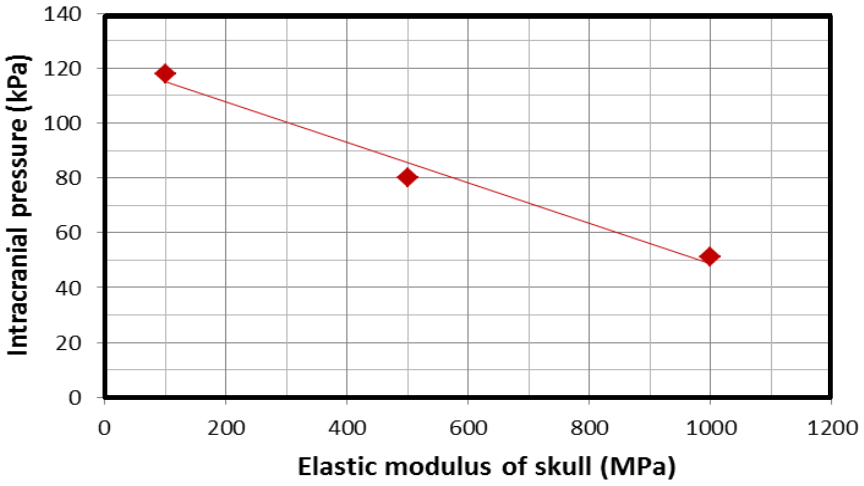

Figure 6.4: Relationship between elastic modulus of the skull and intracranial pressure.

From the Figure, it can be seen that there is a negative linear relationship between the rigidity of the skull and intracranial pressure; i.e., with increase in the skull rigidity the pressure experienced in the brain decreases. The reason for this is further explained in section 7.4.

6.3.3. Strains recorded in skull

Figure 6.5 shows the strain recorded in the skull for three different rigidities. Unlike ICP, the strains on the skull have a negative nonlinear relationship with respect to rigidity. There is oscillation in the strain, which indicates the vibratory nature of the loading. Furthermore, these oscillations closely follow the decay pattern of the applied incident pressure. Strain behavior and the oscillations look very similar in the case 500 and 1000 MPa.

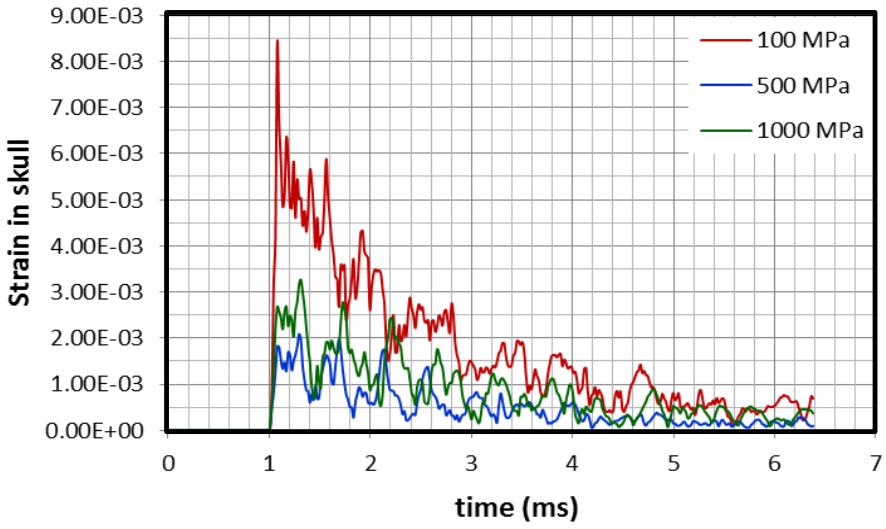

Figure 6.5: Skull maximum principle strain history for varying values of skull rigidity varied between 100,500, and 1000 MPa.

These oscillations can be attributed to the flexuring of the skull. Similar results are observed by Bolander and his collegues in their study on male Sprague Dawley rats [65]. Cause and consequence of this relationship is further demonstrated in chapter 7.

6.4. Wave transmission pathways

Figure 6.6 (a) and (b) show the pressure contour plots on the surface, around and inside the brain of the rat. As the blast wave impinges the rat, the blast wave first interacts with the snout and undergoes diffraction, where it bends and converges towards the eye socket (pathway 1) and top of the skull (pathway 2) (Figure 6.6 (a)). The surface pressure loadings along pathway 1 and pathway 2 are transmitted to the rat brain as depicted in Figure 6.6 (b). These transmitted waves start moving into the rat brain and at the same time converge

towards each other in the region of bregma, lambda and midline sutures. The loading through the snout (pathway 3), does not reach the brain before the transmitted pressure wave from pathway 1 and pathway 2 completely load the brain.

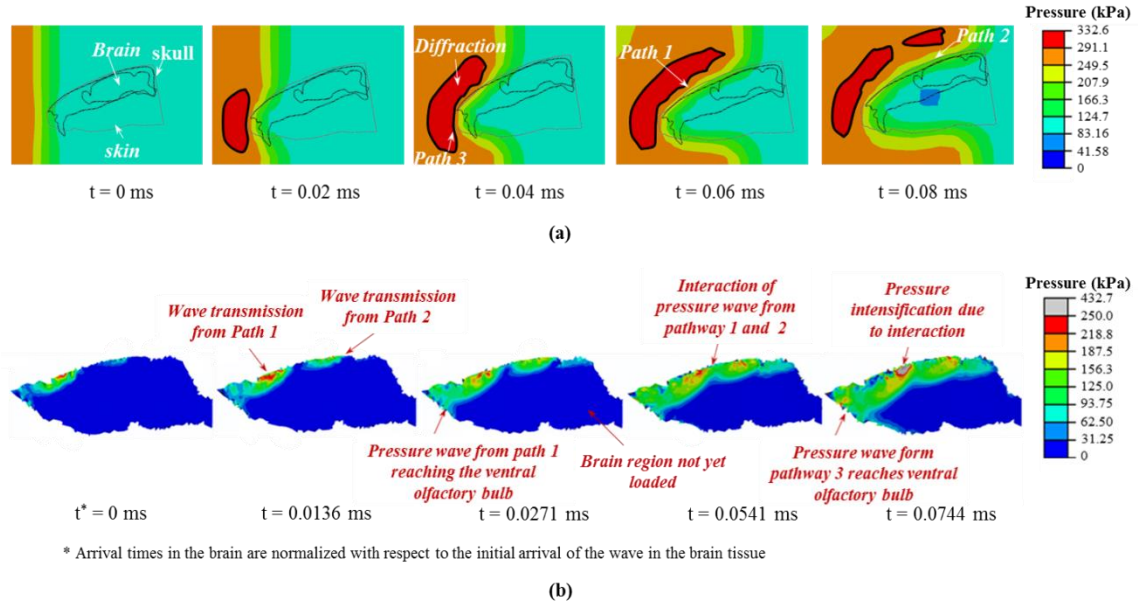

Figure 6.6: Comparison between experiments and numerical models both inside and outside the shock tube, (a) Surface pressure measured on the nose, (b) intracranial pressure inside the brain; (a) and (b) are measured at APL (a) i.e., inside the shock tube, (c) Surface pressure measured on the nose, (d) intracranial pressure inside the brain; (c) and (d) are measured at APL (c) i.e., outside the shock tube.

These results are corroborated by the experimental study done by Bolander and his collegues, where the maximum skull flexure and hence the intracranial pressure were recorded between bregma and lambda of the skull[65]. Although snout does not directly play a role in the pressure transmission to the brain, it plays an indirect role in diffracting

the blast to cause loading in the pathways 1 and 2. Effect of the snout was further investigated using a parametric study in chapter 7.

6.5. Summary

A biofidelic model of the rat head is generated from high-resolution medical imaging data. The rat head model was segmented into three different structures/components namely skin, skull, and brain. Although, geometric details like hippocampus, cerebellum could have been added to the brain, it was not done due to the lack of material model. Computational methodology based on Euler-Lagrangian coupling method is developed to simulate blast events. This computational methodology allows accurate concurrent simulations of the formation and propagation of the blast wave in the air, the fluid-structure interactions between the blast wave and the head model, and the stress wave propagation within the brain. The biofidelic head model was then validated against blast experiments at two different flow condition of the shock tube. The experiment and simulation response is compared using surface pressures and intracranial pressures. Good agreement is seen between the experiments and simulations for both locations. Computer modeling of blast TBI events not only provides the tool for interpreting experimental observations but also forms the basis for additional numerical experiments that are critical in understanding blast TBI. Validated computational model was further used to study the blast induced loading through studying the intracranial pressure and principal strains as a function of incident pressure. Finally, the loading pathways to brain through skull and the subsequent wave propagation in the brain were studied. It was shown that major wave transmission pathway

to the rat brain is through the cranium. The snout plays only a secondary role in biomechanical loading of a rat by diffracting the blast wave towards eye-socket (pathway 1) and skull (pathway 2).

In the next chapter both rat finite element model and experimental model developed in this chapter and the previous chapter were used measure intracranial pressure for various incident pressures; further these data were used as input for developing the nonlinear regression model.

CHAPTER 7: DETERMINATION OF VARIABLES THAT INFLUENCES SCALING OF INTRACRANIAL PRESSURE ACROSS SPECIES USING AN EXPERIMENTAL AND THEORETICAL APPROACH

7.1. Introduction

Final objective of this work is to develop a model that can be used for translating intracranial pressure (ICP) and incident pressure between rat and humans. Consequently, this model would be helpful in developing injury thresholds for blast induced neurotrauma (BINT) for humans. Currently, injury thresholds developed for humans are based on scaling the mass across species, which was originally developed for the pulmonary injury. However, whether this model works for brain injury is yet to be proven experimentally due the difficulties in testing injuries across species for BINT. Therefore, first part of this chapter presents a parametric analysis to show the changes in the relationship between incident pressure and intracranial pressure with respect to change in the geometry of the model (material properties were not varied for this study, although a study on the effect of changing skull modulus for a rat model is presented in section 6.3). In the second part of this work, data obtained from the experimental and numerical studies on rat and PMHS were used for developing a regression model to predict the ICP with incident pressure as a predictor variable. Finally, with this model, a method for developing injury threshold is described and it is compared with the current injury threshold models developed for BINT.

Organization of this chapter is as follows, in section 7.2 the methods used for this study is described. In section 7.3 results for the parametric analyses followed by the description of the results of the regression model. In section, 7.4 discussions of the results were made followed by the summary of this chapter in section 7.5.

7.2. Method

7.2.1. Numerical model for parametric study

To determine the variables that influence the ICP a parametric analysis using a simple ellipsoidal model consisting of skull (with rat skull properties) and brain (rat brain properties) was made. The details of the numerical model setup including loading and boundary condition are shown in Figure 7.1. The base dimension of the ellipsoid was 10.5 mm minor axis and 20.5 mm major axis as brain and skull is 2 mm thick surrounding the brain (Figure 7.1 (a)). 10-noded quadratic tetrahedral element was used for meshing both skull and brain and tie contact is established between the inner surface of the skull and the outer surface of brain. Blast exposure was done using the numerical technique described in chapter 6. In all the cases a blast pulse with 242 kPa overpressure was applied as loading while the bottom hemisphere of the model (skull and brain) were completely constrained in all degrees of freedom (Figure 7.1 (e) and (f)).

Firstly, the effect of the skull thickness was studied by varying it by 0.2, 0.6, 2, 4, 8 mm (Figure 7.1 (b)). Secondly, the effect of radius of curvature (effect of snout) was studied by varying the major axis of the base ellipsoid on two steps, first to a sphere followed by a

biconvex disc (Figure 7.1 (c)). The third and final variable that was studied is the effect of cross sectional area (to study the effect of head size) on the ICP. Here the area was varied by varying the minor axis length by 12.5, 17.5, 50 and 88 mm (Figure 7.1 (d)). To maintain the ratio between major and minor axis of the ellipse the major axis was also appropriately changed.

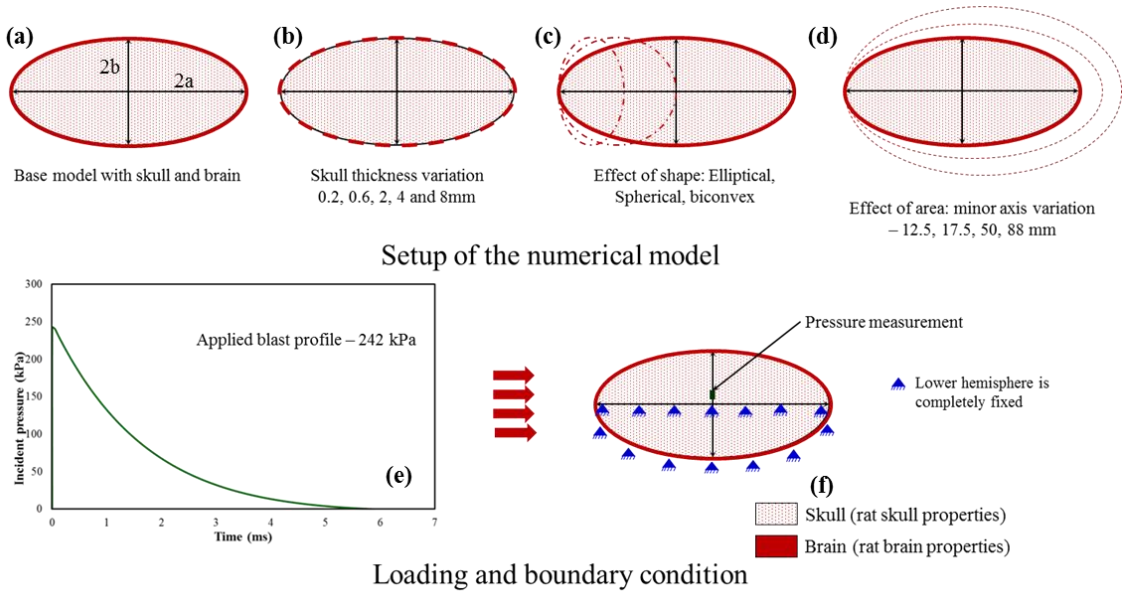

Figure 7.1: Numerical model setup for parametric analysis, (a) base model where a and b are the major and minor axis respectively, (b) skull thickness variation, (c) radius of curvature variation, (d) cross sectional area variation, (e) blast loading profile and (f) boundary condition.

7.2.2. Experimental and numerical model for ICP measurement on rat and PMHS

7.2.2.1. Experimental Rat model

Rat model described in chapter 5 was used in this work. Five 10 weeks old male Sprague Dawley rats were sacrificed by placing them in a carbon dioxide (CO_2) chamber for approximately 5 minutes until all movements had ceased. The death of the animal was confirmed before the experiment by ensuring no reaction to a noxious stimulus. Immediately following the sacrifice, a probe Kulite (model # XCL-072-500A) pressure sensor was placed in the brain. Figure 5.2 (in chapter 5) shows the approximate positions of this sensor. Kulite probe sensors have a diameter of 1.9 mm and a length of 9.5 mm. Rats were subjected to five different incident pressures 127, 195, 223, 243 and 282 kPa.

7.2.2.2. Experimental PMHS model

Three PMHS heads were used in the current study. PMHS heads were obtained from the 'University of Virginia Center for Applied Biomechanics' laboratory. All specimens were handled, prepared and used in accordance with local and federal laws. Ethical guidelines and research protocol approved by the University of Nebraska institutional review panel for PMHS use were also followed. The specimen had no record of osseous disease and pre-existing fractures were not present as confirmed by CT imaging. The age, gender, and basic anthropometry of the specimen are listed in Table 7.1.

PMHS specimens were not fresh and had been kept refrigerated at 'University of Virginia Center for Applied Biomechanics' laboratory for several months. All heads were thawed/defrosted 24 hours prior to the testing. Since PMHS heads were not fresh, brain was significantly degraded (for each specimen). Thus, the brain was removed from each PMHS head and the intracranial space was backfilled with ballistic gelatin. The brain tissue

and dura mater were removed through foramen magnum using flat head screw driver. '20% ballistic gelatin' (ballistic gel, from here on) was prepared by dissolving 2 parts of '250 bloom gelatin' into 9 parts of warm (@40 °C) water (by mass), stirring the mixture while pouring in the powdered gelatin. The gelatin is obtained from Gelita USA Inc. (Sioux, IA) in the bloom form. The ballistic gel is poured in the intracranial cavity through foramen magnum and allowed to settle at room temperature. After ballistic gel is settled the entire head was put inside the plastic bags and air bubbles were removed using vacuum cleaner. The foramen magnum was sealed using filler material (Bondo®). Hybrid III neck was attached to the head using base plate. Base plate was screwed to the bottom of the head.

Table 7.1: Characteristics of the three PMHS heads tested in this study [117]

PMHS sr. no.	Sex	Age	Height (cm)	Weight (kg)	Cause of death
1	M	72	175	68	prostate cancer, diabetes
2	M	75	173	79	cardiovascular disease
3	M	65	175	73	Prostate cancer

7.2.2.3. Instrumentation

Although in the original experiment PMHS head was instrumented to measure surface pressures, surface strains and ICPs, for the sake of this study we consider only the ICP measurements on the frontal cortex near forehead [117]. CT imaging was used to verify

locations of the sensors inside the head (Figure 7.2). Similar to rat experiments, ICPs were measured using Kulite probe sensor (XCL-072-500A).

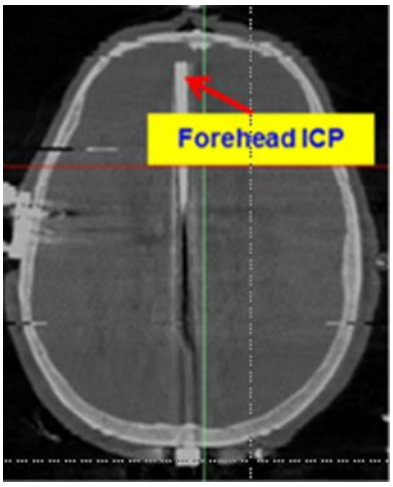

Figure 7.2: CT image of instrumented PMHS showing sensor location, the location of the sensor was chosen very to the skull to reduce errors caused due to the use of ballistic gel [117].

7.2.2.4. Blast wave exposure:

All PMHS heads are subjected to blast waves of three different incident intensities or overpressures (70 kPa, 140 kPa and 200 kPa). As mentioned earlier, the PMHS head is placed in the test section of the shock tube located approximately 2502 mm from the driver end; the total length of the shock tube is 12319 mm.

7.2.3. Finite element model

7.2.3.1. Numerical rat model

The numerical model described in chapter 6 was used in this study. Here the rat model was first validated with the experimental results of rat ICP measurements.

7.2.3.2. Numerical human head model

A validated three dimensional finite element model of human head developed previously [117] was used in the study. The three-dimensional human head model was generated from segmentation of high resolution MRI data obtained from the Visible Human Project [120]. The MRI data consists of 192 T1-weighted slices of 256x256 pixels taken at 1 mm intervals in a male head. The image data is segmented into four different tissue types: 1) skin, 2) skull, 3) subarachnoidal space (SAS) and 4) brain. The segmentation uses 3D image analysis algorithms (voxel recognition algorithms) implemented in Avizo®. The segmented 3D head model is imported into the meshing software HyperMesh® and is meshed as a triangulated surface mesh. The volume mesh is generated from this surface mesh to generate 10-noded tetrahedrons. Tetrahedron meshing algorithms are robust than hexahedral meshing algorithms, and can model complex head volumes like brain and SAS faster and easier [121-123]. Modified quadratic tetrahedral element (C3D10M) available in Abaqus® is very robust and is as good as hexahedral elements (Abaqus user's manual) as far as accuracy of results is concerned [124-126]. In addition, hexahedral elements can suffer from the problem of volumetric locking for highly incompressible materials like brain. The problem of volumetric locking is not present for modified quadratic tetrahedral element (C3D10M) (Abaqus user's manual. The use of specialized 3D image processing (Avizo®) and meshing software (HyperMesh®) allowed for the development of a geometrically accurate FE model.

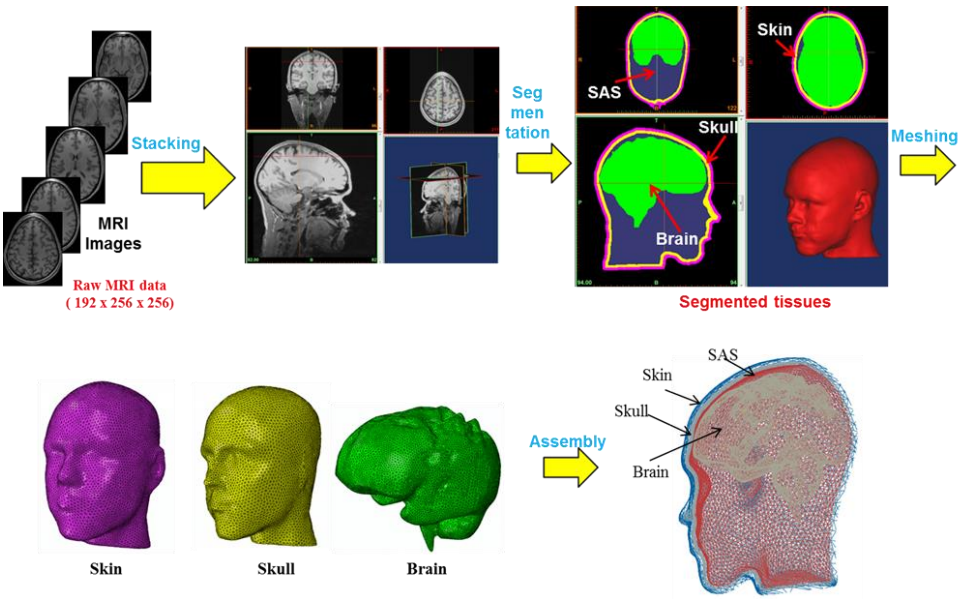

Figure 7.3: Finite Element (FE) discretization, [117].

7.2.3.3. Material models and material parameters used in the head model:

The skin and skull are modeled as linear, elastic, isotropic materials with properties adopted from the literature. Elastic properties in general, are sufficient to capture the wave propagation characteristics for these tissue types and this approach is consistent with other published works [11, 127-131].

For material parameters of the brain tissue, widely accepted bulk modulus value of 2.19 GPa is used in this work. This value is motivated from the works of Stalnaker [114] and McElhaney [115]. The shear properties of the brain tissue are adopted from Zhang et al. [116], who derived shear modulus from the experimental work of Shuck and Advani [132] on human white and grey matter. For material parameters, we relied on widely accepted

values in the literature for base simulations. In addition, parametric studies are conducted to account for reported variations in the brain material properties. The material properties of the head model along with longitudinal wave speeds are summarized in Table 7.2.

Table 7.2: Material Properties (a) Elastic material properties, (b) Viscoelastic material properties of the brain [117].

Tissue type	**Density (kg/m^3)**	**Young's Modulus (MPa)**	**Poisson's Ratio**	**Longitudinal wave speed, C_L (m/sec)**
Skin	1200	16.7	0.42	188.48
Skull	1710	5370	0.19	1856.79
SAS	1000	10	0.49	413.69
Neck	2500	354	0.3	436.60
		Bulk Modulus (MPa)		
Brain	1040	2.19 (a)	0.49999	1451.15

	Instantaneous Shear Modulus (kPa)	**Long-term Shear Modulus (kPa)**	**Decay Constant (sec^{-1})**
Brain	41.0	7.8	700

(b)

7.2.4. Statistical analysis

A 2 x Q nonlinear regression (2 represents two groups rat and PMHS, and Q represents quantitative variable incident pressure) was performed on the resulting experimental data for ICP (criterion variable) in terms of incident pressure and specimen type (rat or human). A total of 8 experimental data sets (5 for rats and 3 for PMHS) along with 8 numerical data sets (using incident pressures different from experiments) were used as input to the statistical analysis. Our initial analysis of the data suggested that ICP had a linear trend for rat and a nonlinear trend for PMHS (showed in section 7.4.4). Therefore, a nonlinear model of the following form was adopted

$$ICP = b_1(IP) + b_2(IP)^2 + b_3(IP).(z) + b_4(IP)^2.(z) + c \qquad (7.1)$$

Where *ICP* is Intra cranial pressure, *IP* is incident pressure, *z* is the type of specimen (here 1- PMHS and 0 - rat) and b_1, b_2, b_3, b_4 and *c* are the coefficients of the model that has to be determined. IBM SPSS 22® statistics package was used to perform the nonlinear regression to determine the coefficient for the model. A stepwise regression approach was used to obtain an optimized model. Stepwise regression is a semi-automated process of building a model by successively adding or removing variables based solely on the t-statistics of their estimated coefficients. At the end, each step is presented as a separate model for further analysis.

7.3. Results

The results of the parametric analysis are shown followed by the result of the numerical and experimental blast simulations on rat and PMHS along with the results of the nonlinear regression model.

7.3.1. Effect of thickness

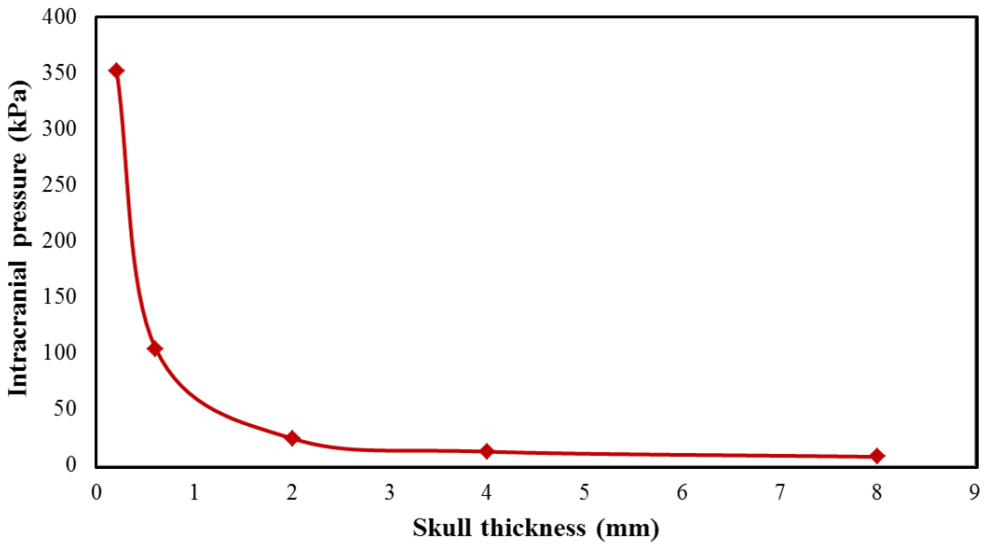

Figure 7.4: Relationship between skull thickness and intracranial pressure (ICP) of an ellipsoid brain system 22.5 mm major axis and 12.5 mm minor axis. Here the thickness of the ellipsoid skull is varied between 0.2, 0.6, 2, 4, and 8 mm.

Figure 7.4 shows the relationship between skull thickness and intracranial pressure (ICP) by having cross section area (variation due to skull thickness changes are negligible) and shape fixed (see Figure 7.1 (b)), when the applied pressure is 242 kPa. We should note the ICP measurements are made in the minor axis as shown in Figure 7.1 (f).

From the Figure, it can be seen that there is a nonlinear relationship between the skull thickness and ICP. That is with increase in thickness, the ICP decreases drastically up to 2 mm and with further increase in the skull thickness the ICP variation is minimal for the given geometry.

7.3.2. Effect of shape

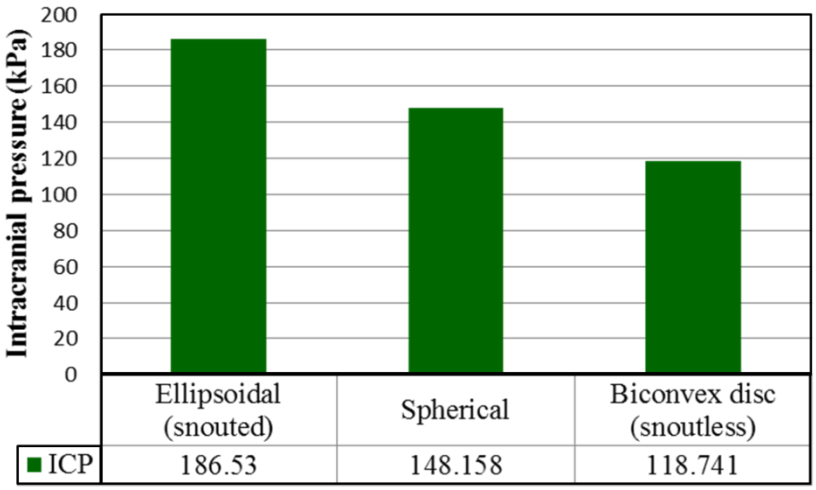

Figure 7.5: Relationship between ICP and shape of the head. Hear the minor axis and skull thickness were kept constant.

Figure 7.5 shows the effect of the shape on the ICP. In this case, the minor axis of the ellipsoid and the thickness of the skull were kept constant whereas the major axis was reduced from ellipsoidal (represents an animal with snout) to spherical and to a biconvex disc (represent human head). From the Figure, it can see that there is a linear reduction in ICP from the ellipsoidal to biconvex disc. The reason for this will be further explained in the discussion section.

7.3.3. Effect of cross sectional area

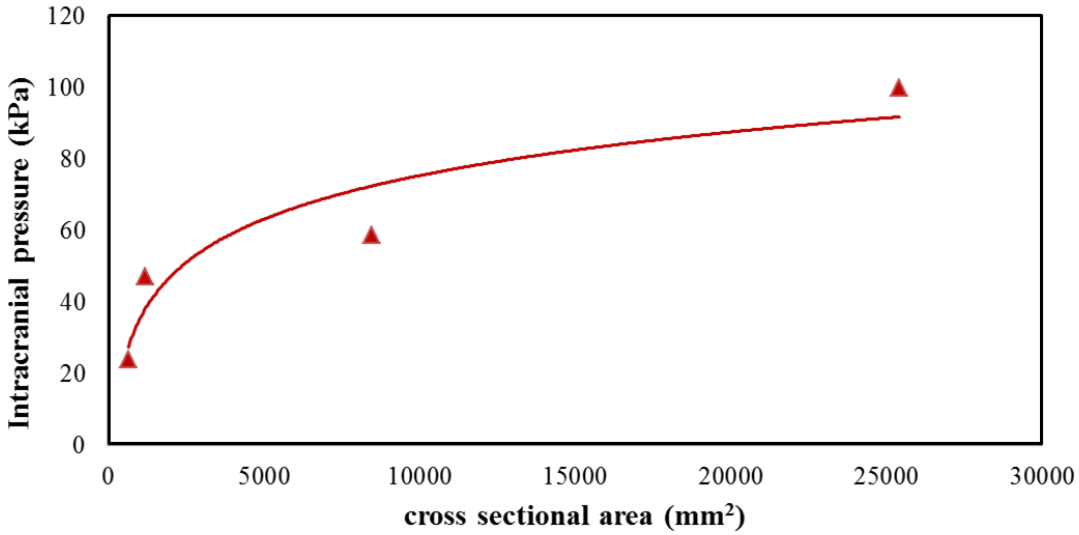

Figure 7.6: Relationship between ICP and head cross sectional area while keeping the shape and skull thickness constant.

Figure 7.6 shows the relationship between ICP and cross sectional area. There is a nonlinear relationship between the cross sectional area and ICP; i.e., ICP increases with increase in the volume of the head exposed to the blast. Furthermore, there is steep increase in the ICP upto 5000 mm^2 and beyond that, the rate of increase of the ICP reduces.

7.3.4. ICPs of PMHS and rat

In this section, the results of the measured ICPs of rat and PMHS are presented. Experimentally ICPs were recorded on 5 rat and 3 PMHS heads. Numerical model of human head and rat head were validated against their corresponding experimental data and the validated models were used as a predictive tool to determine ICP for rat with the experimental incident pressure of PMHS and vice versa. This method was adopted to increase the number of data points of rat ICP for the model.

7.3.4.1. Numerical model validation

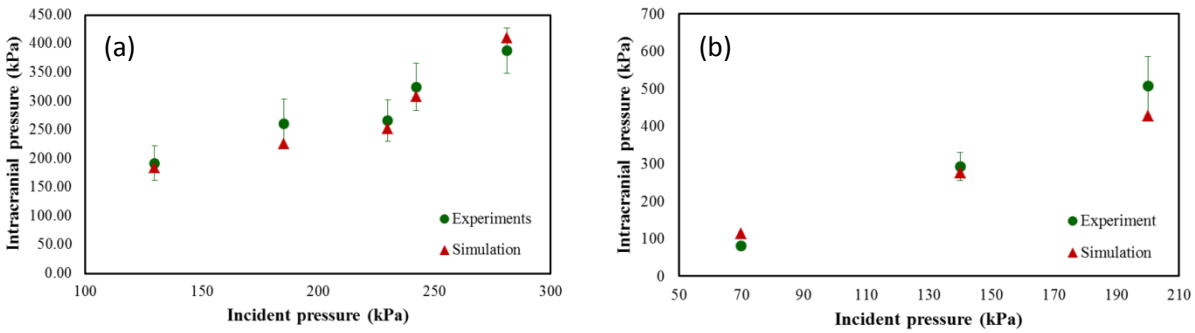

Figure 7.7: Validation of the rat and head numerical for peak ICPs, (a) rat model, (b) human model.

Figure 7.7 shows the validation for peak ICPs between experiment and simulation. Element location, where the ICP is measured in the simulation is approximately matched with the sensor location in the experiment. Since a quadratic tetrahedron element is used, each element has four integration points at which the pressure is calculated. Here, the pressure is calculated in three elements and peak ICP is the average of all the peaks obtained on the 12 pressure time profiles. From the Figure, it can be seen that in both cases (human and rat model) there is a good match between the experiment and the simulation.

7.3.4.2. Incident pressure vs. ICP for humans and animals

Figure 7.8 shows the relationship between incident pressure and the ICP. It can be seen that there is a linear relationship between incident pressure and ICP for rat model, whereas, a quadratic relationship between incident pressure and ICP for a PMHS model. From visual observation, it can be seen that within 70 kPa there is no significant difference in the ICP.

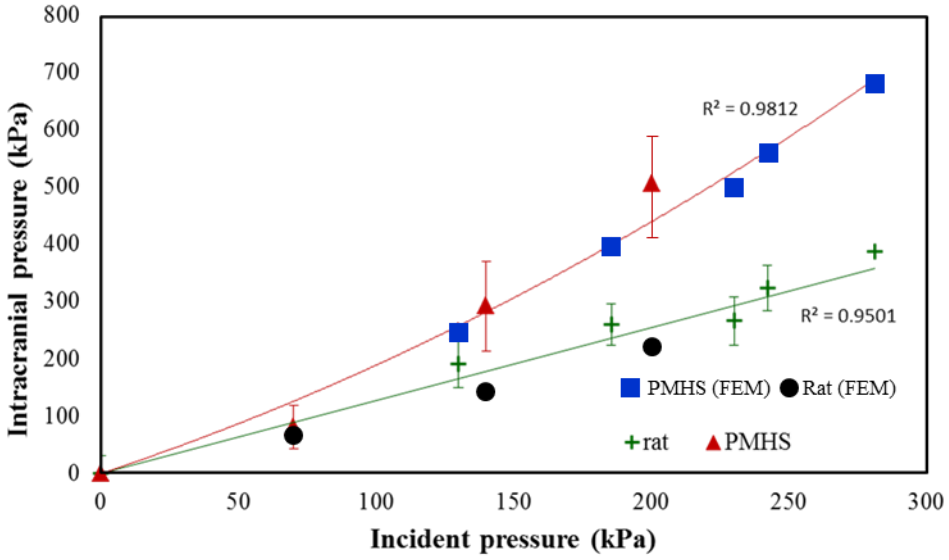

Figure 7.8: Relationship between incident and ICP for rat and PMHS model.

7.3.4.3. Nonlinear regression model to predict ICP for rats and humans

Final part of this work is to construct a model to determine the ICP of rat and human with respect to different incident pressure. From Figure 7.8, it was seen that there was nonlinear relationship between incident pressure and PMHS ICP. In order to consider the nonlinearity as well as the effect of two species, a 2xQ nonlinear regression model was adopted.

Table 7.3: Correlation between the predictor variables and dependent variable (ICP)

Correlations

		Intracranial pressure	animal_type	Incident pressure	square of incident pressure	incidentxtype	square incident x type
Pearson Correlation	Intracranial pressure	1.000	.414	.859	.841	.798	.844
	animal_type	.414	1.000	.000	.000	.810	.696
	Incident pressure	.859	.000	1.000	.956	.414	.485
	square of incident pressure	.841	.000	.956	1.000	.396	.507
	incidentxtype	.798	.810	.414	.396	1.000	.966
	square incident x type	.844	.696	.485	.507	.966	1.000
Sig. (1-tailed)	Intracranial pressure	.	.044	.000	.000	.000	.000
	animal_type	.044	.	.500	.500	.000	.001
	Incident pressure	.000	.500	.	.000	.044	.021
	square of incident pressure	.000	.500	.000	.	.052	.016
	incidentxtype	.000	.000	.044	.052	.	.000
	square incident x type	.000	.001	.021	.016	.000	.
N	Intracranial pressure	18	18	18	18	18	18
	animal_type	18	18	18	18	18	18
	Incident pressure	18	18	18	18	18	18
	square of incident pressure	18	18	18	18	18	18
	incidentxtype	18	18	18	18	18	18
	square incident x type	18	18	18	18	18	18

Table 7.3 shows the Pearson correlation between the predictors and criterion variable. From the Table it can be seen that there is a positive correlation between the predictors and the

criterion variable and these correlations were significant. However, while developing a regression model, it important to consider the collinearity effect, i.e., two variables having a strong relationship with each other and act as a suppressor variable to the model. Hence, it prevents the contribution of the variable that has higher predictive capability resulting in an imperfect model. From the correlation Table it can be seen that there is a strong relationship between incident pressure and square of incident pressure and there is a strong relationship between the product nonlinear predictors (*incident x type* and *incident*^{2} *x type*).

At the same time it should also be known that certain variables although do not have a significant correlation can contribute to the model. Consequently, all the variables above were used as predictors for the model.

Table 7.4: (a) model summary for the stepwise variable addition, (b) ANOVA for both models, (c) regression coefficients for both the models.

(a)

Model Summary

Model	R	R Square	Adjusted R Square	Std. Error of the Estimate
1	.859[a]	.737	.721	102.46323
2	.988[b]	.977	.973	31.57687

a. Predictors: (Constant), Incident pressure

b. Predictors: (Constant), Incident pressure, square incident x type

(b)

ANOVA[a]

Model		Sum of Squares	df	Mean Square	F	Sig.
1	Regression	471327.412	1	471327.412	44.894	.000[b]
	Residual	167979.416	16	10498.714		
	Total	639306.828	17			
2	Regression	624350.348	2	312175.174	313.084	.000[c]
	Residual	14956.480	15	997.099		
	Total	639306.828	17			

a. Dependent Variable: Intracranial pressure

b. Predictors: (Constant), Incident pressure

c. Predictors: (Constant), Incident pressure, square incident x type

(c)

Coefficients[a]

Model		Unstandardized Coefficients		Standardized Coefficients	t	Sig.	95.0% Confidence Interval for B	
		B	Std. Error	Beta			Lower Bound	Upper Bound
1	(Constant)	-31.927	53.073		-.602	.556	-144.435	80.582
	Incident pressure	1.927	.288	.859	6.700	.000	1.318	2.537
2	(Constant)	-5.208	16.497		-.316	.757	-40.371	29.956
	Incident pressure	1.318	.101	.587	12.996	.000	1.102	1.534
	square incident x type	.004	.000	.560	12.388	.000	.004	.005

a. Dependent Variable: Intracranial pressure

Table 7.4 (a) shows the model summary for the two models of the stepwise regression with model 1 having only incident pressure (b_1) as predictors and model 2 having incident pressure along with product of square of incident pressure and animal type (b_4). From the summary, it can be seen that the second model has $R^2=0.98$, which means the model accounts for 98% of the variability of incident pressure, whereas model 1 accounts for only 86% of the variability. Table 7.4 (b) shows the F test for testing the null (H_o: $R^2 = 0$, i.e., no relationship between predictors and criterion). From the results, it can be seen that there is a significant R^2 ($p < 0.001$) for both the model; however, as seen earlier model 2 has the

highest accountability. Table 7.4 (c) shows coefficients of the regression model for both model 1 and 2 along with the *t* test results. Interpretation of the coefficients is as follows. In model 1, predictor incident pressure has a regression b_1 (unstandardized coefficient) of 1.927, i.e., with increase in 1 kPa of incident pressure the *ICP* increases by 1.927. The standardized coefficient beta ($-1<\beta<1$) 0.859 gives the contribution of the particular variable to the model. The t test for coefficient yielded $t = 6.7$, $p < 0.001$, which means the coefficient makes a significant contribution to the model. Second part of the model is the constant; here it gives the value of the *ICP* when the incident pressure is zero. The t test for coefficient yielded $t = -0.607$, $p = 0.56$, which means constant does not make a significant contribution to the model, i.e., *ICP* is zero for zero incident pressure. In model 2, predictor incident pressure has a regression b_1 weight (unstandardized coefficient) of 1.318, i.e., with increase in 1 kPa of incident pressure the *ICP* increases by 1.318. The standardized coefficient beta ($-1<\beta<1$) 0.587 gives the contribution of the particular variable to the model.

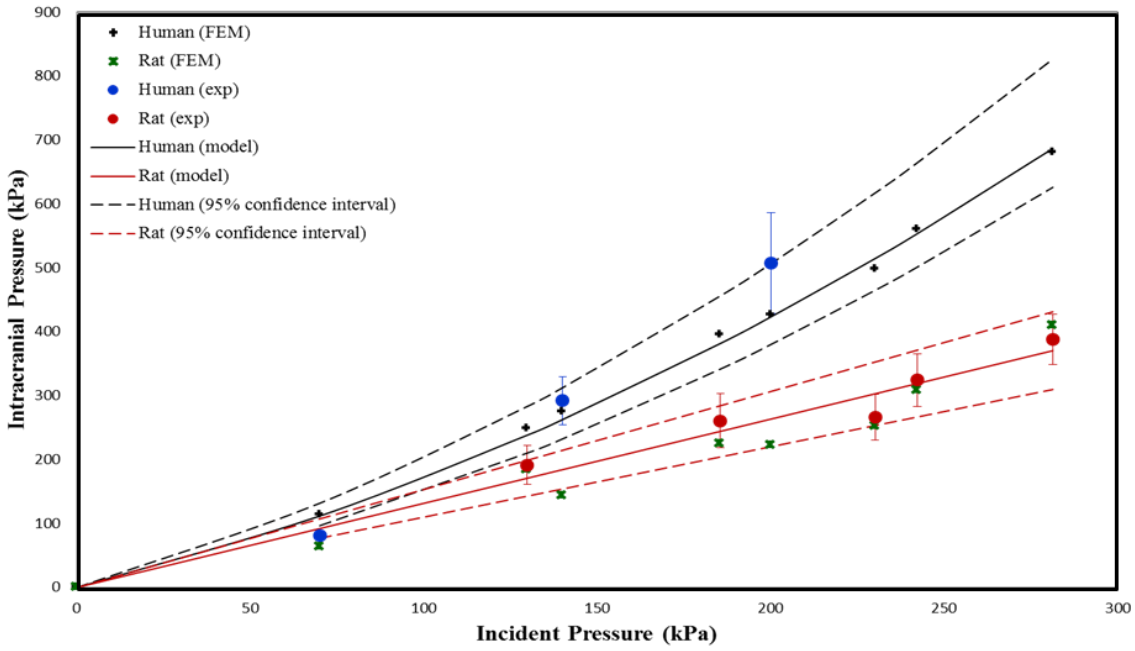

Figure 7.9: 2xQ nonlinear regression model to predict ICP for different incident pressures between 0-280 kPa.

The t test for coefficient yielded $t = 12.996$, $p < 0.001$, which means the coefficient makes a significant contribution to the model. The other predictor for the model is the nonlinear interaction term $incident^2$ *x animal type (animal type: human = 1 and animal = 0)* has a regression b_4 weight (unstandardized coefficient) of 0.004, i.e., with 1 kPa increase in incident pressure the slope of *ICP* increases by 0.004. The standardized coefficient beta ($-1<\beta<1$) 0.560 gives the contribution of the particular variable to the model. The t test for coefficient yielded $t = 12.388$, $p < 0.001$, which means the coefficient makes a significant contribution to the model. Finally, the constant gives the value of the ICP when all the predictors are zero. The t test for coefficient yielded $t = -0.607$, $p = 0.56$, which means constant does not make a significant contribution to the model, i.e., ICP is zero for zero

incident pressure. Figure 7.9 shows the plot from nonlinear regression model for predicting ICP for incident pressures between 0-280 kPa. The model also includes the experimental and finite element model data along with the 95 % for ICPs calculated through the regression model.

7.4. Discussion

Experiments using animals especially rats remain the foremost means to investigate biomechanics, biochemical and behavioral disorders due to BINT. The objective is to utilize the findings from the animals and apply it on the diagnostics, prognostics, and therapeutics of BINT for humans. Recently, research done on the animal models has shown that increase in blast pressure increases the intensity of injury to the brain. Furthermore, relationships have also been established between incident pressures and biological outcomes using animals [4, 133]. Although, the injury to the brain is a function of tissue level loading that is the intracranial pressure (ICP), species that are exposed to similar incident pressures have a significantly different ICP [134]. Therefore, incident pressure corresponding to injury for a particular species cannot be directly translated.

For the sake of this study, it was postulated that brain injury and the subsequent sequelae from blast exposure is due to the tissue level loading, i.e., ICP seen by the brain tissue/cell during blast. Furthermore, it is assumed that the injury threshold of tissue/cell of the brain across species is same. In the first part study, parametric analysis with simple ellipsoidal model was performed to study: (i) effect of skull thickness, (ii) effect shape and (iii) effect of cross sectional area. Consequently, proving scaling of injury across species for TBI

depends on variables other than just the mass of the species. In the second part of the study, a nonlinear regression model to determine the ICP for rats and humans from incident pressure is proposed. The consequence of this would be twofold: (i) ability to translate the biological outcome from the rat model to the human model, i.e., the intensity of the critical incident pressures that cause injury in the rat can be translated to humans, (ii) With the incident pressures known the corresponding ICPs can be determined in live animal testing to relate the biological outcomes.

For the parametric study, a theoretical model of a blast wave interacting with an ellipsoidal model (hollow ellipsoidal skull containing the brain) was developed. From the previous research by Kuppuswamy and his colleagues, it was shown that, the loading at any given point in the brain is a function of two separable parts as direct (longitudinal component or direct transmission) loading (P_d) and indirect (flexural component) loading (P_{id}) components given by $P=P_d+P_{id}$ (7.2) [135]. Direct transmission of blast waves further depends on the intensity of blast load (i.e., incident pressure) and the acoustic impedance mismatch between the skull-brain interfaces. The amount of pressure due to transmission (σ_t) is given by the eqn 7.3, $\sigma_t = \sigma_i \left(\frac{2Z_1}{Z_1+Z_2}\right)$ (7.3), where $Z_1=\rho_1 C_1$ and $Z_2=\rho_2 C_2$ are the impedance of the skull and brain respectively. σ_i, σ_t are the intensity of the incident pressure and transmitted pressure respectively and ρ and $C^2=E/\rho$ are the density and acoustic velocity of the medium. Apart from direct transmission, pressure on the skull causes flexural wave that travels through the circumference of the skull. This causes displacement of the skull causing localized loads on the brain, which is the indirect component of the

loading. The amplitude and frequency of the wave depends on the cross sectional geometry (second moment of area) and stiffness (young's modulus).

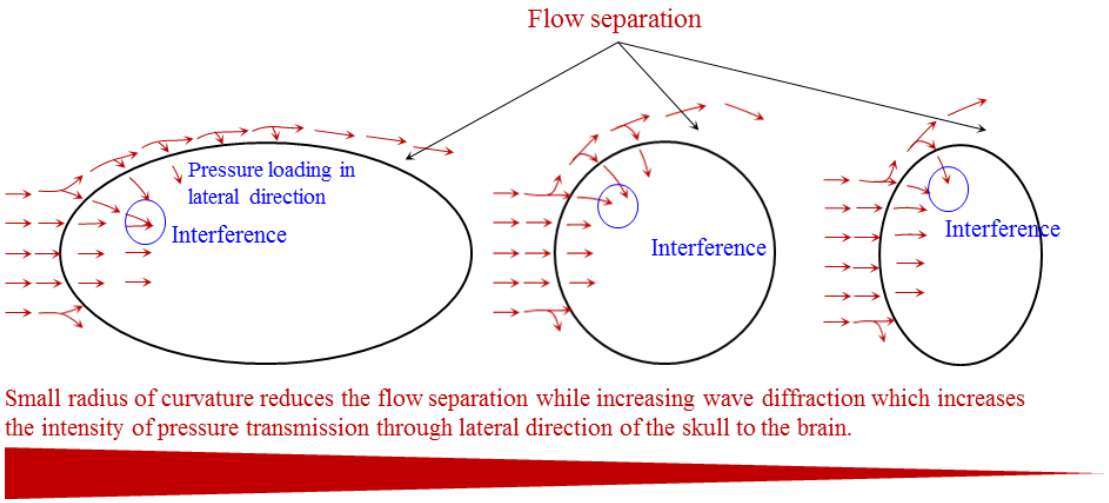

Figure 7.10: Pictorial representation of the flow-field for different shapes depicting the effect of the radius of curvature; furthermore, ellipsoidal model has a higher surface area of exposure compared to the other two geometries.

It was observed that with increase in the skull thickness pressure measured in the brain decreases. Although, the impedance mismatch in all the cases remains same, peak pressure in the brain for 8 mm thick skull is significantly lesser than the 0.2 mm case.

As discussed earlier, when the skull is subjected to blast loading, there is a direct transmission of stress followed by the indirect loading due to flexure. While the direct load is determined by the impedance mismatch, the indirect loading is determined by the flexural response of skull. For the same skull size, an increase in thickness leads to increase in the area moment of inertia, and hence lower amplitude and wavelength of deflection.

Consequently, the indirect loading reduces and hence the ICP. For the given head size and shape, beyond 2 mm skull thickness most of the pressure transmission from indirect loading is eliminated. Similarly, with increase in the modulus the intensity of the ICP reduces, which was shown through rat model in chapter 6 (section 6.3.2).

The next variable that was studied is the effect of radius of curvature on the ICP with constant skull thickness. Figure 7.10 shows the representation flow field on different geometries. A reduction in the pressure with reduction in the major axis of the ellipse was observed. This is due to two reasons: (i) with increase in the radius of curvature the flow separation increases reducing the lateral loading (from top), i.e., having more flat surface decreases the pressure loading in the top whereas having curvature increases the loading from the top, (ii) the interaction between two compressive waves from top and front results in a constructive interference resulting in higher ICP. Similar findings were observed during the numerical simulation of rat head where the blast wave after impinging on the snout diffracts and loads near eye socket and between bregma and lamba of the skull. Furthermore, the intensification of pressure due interference of waves was also observed during that study.

Similarly, experiments done on the rats by Bolander and his collegues showed higher principle strains on the skull between bregma and lambda. Experiments done on cylinder show that when the blast wave approaches the cylinder (circular cross section), the entire front half is engulfed in blast loading once the blast wave traverses halfway point flow separation is initiated, which eventually reduces ICP [135].

The next variable studied was the effect of the cross sectional area exposed to blast and its influence on the ICP. At a constant skull thickness of 2 mm, with increase in the area, there is a logarithmic (nonlinear) increase in the ICP measured in the brain. This is because increase in the size of the head increases the interaction time of the blast with the head. According to Bolander, for blasts with similar Mach number, a rat skull that is 45 mm long interacts with the blast wave for 92 μs, whereas a human skull that is 180 mm long interacts with the blast wave for 367 μs. This is further proven through the ICP measured on the rat and PHMS experiments in our study, where for a 150 kPa incident pressure rat and PMHS had 190 and 300 kPa respectively.

The results of the parametric studies showed that interaction of the blast with the different structures is a complex phenomenon. Furthermore, experiments done on rat and PMHS showed that there is significant variation in the ICP for a similar incident pressure applied. Consequently, neurochemical and histological studies along with the injury threshold development done on the animal (rats) may not apply to humans directly. Consequently, it is vital to develop a model that can be used for translating the results of the animals to human. Experiments were done on both rat and PMHS model to measure ICP for different incident pressures. A nonlinear regression model was developed to predict ICP for various incident pressures (between 0 to 280 kPa) for rat and humans. Model also has a 95% confidence interval curves for both rat and PMHS. It is interesting to note that the ICP for rat and PMHS is similar for incident pressures up to 70 kPa and beyond that, the ICP for PMHS becomes more nonlinear.

Although variables such as skull thickness cross sectional area and shape influence the ICP of the species, they were not included as predictor variables for the model. Since there were only two species in the model (humans and animals) effects of all these variables are included as a qualitative binary coded variable (PMHS = 1 and rat = 0). This step reduces the complexity and enhances the accuracy of the model. The model was further tested with the experimental ICP results of PMHS by Bolander (Figure 7.11). The data was acquired by exposing a front facing PMHS head to blast wave and the pressure was measured in the frontal cortex close to skull (similar to the current experimental model). From the results, it can be seen that model predicts ICP with fair accuracy. Furthermore, all the experimental data points lie within the 95% confidence interval.

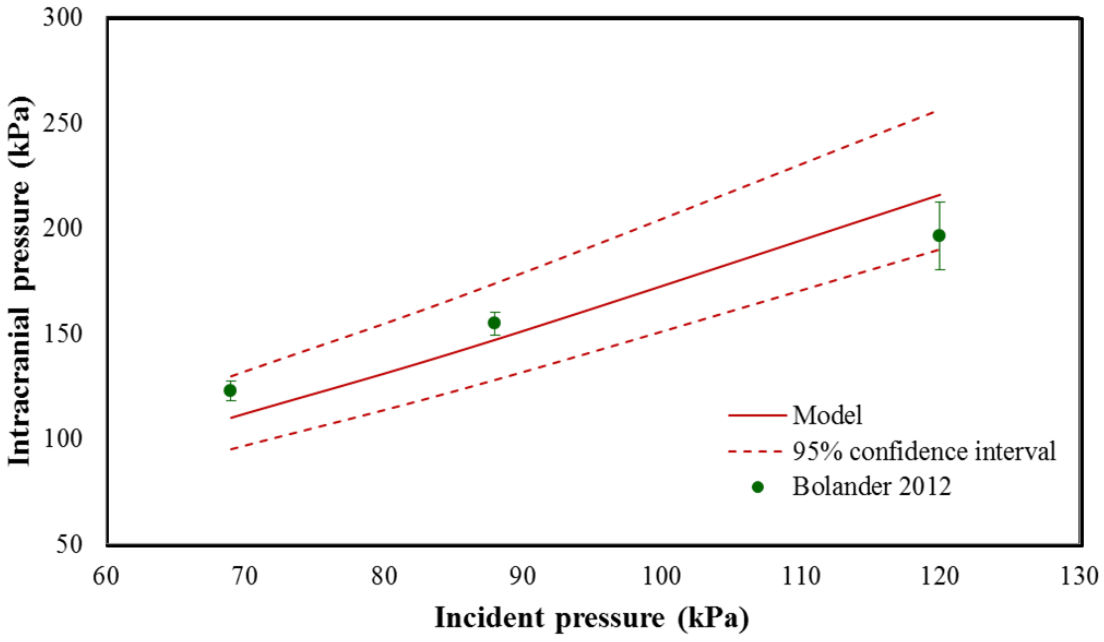

Figure 7.11: Comparison of the frontal cortex ICP between the model and Bolandar 2012 PMHS data.

Finally, if the injury to the brain is assumed to be a function of the tissue level loading experienced by any given species. Following method shows how model developed in this study can be used for translating the incident pressures corresponding to injury from rat experimental model. An experimental study was done by Abdul-Muneer and his colleagues to investigate the oxidative damage to the perivascular components of the brain due to blast impingement. From the study, it was determined that rats exposed to incident pressure of 123 kPa resulted in the disruption of the perivascular components resulting in neuroinflammation and neurotrauma to rats, which caused blood brain barrier (BBB) damage. However, rats recovered from this injury; authors suggested that repeated exposure at this intensity level might cause permanent damage to the brain.

Based on our predictive model proposed in Equation 7.2, an incident pressure of 123 kPa will lead to an ICP of 165 kPa in rats.

$$ICP = 1.318.(IP) + 0.004.(IP)^2.(z) \qquad (7.4)$$

$$0.004.(IP)^2.(z) + 1.318.(IP) - ICP = 0 \qquad (7.5)$$

While equation 7.2 predicts *ICP* for either a rat (*z=0*) or human (*z=1*), Eqn. 7.4 can be used to predict an incident pressure given an *ICP*. Consequently, for the same *ICP* (i.e., 165 kPa *ICP*), human should be exposed to an incident overpressure of 97 kPa, as per Eqn. 7.5.

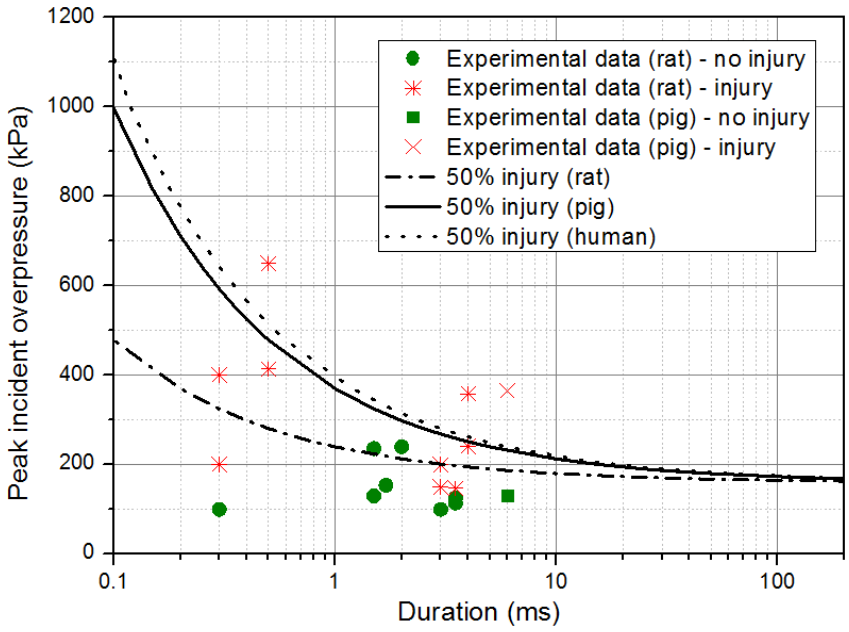

Figure 7.12: Scaling the 50% injury curve from the rat to the pig and human. The experimental data for the rat and pig are also included for comparison purpose (Figure from [85]).

It is interesting to note while rats are not injured at 123 kPa, humans may be injured and this is due the size and shape effect despite the fact that human skull is thicker than that of rat (as shown through the numerical study done earlier in this chapter). This is counter-intuitive to some of the published work based on scaling models with mass as the criterion.

Figure 7.12 shows the latest injury threshold model developed using mass as a scaling variable by Zhu and his colleagues. On the contrary to the predictions of the model in this work, using mass as a scaling variable predicts higher incident pressures for humans than rats (incident pressure within 1 to 10ms are usually seen in theater). Consequently, developing protective equipment or therapies based on this data can lead to fatal outcomes.

Some of the limitations of the model are as follows: (i) since the model is based on the data collected from the frontal cortex near forehead (close to skull), it does not account for the ICP in the other parts of the brain, which may vary significantly; however, the ICP measured in the frontal cortex had the maximum values [117], (ii) range of the model is within 0 to 280 kPa, (iii) experiments for humans head were done using PMHS, therefore, freezing/thawing, tissue disruption and rigor mortise affects the accuracy of the results, (iv) only limited number data points were used in the model, therefore, adding more data points would definitely increase the accuracy and range of applicability of the model, (v) In this study only the overpressure of the ICP profile is scaled time duration, which is also an important parameter is not included (vi) ICP is considered as the key determinant variable for injury; however other critical parameters like pressure duration (or impulse), local stress, strain, or energy density may also influence the injury severity.

7.5. Summary

A nonlinear regression model was developed to predict and relate the intracranial pressure (ICP) of rat and human head. Experimental as well as finite element model of rat head and human head were used to obtain the data points. With these data points as input, a nonlinear regression model was developed with incident pressure (quantitative) and specimen type (qualitative) as predictor variable and ICP as criterion variable. Model was validated with ICP measurements on PMHS head model. There was good agreement in the predicted ICP to the experimental data. Subsequently, model was applied to predict the incident pressure

for blood brain barrier (BBB) rupture by translating the corresponding incident pressure from rat model. Some of the key findings from this chapter are as follows:

- Geometry of the head plays a major role when interacting with the blast wave resulting varying ICPs for various species.
- ICP at higher incident pressure become nonlinear for PMHS whereas remains linear for rat model.
- Incident pressure corresponding to injury (as measured by ICP) in humans is less compared to rat; consequently, this makes humans more vulnerable to blast for the same incident pressure.
- Using mass as a scaling variable leads to erroneous predictions of incident pressure.

CHAPTER 8: CONCLUSION AND FUTURE WORK

8.1 Conclusions of this work:

Due to the increasing acts of terror as well as the asymmetric warfare encountered in theater, blast-induced neurotrauma (BINT) has become more prevalent. Exhaustive research efforts have been initiated recently to encounter this problem. Although, some progress has been made, much more work has to be done to increase the understanding of BINT. Currently, a lot of research is conducted to study the biological consequences of BINT using animal model (especially rat). However, due to the varying mechanical and biological variables across species as well as nonstandard methods used for replicating field blast, it is impossible to translate any biological outcomes from animal model experiment to humans or to use the results in designing effective mitigation strategies. In this work, a standardized method for producing blast wave conditions (related to field conditions) pertaining to primary blast injury is proposed. Furthermore, this knowledge along with numerical methods is used to study blast wave head interactions on rat model. Finally, a nonlinear regression model was developed to translate the incident pressure corresponding to injury from animal model to humans. Some of the contributions of this work are:

- It was shown that shock tube could be effectively controlled to produce blast wave profiles that are comparable to field explosion testing.

- The results from the field experiments and shock tube were compared to show that blast wave produced in the shock tube interacts with a surrogate in a similar manner seen in the field experiments.
- Experimental and numerical rat models were developed to study the blast wave interaction, intracranial pressure and skull flexure.
- A nonlinear regression model to translate the incident pressure between rat and humans was developed. With this model, the critical thresholds developed in rat model can be translated to humans. Furthermore, the thresholds deduced from the model can be used in developing personal protective equipment.

8.2 Recommendations for the future work:

Recommendations are given based on the chapters. Some of the recommendations for the future work are:

- In the third chapter, only the positive phase of the blast wave was modeled in shock tube and all the analysis to control and manipulate shock tube were done only on the positive phase of the shock tube; however, the negative phase is also important and needs to be studied. It is hypothesized that negative phase or negative overpressure may be responsible for cavitation in the brain, which is an important injury mechanism that has to be studied.
- In the fourth chapter, where a comparison between field and shock tube experiments were made, a lot more field experiments have to be done to reduce the type II error in the peak comparison of acceleration and overpressures. Furthermore, analysis to

determine the high acceleration in shock tube compared to field experiments has to be made. Finally, it should be determined whether these acceleration values affect the overall experimentation.

- In the fifth and sixth chapter, only intracranial pressure and direct transmission were studied; however, other mechanisms such as cavitation, thoracic surge and injuries due to acceleration and deceleration has to be studied to have comprehensive understanding of the blast.
- In the final chapter, the number of data points used in the model should be increased. Furthermore, other species such as pig and mice should also be included to obtain a comprehensive model. Finally, limitations mentioned at the end of the chapter should be addressed.

REFERENCES

1. Bhattacharjee, Y., *Shell Shock Revisited: Solving the Puzzle of Blast Trauma.* Science, 2008. **319**(5862): p. 406-408.

2. Wolf, S.J., et al., *Blast injuries.* The Lancet, 2009. **374**(9687): p. 405-415.

3. Ackerman, S., *Global terrorism rose 43% in 2013 despite al-Qaida splintering, US reports,* in *theguardian*. 2014, theguardian.com: New York.

4. Cernak, I., et al., *The pathobiology of blast injuries and blast-induced neurotrauma as identified using a new experimental model of injury in mice.* Neurobiology of disease, 2011. **41**(2): p. 538-551.

5. Cho, H.J., et al., *Potential role of pro-oxidative and pro-inflammatory mechanisms in blast-induced neurotrauma.* The FASEB Journal, 2013. **2013**(27).

6. Risling, M. and J. Davidsson, *Experimental animal models for studies on the mechanisms of blast-induced neurotrauma.* Frontiers in neurology, 2012. **3**.

7. Anderson, R.J., *Shell shock: an old injury with new weapons.* Molecular interventions, 2008. **8**(5): p. 204.

8. Zoroya, G. *360,000 veterans may have brain injuries*. 2009; Available from: http://usatoday30.usatoday.com/news/military/2009-03-04-braininjuries_N.htm.

9. Tanielian, T., and Jaycox, L.H., *Invisible wounds of war*. 2008, Santa Monica, CA: RAND Corporation.

10. DePalma, R.G., et al., *Blast Injuries.* New England Journal of Medicine, 2005. **352**(13): p. 1335-1342.

11. Moore, D.F., et al., *Computational biology - Modeling of primary blast effects on the central nervous system.* Neuroimage, 2009. **47**: p. T10-T20.

12. Moore, D.F., et al., *Blast physics and central nervous system injury.* Future Neurology, 2008. **3**(3): p. 243-250.

13. Belmont, P., A.J. Schoenfeld, and G. Goodman, *Epidemiology of combat wounds in Operation Iraqi Freedom and Operation Enduring Freedom: orthopaedic burden of disease.* J Surg Orthop Adv, 2010. **19**(1): p. 2-7.

14. Schwartz, R.B., R.W. Sattin, and R.C. Hunt, *Medical Response to Bombings: The Application of Lessons Learned to a Tragedy.* Disaster Medicine and Public Health Preparedness, 2013. **7**(02): p. 114-115.

15. Biddinger, P.D., et al., *Be prepared—the Boston Marathon and mass-casualty events.* New England journal of medicine, 2013. **368**(21): p. 1958-1960.

16. Wilson, C. *Improvised explosive devices (IEDs) in Iraq and Afghanistan: effects and countermeasures*. 2006. DTIC Document.

17. Baker, D. and V. Murray, *Emergency medical and public health responses to the 2005 London bombings.* Integrated Emergency Management for Mass Casualty Emergencies: Proceedings of the NATO Advanced Training Course on Integrated Emergency Management for Mass Casualty Emergencies Organized by CESPRO, University of Florence, Italy, 2013. **113**: p. 74.

18. Reneer, D.V., et al., *A Multi-Mode Shock Tube for Investigation of Blast-Induced Traumatic Brain Injury.* Journal of Neurotrauma, 2011. **28**(1): p. 95-104.

19. Terrio, H., et al., *Traumatic Brain Injury Screening: Preliminary Findings in a US Army Brigade Combat Team.* Journal of Head Trauma Rehabilitation, 2009. **24**(1): p. 14-23.

20. Zhu, F., et al., *Development of an FE model of the rat head subjected to air shock loading.* Stapp car crash journal, 2010. **54**: p. 211-25.

21. *Operation Iraqi Freedom (OIF)/Operation Enduring Freedom (OEF) Fact Sheet.* Defense and Veterans Brain Injury Center February 2007.

22. Sundaramurthy, A., et al., *Blast-Induced Biomechanical Loading of the Rat: An Experimental and Anatomically Accurate Computational Blast Injury Model.* Journal of Neurotrauma, 2012. **29**(13): p. 2352-2364.

23. Warden, D., *Military TBI During the Iraq and Afghanistan Wars.* The Journal of Head Trauma Rehabilitation, 2006. **21**(5): p. 398-402.

24. N.Kleinschmit, *A shock tube technique for blast wave simulation and studies of flow structure interactions in shock tube blast experiments [Master's thesis]*, in *Engineering Mechanics*. 2011, University of Nebraska Lincoln: Lincoln.

25. AEP-55., N.A.T.O., *Procedures for evaluating the protection level of logistic and light armoured vehicle: for mine threat. (Volume 2),*. 2006.

26. Terrio, H., et al., *Traumatic brain injury screening: preliminary findings in a US Army Brigade Combat Team.* The Journal of head trauma rehabilitation, 2009. **24**(1): p. 14-23.

27. Jones, E., N.T. Fear, and S. Wessely, *Shell shock and mild traumatic brain injury: A historical review.* American Journal of Psychiatry, 2007. **164**(11): p. 1641-1645.

28. Baum, F., K. Stanyukovich, and B.I. Shekhter, *Physics of an Explosion*. 1959, DTIC Document.

29. Kinney, G.F. and K.J. Graham, *Explosive shocks in air*. 1985, New York: Springer-Verlag.

30. Ritzel, D. and K. Matthews. *An adjustable explosion-source model for CFD blast calculations*. in *Proc. of 21st International Symposium on Shock Waves*. 1997.

31. Ritzel, D., et al. *Experimental blast simulation for injury studies*. in *Proc. HFM-207 NATO Symposium on a Survey of Blast Injury Across the Full Landscape of Military Science*. 2011.

32. Kobeissy, F.H., et al., *Assessing Neuro-Systemic & Behavioral Components in the Pathophysiology of Blast-Related Brain Injury.* Frontiers in Neurology, 2013. **4**.

33. Abdul-Muneer, P.M., et al., *Induction of oxidative and nitrosative damage leads to cerebrovascular inflammation in an animal model of mild traumatic brain injury induced by primary blast.* Free Radical Biology and Medicine, 2013. **60**(0): p. 282-291.

34. Ahmed, F.A., et al., *Long-term consequences of single and multiple mild blast exposure on select physiological parameters and blood-based biomarkers.* Electrophoresis, 2013. **34**(15): p. 2229-2233.

35. Arun, P., et al., *Distinct patterns of expression of traumatic brain injury biomarkers after blast exposure: role of compromised cell membrane integrity.* Neuroscience letters, 2013. **552**: p. 87-91.

36. Ahlers, S.T., et al., *Assessment of the effects of acute and repeated exposure to blast overpressure in rodents: toward a greater understanding of blast and the potential ramifications for injury in humans exposed to blast.* Frontiers in neurology, 2012. **3**: p. 32.

37. Prima, V., et al., *Impact of Moderate Blast Exposures on Thrombin Biomarkers Assessed by Calibrated Automated Thrombography in Rats.* Journal of neurotrauma, 2013. **30**(22): p. 1881-1887.

38. Tümer, N., et al., *Overpressure blast-wave induced brain injury elevates oxidative stress in the hypothalamus and catecholamine biosynthesis in the rat adrenal medulla.* Neuroscience letters, 2013. **544**: p. 62-67.

39. Huber, B.R., et al., *Blast exposure causes early and persistent aberrant phospho- and cleaved-tau expression in a murine model of mild blast-induced traumatic brain injury.* Journal of Alzheimer's disease, 2013. **37**(2): p. 309-323.

40. Skotak, M., et al., *Rat injury model under controlled field-relevant primary blast conditions: acute response to a wide range of peak overpressures.* Journal of neurotrauma, 2013. **30**(13): p. 1147-1160.

41. Valiyaveettil, M., et al., *Contribution of systemic factors in the pathophysiology of repeated blast-induced neurotrauma.* Neuroscience letters, 2013. **539**: p. 1-6.

42. Turner, R.C., et al., *Modeling clinically relevant blast parameters based on scaling principles produces functional & histological deficits in rats.* Experimental neurology, 2013. **248**: p. 520-529.

43. Cho, H.J., et al., *Blast induces oxidative stress, inflammation, neuronal loss and subsequent short-term memory impairment in rats.* Neuroscience, 2013. **253**(0): p. 9-20.

44. Balakathiresan, N., et al., *MicroRNA let-7i is a promising serum biomarker for blast-induced traumatic brain injury.* Journal of neurotrauma, 2012. **29**(7): p. 1379-1387.

45. Bir, C., et al., *Effects of variable blast pressures on blood flow and oxygen saturation in rat brain as evidenced using MRI.* Magnetic Resonance Imaging, 2012. **30**(4): p. 527-534.

46. Kovesdi, E., et al., *Acute minocycline treatment mitigates the symptoms of mild blast-induced traumatic brain injury.* Frontiers in neurology, 2012. **3**.

47. Rafaels, K.A., et al., *Brain injury risk from primary blast.* Journal of trauma and acute care surgery, 2012. **73**(4): p. 895-901.

48. Shridharani, J.K., et al., *Porcine head response to blast.* Frontiers in neurology, 2012. **3**.

49. Elder, G.A., et al., *Blast exposure induces post-traumatic stress disorder-related traits in a rat model of mild traumatic brain injury.* Journal of neurotrauma, 2012. **29**(16): p. 2564-2575.

50. Dalle Lucca, J.J., et al., *Blast-induced moderate neurotrauma (BINT) elicits early complement activation and tumor necrosis factor alpha (TNFα) release in a rat brain.* Journal of the neurological sciences, 2012. **318**(1): p. 146-154.

51. Arun, P., et al., *Studies on blast traumatic brain injury using in-vitro model with shock tube.* Neuroreport, 2011. **22**(8): p. 379-384.

52. Chavko, M., et al., *Relationship between orientation to a blast and pressure wave propagation inside the rat brain.* Journal of Neuroscience Methods, 2011. **195**(1): p. 61-66.

53. Koliatsos, V.E., et al., *A mouse model of blast injury to brain: initial pathological, neuropathological, and behavioral characterization.* Journal of Neuropathology & Experimental Neurology, 2011. **70**(5): p. 399-416.

54. Cernak, I., et al., *Ultrastructural and functional characteristics of blast injury-induced neurotrauma.* Journal of Trauma-Injury, Infection, and Critical Care, 2001. **50**(4): p. 695-706.

55. Risling, M., et al., *Mechanisms of blast induced brain injuries, experimental studies in rats.* NeuroImage, 2011. **54, Supplement 1**(0): p. S89-S97.

56. Connell, S., et al., *Novel model to investigate blast injury in the central nervous system.* Journal of neurotrauma, 2011. **28**(7): p. 1229-1236.

57. Garman, R.H., et al., *Blast exposure in rats with body shielding is characterized primarily by diffuse axonal injury.* Journal of neurotrauma, 2011. **28**(6): p. 947-959.

58. Gyorgy, A., et al., *Time-dependent changes in serum biomarker levels after blast traumatic brain injury.* Journal of neurotrauma, 2011. **28**(6): p. 1121-1126.

59. Readnower, R.D., et al., *Increase in blood–brain barrier permeability, oxidative stress, and activated microglia in a rat model of blast-induced traumatic brain injury.* Journal of neuroscience research, 2010. **88**(16): p. 3530-3539.

60. Long, J.B., et al., *Blast Overpressure in Rats: Recreating a Battlefield Injury in the Laboratory.* Journal of Neurotrauma, 2009. **26**(6): p. 827-840.

61. Saljo, A., et al., *Low-Level Blast Raises Intracranial Pressure and Impairs Cognitive Function in Rats: Prophylaxis with Processed Cereal Feed.* Journal of Neurotrauma, 2010. **27**(2): p. 383-389.

62. Cernak, *Animal Models of Head Trauma.* NeuroRX, 2005. **2**(3): p. 410-422.

63. Chavko, M., et al., *Measurement of blast wave by a miniature fiber optic pressure transducer in the rat brain.* Journal of Neuroscience Methods, 2007. **159**(2): p. 277-281.

64. Leonardi, A.D.C., et al., *Intracranial Pressure Increases during Exposure to a Shock Wave.* Journal of Neurotrauma, 2011. **28**(1): p. 85-94.

65. Bolander, R., et al., *Skull Flexure as a Contributing Factor in the Mechanism of Injury in the Rat when Exposed to a Shock Wave.* Annals of Biomedical Engineering, 2011: p. 1-10.

66. Skotak M, et al., *Rat injury model under controlled field-relevant primary blast conditions: Acute response to a wide range of peak overpressures.* J Neurotrauma., 2013. **Epub ahead of print**.

67. Leonardi, A.D.C., et al., *Methodology and Evaluation of Intracranial Pressure Response in Rats Exposed to Complex Shock Waves.* Annals of biomedical engineering, 2013. **41**(12): p. 2488-2500.

68. Ward, C., P. Nikravesh, and R. Thompson, *Biodynamic finite element models used in brain injury research.* Aviation, space, and environmental medicine, 1978. **49**(1 Pt. 2): p. 136-142.

69. Ward, C., M. Chan, and A. Nahum, *INTRACRANIAL PRESSURE--A BRAIN INJURY CRITERION*. 1980.

70. Gennarelli, T.A., et al., *Diffuse axonal injury and traumatic coma in the primate.* Annals of neurology, 1982. **12**(6): p. 564-574.

71. Lee, M.-C., J.W. Melvin, and K. Ueno, *Finite element analysis of traumatic subdural hematoma*. 1987, SAE Technical Paper.

72. Mendis, K., *Finite Element Modeling of the Brain to Establish Diffuse Axonal Injury Criteria*, in *Mechanical Engineering*. 1992, The Ohio State University.

73. Zhou, C., T.B. Khalil, and A.I. King. *Shear stress distribution in the porcine brain due to rotational impact*. in *SAE PUBLICATION P-279. PROCEEDINGS OF THE 38TH STAPP CAR CRASH CONFERENCE, OCTOBER 31-NOVEMBER 4, 1994, FORT LAUDERDALE, FLORIDA, USA (SAE TECHNICAL PAPER 942214)*. 1994.

74. Peña, A., et al., *Brain tissue biomechanics in cortical contusion injury: a finite element analysis.* Acta Neurochir. Suppl, 2005. **95**: p. 333-336.

75. Levchakov, A., et al., *Computational studies of strain exposures in neonate and mature rat brains during closed head impact.* Journal of neurotrauma, 2006. **23**(10): p. 1570-1580.

76. Mao, H., et al., *Application of a finite element model of the brain to study traumatic brain injury mechanisms in the rat.* Stapp car crash journal, 2006. **50**: p. 583-600.

77. Mao, H., et al., *Finite element analysis of controlled cortical impact-induced cell loss.* Journal of neurotrauma, 2010. **27**(5): p. 877-888.

78. Mao, H., et al., *Computational neurotrauma—design, simulation, and analysis of controlled cortical impact model.* Biomechanics and modeling in mechanobiology, 2010. **9**(6): p. 763-772.

79. Richmond, D., et al., *Shock tube studies of the effects of sharp-rising, long-duration overpressures on biological systems*. 1959, DTIC Document.

80. Bowen, I.G., et al., *A fluid-mechanical model of the thoraco-abdominal system with applications to blast biology*. 1965, DTIC Document.

81. Bass, C.R., K.A. Rafaels, and R.S. Salzar, *Pulmonary injury risk assessment for short-duration blasts.* Journal of Trauma-Injury, Infection, and Critical Care, 2008. **65**(3): p. 604-615.

82. Gruss, E., *A correction for primary blast injury criteria.* Journal of Trauma-Injury, Infection, and Critical Care, 2006. **60**(6): p. 1284-1289.

83. Rafaels, K.A., et al., *Pulmonary injury risk assessment for long-duration blasts: a meta-analysis.* Journal of Trauma-Injury, Infection, and Critical Care, 2010. **69**(2): p. 368-374.

84. Panzer, M.B., et al., *Primary blast survival and injury risk assessment for repeated blast exposures.* The journal of trauma and acute care surgery, 2012. **72(**2): p. 454-466.

85. Zhu, F., et al., *SOME CONSIDERATIONS ON THE THRESHOLD AND INTER-SPECIES SCALING LAW FOR PRIMARY BLAST-INDUCED TRAUMATIC BRAIN INJURY: A SEMI-ANALYTICAL APPROACH.* Journal of Mechanics in Medicine and Biology, 2013. **13**(04).

86. Ommaya, A.K., et al., *Scaling of experimental data on cerebral concussion in sub-human primates to concussion threshold for man*. 1967, DTIC Document.

87. Ommaya, A. and A. Hirsch, *Tolerances for cerebral concussion from head impact and whiplash in primates.* Journal of biomechanics, 1971. **4**(1): p. 13-21.

88. Margulies, S.S. and L.E. Thibault, *A proposed tolerance criterion for diffuse axonal injury in man.* Journal of biomechanics, 1992. **25**(8): p. 917-923.

89. Gibson, L., *Woodpecker pecking: how woodpeckers avoid brain injury.* Journal of Zoology, 2006. **270**(3): p. 462-465.

90. Stalnaker, R., V. Roberts, and J.H. McElhaney. *Side impact tolerance to blunt trauma*. in *Proceedings: Stapp Car Crash Conference*. 1973. Society of Automotive Engineers SAE.

91. McElhaney, J.H., et al., *Door crashworthiness criteria.* Training, 1971. **2014**: p. 04-07.

92. Ono, K., et al., *Human head tolerance to sagittal impact. Reliable estimation deduced from experimental head injury using subhuman primates and human cadaver skulls*. 1980.

93. Zhang, L., K.H. Yang, and A.I. King, *A proposed injury threshold for mild traumatic brain injury.* Journal of biomechanical engineering, 2004. **126**(2): p. 226-236.

94. Rafaels, K., *Blast brain injury risk. (Doctoral dissertation)*. 2010, University of Virginia.

95. Svetlov, S.I., et al., *Morphologic and Biochemical Characterization of Brain Injury in a Model of Controlled Blast Overpressure Exposure.* The Journal of Trauma, 2010. **69**(4): p. 795-804 10.1097/TA.0b013e3181bbd885.

96. Chandra, N., A. Holmberg, and R. Feng, *Controlling the shape of the shock wave profile in a blast facility*, U.S.P. patent, Editor. 2011.

97. Kleinschmit, N.N., *A shock tube technique for blast wave simulation and studies of flow structure interactions in shock tube blast experiments (Masters Thesis),* in *Engineering Mechanics*. 2011, University of Nebraska Lincoln.

98. Skotak, M., et al., *Rat injury model under controlled field-relevant primary blast conditions: Acute response to a wide range of peak overpressures.* Journal of Neurotrauma, 2013(in print).

99. Payman, W. and W.C.F. Shepherd, *Explosion Waves and Shock Waves. VI. The Disturbance Produced by Bursting Diaphragms with Compressed Air.* Proceedings of the Royal Society of London. Series A. Mathematical and Physical Sciences, 1946. **186**(1006): p. 293-321.

100. Bass, C.R., et al., *Brain injuries from blast.* Annals of Biomedical Engineering, 2012: p. 1-18.

101. Mott, D., et al., *Blast-Induced Pressure Fields Beneath a Military Helmet for Non-Lethal Threats.* Bulletin of the American Physical Society, 2008. **53**.

102. HSD, *Homeland security bomb threat chart, https://www.llis.dhs.gov/sites/default/files/DHS-BombThreatChart-6-5-09.pdf*.

103. Haselbacher, A., S. Balachandar, and S.W. Kieffer, *Open-ended shock tube flows: Influence of pressure ratio and diaphragm position.* AIAA Journal, 2007. **45**(8): p. 1917-1929.

104. Desmoulin, G.T. and J.-P. Dionne, *Blast-Induced Neurotrauma: Surrogate Use, Loading Mechanisms, and Cellular Responses.* The Journal of Trauma, 2009. **67**(5): p. 1113-1122 10.1097/TA.0b013e3181bb8e84.

105. Chang, K.S. and J.K. Kim, *Numerical Investigation of Inviscid Shock-Wave Dynamics in an Expansion Tube.* Shock Waves, 1995. **5**(1-2): p. 33-45.

106. Honma, H., et al., *Interferometric CT measurement of three-dimensional flow phenomena on shock waves and vortices discharged from open ends.* Shock Waves, 2003. **13**(3): p. 179-190.

107. Jiang, Z., O. Onodera, and K. Takayama, *Evolution of shock waves and the primary vortex loop discharged from a square cross-sectional tube.* Shock Waves, 1999. **9**(1): p. 1-10.

108. Jiang, Z., K. Takayama, and B.W. Skews, *Numerical study on blast flowfields induced by supersonic projectiles discharged from shock tubes.* Physics of Fluids, 1998. **10**(1): p. 277-288.

109. Ganpule, S., et al., *Role of helmet in the mechanics of shock wave propagation under blast loading conditions.* Computer Methods in Biomechanics and Biomedical Engineering, 2011: p. 1-12.

110. Anderson, J., *Fundamentals of aerodynamics*. 2001, New York: McGraw-Hill.

111. Ahlers, S.T., et al., *Assessment of the effects of acute and repeated exposure to blast overpressure in rodents: toward a greater understanding of blast and the potential ramifications for injury in humans exposed to blast.* Frontiers in Neurology, 2012. **3**.

112. Moore, D.F., et al., *Computational biology — Modeling of primary blast effects on the central nervous system.* NeuroImage, 2009. **47, Supplement 2**(0): p. T10-T20.

113. Willinger, R., H.-S. Kang, and B. Diaw, *Three-Dimensional Human Head Finite-Element Model Validation Against Two Experimental Impacts.* Annals of Biomedical Engineering, 1999. **27**(3): p. 403-410.

114. Stalnaker, R.L., *Mechanical properties of the head, Ph.D. Dissertation*. 1969, West Virginia University.

115. McElhaney, J., et al. *Dynamic characteristics of the tissues of the head*. in *In: Perspectives in Biomedical Engineering*. 1973.

116. Zhang, L.Y., K.H. Yang, and A.I. King, *Comparison of brain responses between frontal and lateral impacts by finite element modeling.* Journal of Neurotrauma, 2001. **18**(1): p. 21-30.

117. Ganpule, S.G., *Mechanics of blast loading on post-mortem human and surrogate heads in the study of Traumatic Brain Injury (TBI) using experimental and computational approaches.* 2013.

118. Jiang, Z., et al., *Three-dimensional propagation of the transmitted shock wave in a square cross-sectional chamber.* Shock Waves, 2003. **13**(2): p. 103-111.

119. Kashimura, H., et al., *Discharge of a shock wave from an open end of a tube.* Journal of Thermal Science, 2000. **9**(1): p. 30-36.

120. Project, T.V.H., *The Visible Human Project, National Library of Medicine*. 2009.

121. Bourdin, X., et al. *Comparison Of Tetrahedral And Hexahedral Meshes For Human Finite Element Modelling: An Application To Kidney Impact*. in *In: 20th Enhanced Safety of Vehicles Conference: Innovations for safety: opportunities and challenges*. 2007.

122. Baker, T.J., *Mesh generation: Art or science?* Progress in Aerospace Sciences, 2005. **41**(1): p. 29-63.

123. Schneiders, R. *Algorithms for quadrilateral and hexahedral mesh generation*. in *In Proceedings of the VKI Lecture Series on Computational Fluid Cynamics*. 2000.

124. Wieding, J., et al., *Finite Element Analysis of Osteosynthesis Screw Fixation in the Bone Stock: An Appropriate Method for Automatic Screw Modelling.* PLoS ONE, 2012. **7**(3): p. e33776.

125. Cifuentes, A.O. and A. Kalbag, *A performance study of tetrahedral and hexahedral elements in 3-D finite element structural analysis.* Finite Elements in Analysis and Design, 1992. **12**(3–4): p. 313-318.

126. Ramos, A. and J.A. Simões, *Tetrahedral versus hexahedral finite elements in numerical modelling of the proximal femur.* Medical Engineering & Physics, 2006. **28**(9): p. 916-924.

127. Chafi, M., G. Karami, and M. Ziejewski, *Biomechanical Assessment of Brain Dynamic Responses Due to Blast Pressure Waves.* Annals of Biomedical Engineering, 2010. **38**(2): p. 490-504.

128. Chen, Y. and M. Ostoja-Starzewski, *MRI-based finite element modeling of head trauma: spherically focusing shear waves.* Acta Mechanica, 2010. **213**(1-2): p. 155-167.

129. Grujicic, M., et al., *Fluid/Structure Interaction Computational Investigation of Blast-Wave Mitigation Efficacy of the Advanced Combat Helmet.* Journal of Materials Engineering and Performance, 2011. **20**(6): p. 877-893.

130. Moss, W.C., M.J. King, and E.G. Blackman, *Skull Flexure from Blast Waves: A Mechanism for Brain Injury with Implications for Helmet Design.* Physical Review Letters, 2009. **103**(10): p. 108702.

131. Nyein, M.K., et al., *In silico investigation of intracranial blast mitigation with relevance to military traumatic brain injury.* Proceedings of the National Academy of Sciences, 2010.

132. Shuck, L.Z. and S.H. Advani, *Rheological response of human brain-tissue in shear*. Journal of Basic Engineering, 1972. **94**(4): p. 905-911.

133. Reneer, D., et al., *Extent of Cerebrovascular Disruption Following Blast Exposure is Influenced by the Duration of the Positive Phase in Addition to Peak Overpressure.* J Neurol Neurophysiol, 2014. **5**: p. 188.

134. Bolander, R., *A multi-species analysis of biomechanical responses of the head to a shock wave.* 2012.

135. Kuppuswamy, V.S., *The Mechanics of Intracranial Loading During Blast and Blunt Impacts-Experimental and Numerical Studies* 2013.

APPENDIX – STATISTICAL ANALYSIS

Max pressure comparison (yes – significant difference/ no – not significantly different based on p value)

(I) Comparison between 28 in. short vs. Free field (bare)

Test (bare)	Average	Std.ev	F	p	Conclusion
28 in. short	81.64	4.86	**3.18**	**0.09**	**no**
FF	70.14	20.82			
28 in. short	58.37	2.66	**26.31**	**0.00**	**yes**
FF	41.07	10.86			
28 in. short	30.39	0.85	**192.02**	**0.00**	**yes**
FF	19.17	2.54			
28 in. short	17.09	1.63	**2.58**	**0.12**	**no**
FF	18.93	3.40			
28 in. short	35.90	1.31	**117.60**	**0.00**	**yes**
FF	22.75	3.77			
28 in. short	40.38	1.64	**11.74**	**0.00**	**yes**
FF	32.10	7.85			
28 in. short	25.78	0.66	**19.73**	**0.00**	**yes**
FF	20.91	3.58			
28 in. short	30.73	2.73	**143.85**	**0.00**	**yes**
FF	17.14	2.43			

28 in. short	40.28	1.36	**6.59**	**0.02**	**yes**
FF	34.25	7.67			
28 in. short	27.66	1.05	**34.03**	**0.00**	**yes**
FF	20.12	4.15			
28 in. short	20.39	4.44	**1.11**	**0.31**	**no**
FF	22.51	4.54			

(II) Comparison between 28 in. short vs. Free field (Helmet)

Test (Bare)	**Average**	**Stdev**	**F**	**p**	**Conclusion**
28 in. short	81.64	4.86	**189.07**	**0.00**	**yes**
FF	117.98	3.20			
28 in. short	58.37	2.66	**167.33**	**0.00**	**yes**
FF	76.77	1.49			
28 in. short	30.39	0.85	**86.23**	**0.00**	**yes**
FF	24.80	1.47			
28 in. short	17.09	1.63	**0.16**	**0.70**	**no**
FF	17.45	1.24			
28 in. short	35.90	1.31	**642.74**	**0.00**	**yes**
FF	17.11	1.13			
28 in. short	40.38	1.64	**270.17**	**0.00**	**yes**
FF	55.24	1.20			

28 in. short	25.78	0.66	**125.10**	**0.00**	**yes**
FF	30.48	0.90			
28 in. short	30.73	2.73	**153.73**	**0.00**	**yes**
FF	13.33	0.35			
28 in. short	40.28	1.36	**342.89**	**0.00**	**yes**
FF	54.80	1.29			
28 in. short	27.66	1.05	**1.26**	**0.28**	**no**
FF	28.29	0.48			
28 in. short	20.39	4.44	**20.57**	**0.00**	**yes**
FF	10.07	0.20			

(III) Comparison between 28 in. short vs. D1 (bare)

Test (Bare)	**Average**	**Stdev**	**F**	**p**	**Conclusion**
28 in. short	81.64	4.86	**189.07**	**0.00**	**yes**
D1	117.98	3.20			
28 in. short	58.37	2.66	**167.33**	**0.00**	**yes**
D1	76.77	1.49			
28 in. short	30.39	0.85	**86.23**	**0.00**	**yes**
D1	24.80	1.47			
28 in. short	17.09	1.63	**0.16**	**0.70**	**no**
D1	17.45	1.24			

28 in. short	35.90	1.31	**642.74**	**0.00**	**yes**
D1	17.11	1.13			
28 in. short	40.38	1.64	**270.17**	**0.00**	**yes**
D1	55.24	1.20			
28 in. short	25.78	0.66	**125.10**	**0.00**	**yes**
D1	30.48	0.90			
28 in. short	30.73	2.73	**153.73**	**0.00**	**yes**
D1	13.33	0.35			
28 in. short	40.28	1.36	**342.89**	**0.00**	**yes**
D1	54.80	1.29			
28 in. short	27.66	1.05	**1.26**	**0.28**	**no**
D1	28.29	0.48			
28 in. short	20.39	4.44	**20.57**	**0.00**	**yes**
D1	10.07	0.20			